AFRL-RX-WP-TR-2019-0263

NANO-LITZ

Kasey J. Russell and David J. Carter

The Charles Stark Draper Laboratory, Inc.

30 SEPTEMBER 2019
Final Report

AIR FORCE RESEARCH LABORATORY
MATERIALS AND MANUFACTURING DIRECTORATE
WRIGHT-PATTERSON AIR FORCE BASE, OH 45433-7750
AIR FORCE MATERIEL COMMAND
UNITED STATES AIR FORCE

NOTICE AND SIGNATURE PAGE

Using Government drawings, specifications, or other data included in this document for any purpose other than Government procurement does not in any way obligate the U.S. Government. The fact that the Government formulated or supplied the drawings, specifications, or other data does not license the holder or any other person or corporation; or convey any rights or permission to manufacture, use, or sell any patented invention that may relate to them.

This report is the result of contracted fundamental research deemed exempt from public affairs security and policy review in accordance with SAF/AQR memorandum dated 10 Dec 08 and AFRL/CA policy clarification memorandum dated 16 Jan 09. This report is available to the general public, including foreign nationals.

Copies may be obtained from the Defense Technical Information Center (DTIC) (http://www.dtic.mil).

AFRL-RX-WP-TR-2019-0263 HAS BEEN REVIEWED AND IS APPROVED FOR PUBLICATION IN ACCORDANCE WITH ASSIGNED DISTRIBUTION STATEMENT.

//SIGNATURE//	**//SIGNATURE//**
JOHN BOECKL	
Work Unit Manager	Branch Chief
Soft Matter Materials Branch	Soft Matter Materials Branch
Functional Materials Division	Functional Materials Division
Materials and Manufacturing Directorate	Materials and Manufacturing Directorate

This report is published in the interest of scientific and technical information exchange, and its publication does not constitute the Government's approval or disapproval of its ideas or findings.

REPORT DOCUMENTATION PAGE

Form Approved
OMB No. 0704-0188

1. REPORT DATE *(DD-MM-YY)*	2. REPORT TYPE	3. DATES COVERED *(From - To)*
30 September 2019	Final	09 July 2015 – 31 August 2019

4. TITLE AND SUBTITLE
NanoLitz

5a. CONTRACT NUMBER
FA8650-15-C-7636

5b. GRANT NUMBER

5c. PROGRAM ELEMENT NUMBER
65502E

6. AUTHOR(S)
Kasey J. Russell and David J. Carter

5d. PROJECT NUMBER
DARPA

5e. TASK NUMBER

5f. WORK UNIT NUMBER
X107

7. PERFORMING ORGANIZATION NAME(S) AND ADDRESS(ES)

The Charles Stark Draper Laboratory, Inc.
555 Technology Square
Cambridge MA 02139-3563

8. PERFORMING ORGANIZATION REPORT NUMBER

9. SPONSORING/MONITORING AGENCY NAME(S) AND ADDRESS(ES)

Air Force Research Laboratory
Materials and Manufacturing Directorate
WPAFB OH 45433-7750
Air Force Materiel Command
United States Air Force

Defense Advanced Research Projects Agency (DARPA)
3701 North Fairfax Drive
Arlington VA 22203-1714

10. SPONSORING/MONITORING AGENCY ACRONYM(S)
AFRL/RXAS

11. SPONSORING/MONITORING AGENCY REPORT NUMBER(S)
AFRL-RX-WP-TR-2019-0263

12. DISTRIBUTION/AVAILABILITY STATEMENT
DISTRIBUTION STATEMENT A. Approved for public release. Distribution is unlimited.

13. SUPPLEMENTARY NOTES
Report contains color.

14. ABSTRACT ***(Maximum 200 words)***

Litz wire is used to combat high-frequency skin effect loss in solid wires, but conventional wire is not useful above ~10 MHz. A2P Nano-litz developed novel methods to fabricate and manipulate insulated wires ~1um in diameter, enabling fabrication of litz wire optimized for GHz frequencies. We show that our Litz wires have lower loss than solid wires or simple bundles, in agreement with analytical models of litz behavior. This work has the potential for >10x lower resistive losses for many high frequency resonators and inductors, such as probe coils used in nuclear magnetic resonance spectroscopy. This research also highlights work done to demonstrate potential avenues for scaling to commercialization of this technology.

15. SUBJECT TERMS
DARPA report, Litz wire, skin effect loss, high frequency inductors, inductor quality factor, nanowires, microwires, nuclear magnetic resonance, high frequency resonators, wireless power transfer, power conversion, high frequency magnetics

16. SECURITY CLASSIFICATION OF:			17. LIMITATION OF ABSTRACT:	18. NUMBER OF PAGES	19a. NAME OF RESPONSIBLE PERSON (Monitor)
a. REPORT	b. ABSTRACT	c. THIS PAGE			John Boeckl
Unclassified	Unclassified	Unclassified	SAR	84	19b. TELEPHONE NUMBER *(Include Area Code)* (937) 255-9906

TABLE OF CONTENTS

LIST OF FIGURES

LIST OF TABLES

1 SUMMARY

At high frequencies, current in a conductor is confined to a layer at the surface of the conductor. This “skin effect” reduces the effective cross-sectional area of the conductor, thereby increasing its effective resistance. Increased conductor resistance can lead to a wide range of potentially detrimental effects on system performance, from decreased efficiency of high-frequency power amplifiers to reduced signal-to-noise ratio for nuclear magnetic resonance systems.

At low frequencies, skin effect can be mitigated using litz wire, but such wire depends on separating a large conductor into individual strands that are each thinner than the skin depth. Unfortunately, commercially-available wire is an order of magnitude too large to enable fabrication of GHz litz wire today. Even if such wire were available, it would be 100x weaker than today’s finest wire and would therefore be impossible to manipulate into litz topology using conventional processing methods.

We have developed both wire fabrication procedures and wire manipulation techniques that can scale to the extreme dimensions and force regime necessary for fabrication of GHz litz wire. Our wire fabrication approach is not a variant of conventional wire drawing. Rather than reducing the diameter of a thicker stock wire, we started with long, continuous nanofibers, which were coated in the desired material to reach the target (composite) wire diameter. To then manipulate such thin wires, we utilized fluid flow through thin capillaries to tension and guide wires while reversibly attaching one end to, e.g., the shaft of an electric motor. Individual wires were twisted into bundles, and those twisted bundles could then be twisted into larger bundles in a hierarchical fashion, resulting in true GHz litz wire (Figure 1).

As noted in Ref. [1], some early references on litz wire claim that it becomes ineffective at frequencies significantly above ~1 MHz[2], [3]. While there was no quantitative analysis to buttress the claim (and, as we discovered, it is very difficult to analyze in detail), the frequency limit of early litz appears in retrospect to be mainly due to limitations in wire fabrication. To verify the expected performance enhancement of our nano-litz wire, we fabricated a wide range of bundles, both hierarchically twisted into litz topology and ‘untwisted’ comparison bundles. In addition, we fabricated individual wires with approximately the same cross-sectional conductor area (i.e. approximately the same DC resistance) as the fabricated bundles. These results clearly show the expected difference in scaling for nano-litz versus non-litz wires and bundles, confirming that litz wire continues to function well into GHz frequencies.

Having shown that wires can be fabricated and manipulated at such challenging length scales, and having demonstrated that nano-litz bundles are able to mitigate skin effect at GHz frequencies, a key question is whether the wires and bundles could be manufactured at scale and at reasonable cost. While a full transition to manufacturability was outside the scope of this program, we have demonstrated the key elements that would be required for production of long lengths (~10 m) of affordable wire. First, we have demonstrated reel-to-reel transfer of ~meter-long single-strand electrospun nanofiber. Next, we have developed a contactless electroplating processes capable of metal deposition onto seeded nanofibers. Finally, we have used a millimeter-scale model to understand the complex dynamics of our wire twisting approach to verify that buckling instabilities will not prevent scale-up to meter-scale lengths

Figure 1. A nano-litz bundle of 22 hierarchically-twisted, gold-coated polymer nanofibers. Individual strands (each ~1.2 µm diameter) are insulated with 40 nm aluminum oxide. Scale bar, 10 µm

In the course of this program, many novel techniques and processes were developed in addition to the core processes used for demonstrating nano-litz performance. One notable discovery was that elastocapillary interactions between wires and nearby surfaces could be utilized to passively twist and braid wires. The simplicity of the apparatus and the complexity of the structures it can fabricate suggest that it may provide an alternative, scalable manufacturing approach for manipulation of thin wires, whether for nano-litz or more broadly.

Some of the likely first uses of nano-litz include high-sensitivity, room temperature NMR spectroscopy and miniaturized, high-Q surface mount inductors for high frequency oscillators and filters. In both of these applications, conventional inductors suffer diminished Q due to skin and proximity effect. In the case of NMR, the higher Q that would be enabled by nano-litz wire translates to higher signal-to-noise ratio, enabling spectroscopy of more complex molecules in shorter times. For wire wound inductors, nano-litz would enable surface-mount components to achieve values of Q comparable to chip-and-wire components, thereby enabling dramatic reductions in volume without sacrificing performance

2 INTRODUCTION

2.1 Skin Effect and Proximity Effect

When a time-varying current is driven through a conductor, magnetic fields are generated that give rise to circulating "eddy" currents within the body of the conductor. At sufficiently high frequency, this effect, known as skin effect, restricts current flow to the outer surface of the conductor (Figure 2). The thickness of this current-carrying layer is set by a length scale known as the skin depth, δ:

$$\delta = \sqrt{\frac{\rho}{\pi f \mu}}, \tag{1}$$

where *f* is the frequency and ρ and μ are the resistivity and permeability of the conductor, respectively. In copper at the 5G frequency band of 28 GHz, for example, skin effect restricts current flow to a surface layer that is only ~390 nm thick (Figure 2). While skin effect is typically analyzed in the context of a solid conductor, a related effect, proximity effect, occurs when the conductor is composed of many individually insulated strands in parallel. In proximity effect, mutual inductance between strands suppresses conduction in the strands near the center of the bundle. By reducing the conductor cross-section available for current transport, skin and proximity effects can increase the ohmic losses in a system by orders of magnitude.

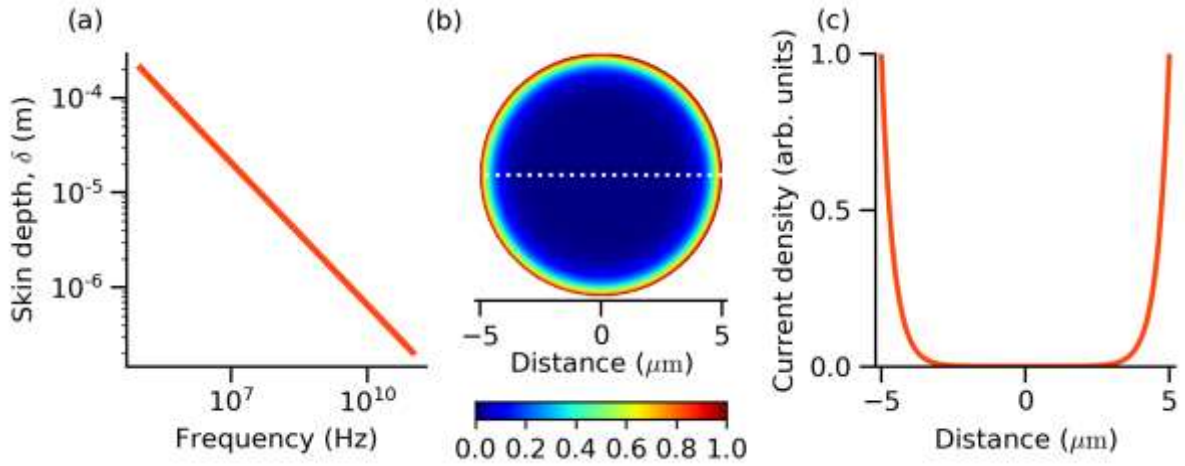

Figure 2. Skin depth and skin effect. (a), Skin depth versus frequency for bulk copper (ρ= 1.68E-8 Ω-m). (b) and (c), Finite element simulation of current distribution in a 58 AWG copper wire at 28 GHz. (b), Cross-sectional plot of normalized current density. (a), Current density versus radial position along the dotted section line in (b)

The increased ohmic losses due to skin and proximity effects lower the efficiency of wireless power transfer, decrease the quality factor (Q) of chip and wire inductors, reduce the resolution and sensitivity of NMR spectrometers, and limit the ability to miniaturize microwave electronics. At megahertz (MHz) frequencies and below, commercial solutions exist to mitigate skin effect using special cable known as litz wire, in which the conductor is separated into many individually-insulated strands, each of which has a diameter less than δ (Figure 3). These strands

are then twisted into hierarchical twists-of-twists so that each strand varies position between the center of the bundle and the outer surface.

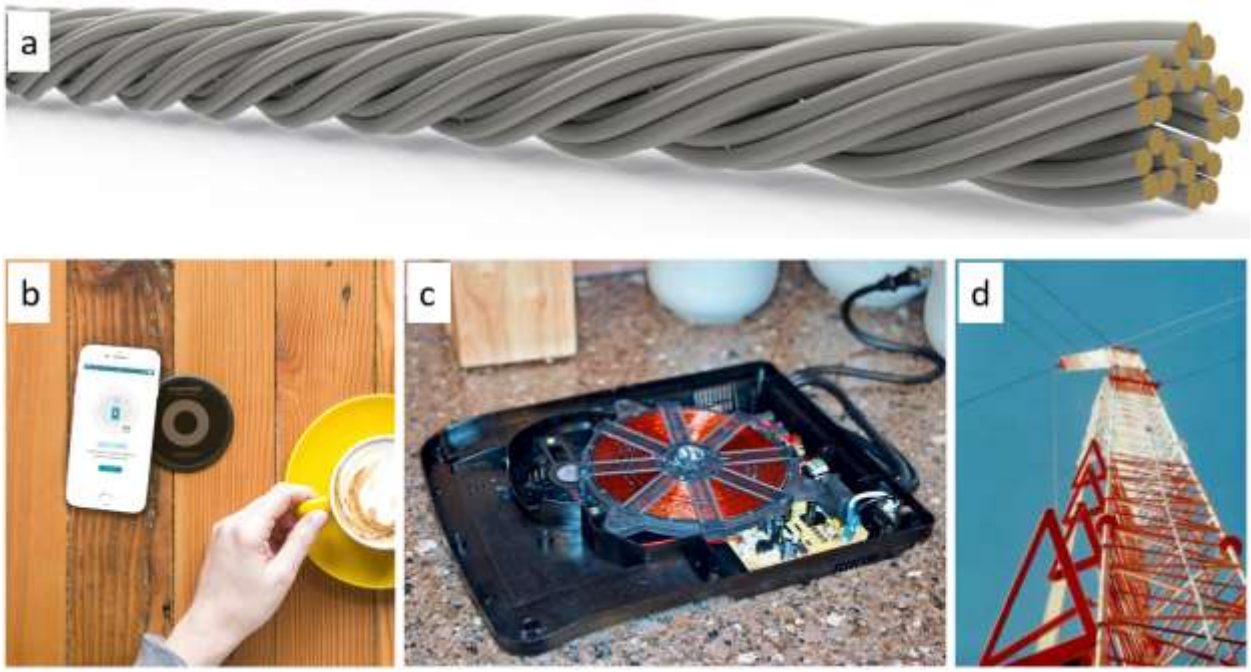

Figure 3. Litz wire and its uses. a, Schematic illustration of a hierarchically-twisted litz bundle of five bundles of five strands each (for 25 total wires). b-d, Example uses of litz wire at sub-MHz frequencies: b, Qi wireless charging mat. c, Induction stove. d, NIST WWVB timing signal transmitting tower.

While conventional litz wire works for frequencies up to the tens of MHz, use at frequencies in the GHz regime requires the ability to produce and precisely manipulate wire that is 10x thinner and 100x weaker than the thinnest available commercial wire. Due to the physics of force scaling versus wire diameter, thin wires present unique challenges for manipulation. As wires become thinner than ~10 μm (which coincides with the lower limit of conventional wire drawing), random and time-varying ambient forces such as electrostatics and laboratory air currents become larger than gravity (Figure 4).

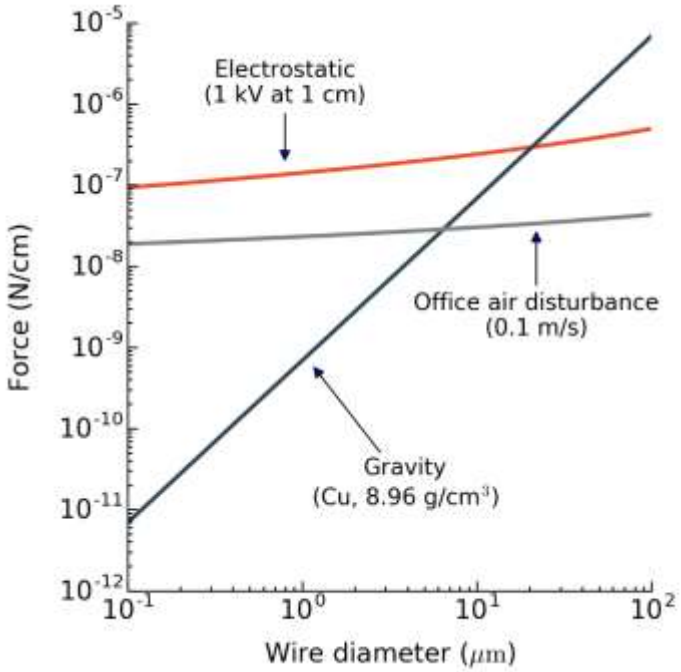

Figure 4. Typical laboratory forces acting on a wire.

In the A2P Nano-Litz program, we have developed a series of novel approaches to both wire fabrication and manipulation. Our wire fabrication process can produce wire with sub-micron diameter over multi-centimeter lengths. Our primary manipulation approach can fabricate hierarchically-twisted litz wire bundles containing a total of 50 individual ~1 µm insulated strands arranged in various twisted sub-bundles, and we have experimentally confirmed that these nanolitz bundles can mitigate skin effect at frequencies of ~10 GHz. In addition, we've laid the groundwork for manufacturability of ~1 µm diameter wire by developing reel-to-reel fabrication of ~1 µm wire and by analyzing the physics of nonlinear geometric instabilities in super high aspect ratio filaments. We have also explored alternative manipulation strategies utilizing both capillary forces and dielecrophoresis and have investigated the ultimate miniaturization regime of braided DNA molecules.

2.2 Fabrication of Thin Wires

Conventional wire fabrication begins with a large-diameter rod of metal that is drawn through a series of consecutively smaller dies to gradually reduce its diameter. As the wire becomes thinner than ~40 AWG (~80 µm diameter) handling via conventional methods becomes more difficult, wire breakage becomes more common, production rates decrease, and cost per kilogram increases significantly (Figure 5 and Ref. [4]). In the case of the thinnest copper wire commonly available commercially (58 AWG, ~10 µm diameter), the wire will have undergone dozens of drawing operations to achieve a total reduction in area of ~10^6 relative to the starting rod. Below this minimum diameter, the tensile strength of the wire is too low to enable further drawing operations.

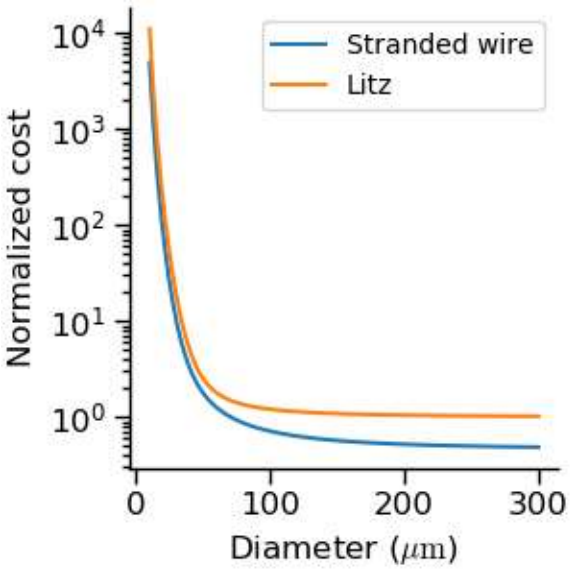

Figure 5. Normalized cost per unit mass of wire produced via conventional wire drawing.

In contrast to conventional wire drawing, the wire fabrication process we have developed utilizes individual nanofibers as one-dimensional substrates to enable bottom-up fabrication of nano- and micro-wires of nearly arbitrary materials. First, using a highly optimized eletrospinning process, we produce arrays of individual high-strength polymer nanofibers (Figure 6). These nanofibers are transferred to processing fixtures and subsequently coated with the desired materials through a variety of deposition processes including physical vapor deposition, chemical vapor deposition, atomic layer deposition, and electroplating. Our baseline process utilizes a nanofiber with average diameter of ~300 nm, which therefore sets the minimum physical diameter of our wire, although thinner nanofibers or individual carbon nanotubes could be used to create thinner wires via the same process. Once ready for assembly into bundles, the wires are individually harvested and inserted into a custom apparatus for twisting bundles of individual nanowires.

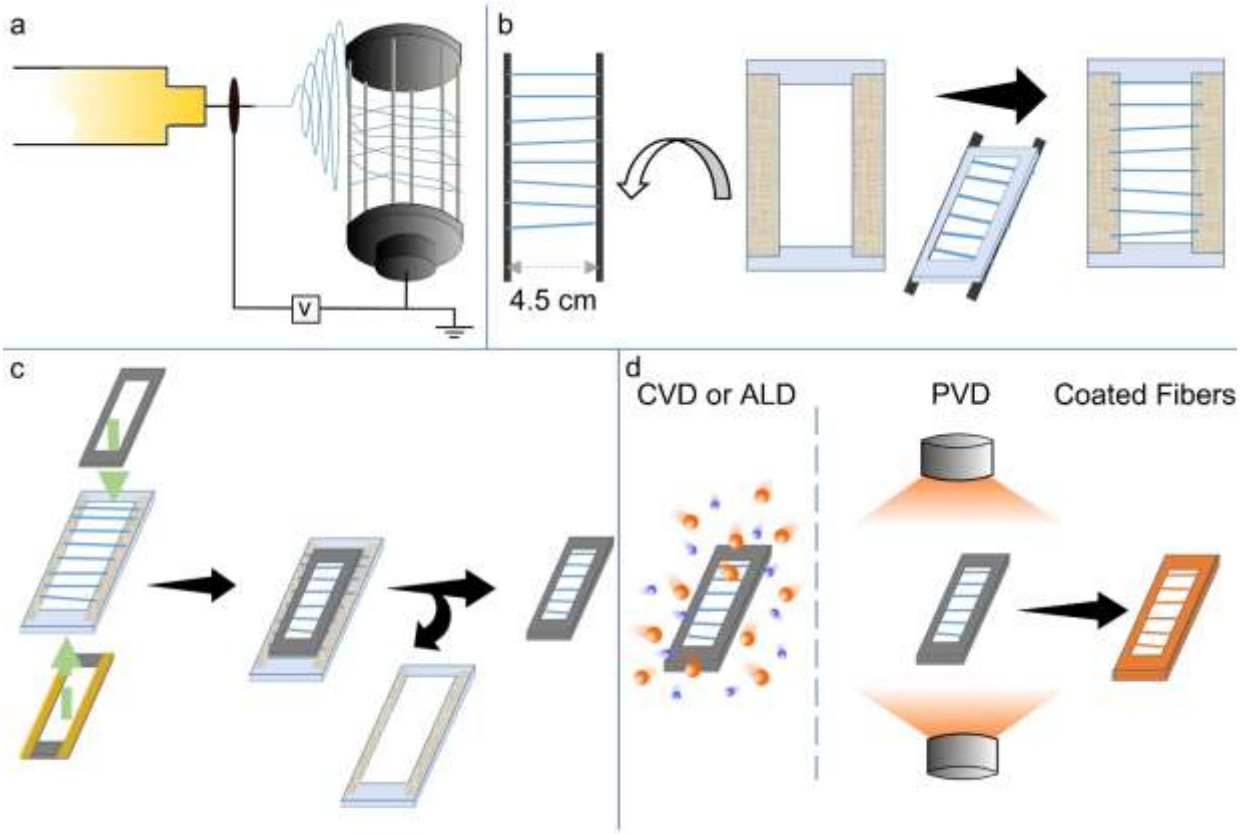

Figure 6. Electrospinning and fiber transfer. (a) Diagram of the electrospinning experiment. (b) Schematic of fiber transfer steps from the spoked drum onto a holder with double-sided tape. The final holder can be used directly for sputter coating or as an intermediate holder to transfer for CVD/ALD holders. (c) Transfer of fibers onto metal holder for deposition experiments. The top frame can be attached using screws, avoiding any tape that might interfere with CVD or ALD experiments. (d) Scheme of metal coating onto polymer nanofibers with different methods.

3 METHODS, ASSUMPTIONS, AND PROCEDURES

3.1 Wire Fabrication

As illustrated in Figure 6 and described in detail in Reference [5], our wire fabrication process utilizes individual, high-strength polymer nanofibers as a scaffold for deposition of various metals (and insulators). These metal wires can then be coated in an additional insulating layer to form insulated single strands. More generally, this approach can yield individual sub-micron diameter wires that are at least several centimeters long from nearly any material or combination of materials that can be sputtered, thermally evaporated, or otherwise deposited at temperatures up to ~400 °C.

3.1.1 Electrospinning nanofibers of the high-strength polymer PMIA.

Poly(m-phenylene isophthalamide) (PMIA) was purchased from Sigma-Aldrich (Product No: 446521-100g, MW ≈ 81,000). It was dried at 140 °C in air before making a solution. It comes in chopped fiber form. $CaCl_2$ (Product No: 746495-100g) and N,N-dimethylacetamide (DMAc) (Product No: D137510-500mL) were also purchased from Sigma Aldrich and were used without further purification.

Sputtering materials were provided by Harvard's Center for Nanoscale Systems or purchased from Kurt J. Lesker. Copper thermal evaporation source was purchased from Kurt J. Lesker (99.99% pure, Product No: EVMCU40QXQD).

The Co DLE-CVD precursor used in this work is a cobalt amidinate, bis(*N*,*N'*-diisopropylacetamidinato) cobalt(II) ($CoC_{16}H_{34}N_4$) from Strem Chemical Company, which has been reported previously[6]. Tetradecane purchased from MilliporeSigma Chemical Co. was distilled from sodium to remove moisture before being used as solvent for the Co amidinate precursor.

For the ALD of $MnSi_xO_y$, tris-tert-pentoxysilanol (TPS) was purchased Sigma-Aldrich (Product No: 553441). Manganese (II) bis(*N,N'*-di-tert-butylacetamidinate) ($Mn(AMD)_2$) was acquired from Strem Chemical Company and was also previously reported[6].

12.0 - 18.0 wt. % PMIA and 8.0 wt. % CaCl2 solutions in DMAc were prepared in 20 mL glass scintillation vials with stirring at 140 °C for at least 24 hours. PMIA was typically dissolved within one hour after drying. Green Sm-Co stir bars (Sigma-Aldrich, Product No: Z671592) were used to stir the viscous solutions, and Teflon sealed caps (Qorpack, VWR Catalogue No: 16161-188) were screwed onto the scintillation vials to prevent leakage at this high temperature. 12.0 wt. % PMIA solution was used to generate fibers for the TGA experiments. Most of the optimized fiber processing was carried out with 17.5 wt. % PMIA solution.

Electrospinning was done with a commercial climate-controlled electrospinner system (EC-CLI, IME Technologies). The climate controller was connected to a compressed dry air line fitted with an additional dehumidifier (Fiber Dry Filter FMDR 301-03-AD, PISCO) that reduced the chamber humidity down to 2-3% and then re-humidified it to a controlled, preset level. Polymer

solution was loaded into a plastic syringe and delivered to the nozzle via polytetrafluoroethylene tubing using a syringe pump. The nozzle-to-collector distance was varied between 4 and 12 cm. In general, PMIA fibers were spun from a single solution droplet at the nozzle without continuous pumping during the experiment. (For more continuous spinning of a yarn of fibers, one would need to pump the solution at about 120 µL/h based on our fiber generation rate.)

After initial optimization, most fiber samples were spun while keeping the chamber around 10% relative humidity (RH) and 24°C. A 17.5 wt. % PMIA and 8.0 wt. % $CaCl_2$ solution in DMAc was used for most of the experiments. Nozzle-to-collector distance was typically kept at 8.0 cm. After the collector was brought up to speed at 2500 rpm, electrospinning was initiated by applying a +12 kV voltage to the nozzle with respect to the grounded collector. After the jet was initiated, fiber diameter and alignment were optimized by lowering the voltage to as low as 5-6 kV without stopping the jet. Once the voltage was turned on at 12 kV, a droplet at the nozzle typically grew and ejected after a few seconds, to form a continuous jet. A rotating drum collector (EM-RDC, IME Technologies) covered with aluminum foil was used to prepare mats of aligned fibers or a rotating spoked-drum collector (EM-RTC with EM-PSD, IME Technologies) with custom windshields was used to prepare single fibers with rotation speeds up to 2500 rpm. (The spoked-drum collector originally comes with 12 spokes, and every other spoke was removed to only have 6 spokes with increased separation.)

For making single fibers, the jet was initiated at one end of the collector, and once the jet was stabilized at a selected lower voltage, the nozzle was translated to the other end of the collector (using EM-TNS, IME Technologies) to separate the fibers along the collector. Voltage was manually turned off as soon as the nozzle reached the end of the collector. (If the jet was allowed to continue beyond one pass over the collector, more fibers got deposited that typically crossed and/or stuck to the existing fibers.) A typical experiment lasted under one minute. There was a messy region of fibers around where the jet is initialized on the collector, while the aligned single fibers covered the rest of the collector. The area of the messy fiber region decreased with decreasing nozzle-to-collector separation.

3.1.2 Transferring Nanofibers to Processing Fixtures.

We used custom frames of varied dimensions for taking the fibers off the spoked collector and holding them during depositions. The spoke-to-spoke separation of the electrospinning collector was 4.5 cm (after we removed every other spoke to increase this separation, Figure 7a). For getting the highest yield, we placed acrylic frames of matching width on three sides of the collector first (Figure 7b). Then, narrower frames with double-sided tape along their long edges were brought into contact with the fibers to collect them. Without adding the larger holders that press onto the fibers at their points of contact with the spokes, harvesting fibers from one side of the collector often causes fibers to get pulled from adjacent faces of the 6-sided collector.

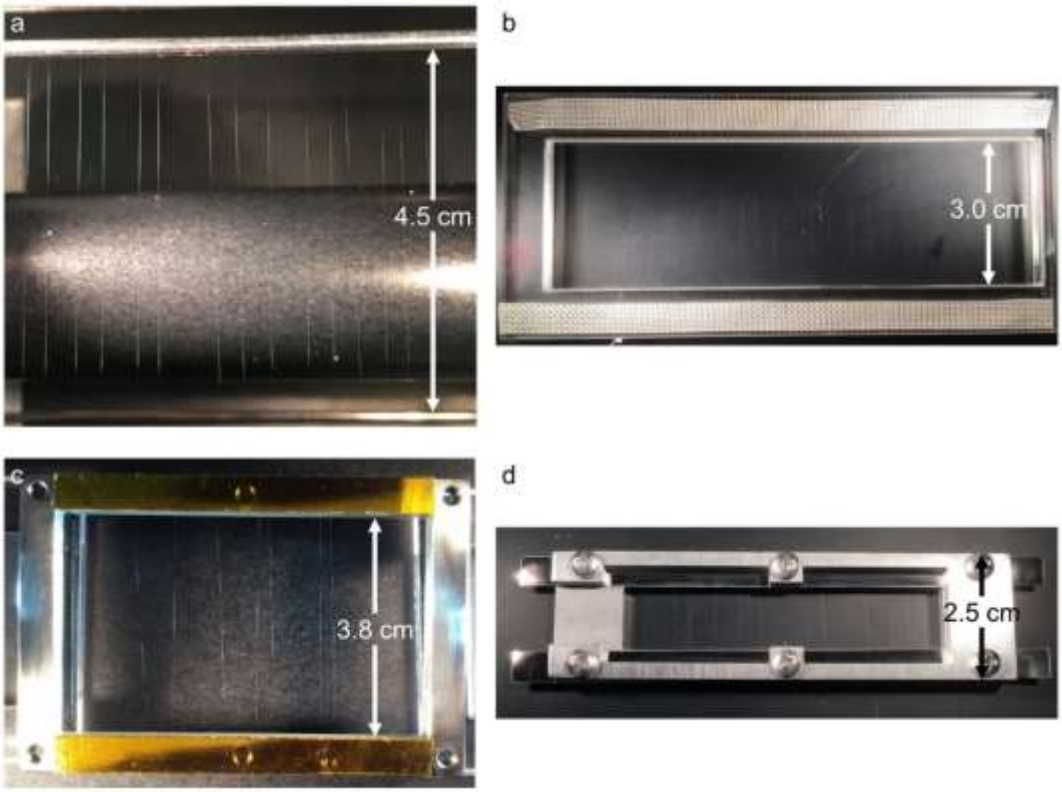

Figure 7. Photographs of electrospun nanofibers. (a) Photograph of aligned fibers on part of the rotating spoked-drum collector. (b) Photograph of aligned fibers on a transfer holder. (c) Photograph of our widest holder with some single fibers attached by double-sided tape that is suitable for PVD. (d) Photograph of Co coated fibers with CVD. Bright illumination from the side results in scattered light from the submicron fibers, making them visible to the naked eye.

It is best to break the fibers away from the frames forcibly during transfer, as merely bringing the holder with tape in contact with the fibers and then pulling away may leave fibers behind; i.e., the strength of the adhesive (for a tape that is often ¼" wide) is often not enough to break the fibers when pulled away.

For physical vapor deposition (PVD), we either added another top frame to the existing double-sided tape, or we added screws on four corners of a frame where we had threaded holes (Figure 7c). This was done so that the holder can be flipped between two PVD depositions to improve conformality without bringing the fibers in contact with a surface to which they might possibly adhere. Qualitatively, we found that the fibers can be brought into contact and lifted back from smooth Si wafer or glass surfaces, but if they get into contact with a plastic surface, they often strongly adhere to it and break off the holder. Most of the holders and screw caps we used are 1/8" thick, but we also used 1/16" thick top and bottom frames for certain sputtering experiments that required thinner samples.

We used double-sided Kapton tape (McMaster-Carr, Product Numbers 7361A11 or 7361A12) for most of our deposition experiments. Especially during dry seasons, Kapton tape often

becomes non-sticky, in which case we revived its adhesiveness by wetting it with isopropanol before starting to collect fibers. For parts that did not need to go into a deposition chamber (transfer holders, fixing holders to surfaces, etc.), we used a fiber glass reinforced cloth masking tape (McMaster-Carr, Product Number 7566A1) which is more conveniently handled and can be removed from most surfaces without leaving a residue.

Between experiments, fibers were kept in petri dishes that were stored in a desiccated environment or vacuum sealed in a plastic bag with silica gel packs. When first placing the fibers into a petri dish, it is important to reduce static charge using an anti-static gun. The entire inside of the petri dish needs to be thoroughly neutralized; otherwise fibers sag and become slack. Brief tests show this sagging is reversible, but if left sagging, the fibers can slip on the tapes from the sides and sag permanently; this adds a complication to the conformality of a CVD coating. Especially when using wide gapped (Figure 7c) or thin (1/16") holders, this sagging can cause the fibers to touch the bottom of the plastic dish, at which point they become strongly attached and eventually break.

For deposition processes operating at high temperatures, we needed to use a mechanically clamped holder to avoid issues with tape adhesive. Our clamped holder design consists of 3.5"x1" frames with a central gap of 0.52" with three holes along the long edges that are threaded for the bottom part and through holes for the top part. More holes increase grasping efficiency at the cost of potentially breaking fibers in their vicinity. We found it necessary to add a layer of Kapton film (typically by attaching it to the bottom frame with double-sided tape on the edges) that serves as a gasket. Without that, we more commonly observe fibers breaking during depositions – especially for chemical vapor deposition processes that operate at a larger flow rate of gases. Fibers were first transferred onto an acrylic frame with a gap that is larger than the mechanical holder. We used the same acrylic holders with a width matching the spoke separations that we described above for fixing the 6 sides. The bottom part of the clamped holder is fixed on a surface (using large pieces of double sided tape). The intermediate holder is then placed so the fibers stretch along the bottom part of the holder, and the intermediate tape is also fixed on the same surface. The top frame is then lowered gently onto the bottom part, sandwiching the fibers in the middle (Figure 6c), and screwed in place. Afterwards, the transfer holder can be removed, breaking fibers outside the clamped region seemingly without affecting the fibers within. If the fibers are held strongly, we can avoid fibers breaking during CVD. Figure 6d shows a mechanically clamped holder with fibers after being coated with CVD. Apart from serving as a pliable gasket layer, the polymer film might also be enhancing grasping efficiency due to strong van der Waals forces with the fibers. We found that after depositions, if the top frame is gently removed, many fibers often remain suspended and attached to the Kapton film on both sides (though they certainly break in the absence of a Kapton film).

3.1.3 Removing $CaCl_2$ from electrospun PMIA nanofibers

$CaCl_2$ was added to the electrospinning solution to improve solubility of PMIA. Unfortunately, the presence of a hygroscopic salt in the electrospun nanofibers often led to undesirable absorption of water, particularly for nanofibers that were exposed to high humidity (Figure 8 and Ref. [5]). By washing the nanofibers with DI water, salt content in the fibers could be greatly reduced.

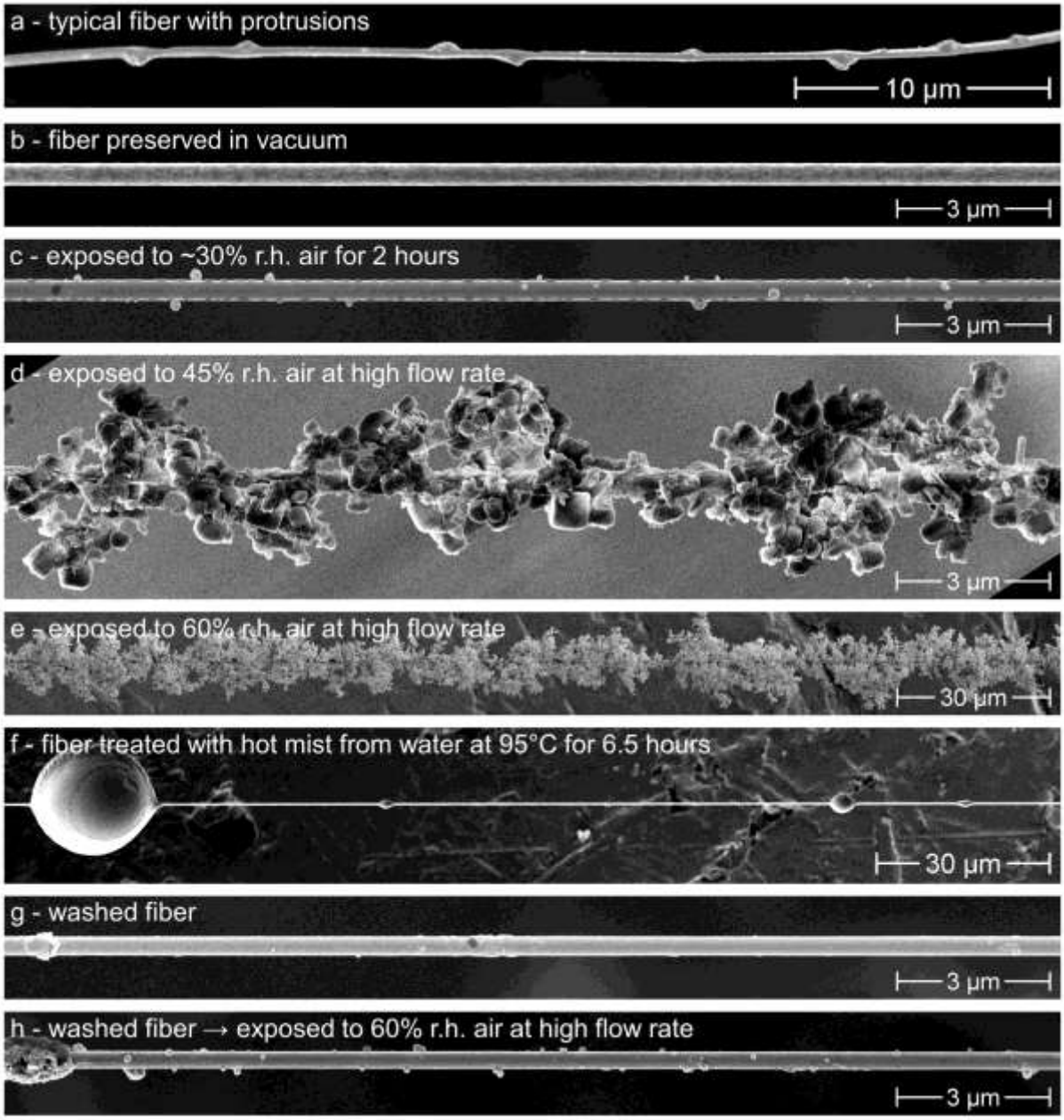

Figure 8. Humidity-dependent morphology evolution: (a) SEM image of a bumpy Pt/Pd alloy (80/20) coated PMIA fiber. (b) Fiber kept in vacuum for 2 hours before imaging. (c) Fiber exposed to ambient air at ~30% RH for 2 hours. (d) Fiber annealed with a high flow rate 45% RH air at room temperature. (e) Fiber annealed with a high flow rate 60% RH air at room temperature. (f) Fiber annealed over a beaker of hot water for 6.5 hours. (g) Fiber where $CaCl_2$ is mostly removed by treatment with an ultrasonic humidifier for 6 hours. (h) After $CaCl_2$ was removed with the previous treatment, fibers were exposed to a high flow rate of 60% RH air as in part d, but they did not roughen nearly as much. (All fibers were coated with a thin layer of Pt/Pd alloy (80/20) to assist with imaging.)

3.1.4 Metal deposition onto high-strength polymer nanofiber scaffolds.

Metal coatings were deposited onto suspended PMIA fibers using PVD (i.e., either sputter coating or thermal evaporation) to make conductive wires with sub-micron diameters. Since both these methods use line-of-sight deposition with respect to the source materials, depositions were performed from two different sides of the holders with PMIA nanofibers (Figure 6d).

PVD often provides non-conformal coatings around the fibers (Figure 9). For sputtering, conformality seems to be somewhat improved with certain metal targets, such as Ag (Figure 10), while Au sputtering consistently gives off-centered coatings. Sputtered fibers occasionally become slack within their frame fixtures, which confounds the problem. We have also observed that sputtering of Cu under our conditions often leads to samples becoming more brittle, and wires tend to break off from their frames after metal deposition. More stable Cu coated wires can be prepared with thermal evaporation of copper, and the slacking behavior is much less apparent. As the fibers remain tightly held within their fixtures, evaporation of a thin layer of Cu (75 nm onto two sides of the fibers) seems to yield a conformal coating, but a thicker deposition yields the wire cross-section with two crescent shaped coatings on two opposite sides of the wire.

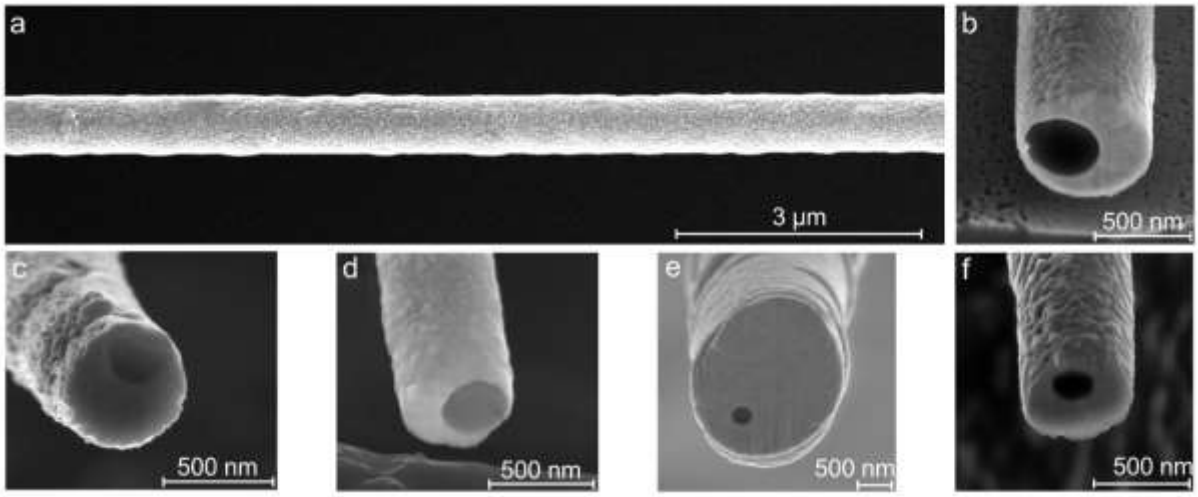

Figure 9. Non-conformal physical vapor deposition on nanofiber scaffolds. (a) Platinum sputter coated fiber and (b) its cross-section. (c) Cross-section of a fiber sputter coated with titanium from one side only. Cross-sections of (d) gold, (e) copper, and (f) cobalt coated fibers sputtered from both sides

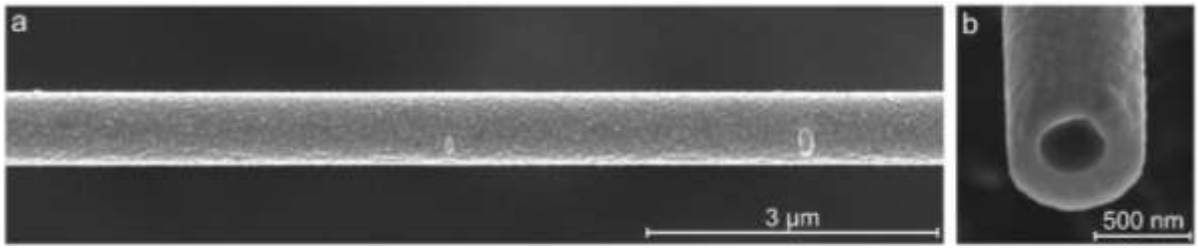

Figure 10. Conformal physical vapor deposition on nanofiber scaffolds. (a) Fiber sputter-coated with Ag from both sides and (b) its cross-section

3.1.5 Deposition of electrical insulation onto ~1 µm diameter metal wires

A variety of deposition processes were utilized to fabricate insulated wires using our process. We deposited Al_2O_3 with atomic-layer deposition (ALD), parylene with chemical-vapor deposition (CVD), and Teflon-like coatings with initiated-CVD (iCVD). Most of our electrical measurements were done with ALD alumina.

3.2 Reel-to-Reel Processing of Nanowires

Electrodeposition of metal layers onto PMIA nanofibers would enable a low cost, scalable route to production of fine wire. A key challenge is that the small diameter of the nanofiber results in a high resistance per unit length. It is therefore advantageous if the anode and cathode contacts to the wire can be located in close proximity to each other. While the cathode contact can be made directly to the spool if the spool is in electrical contact with the wire, the spool is often several centimeters away from the plating region.

The problem was decomposed into several steps of increasing difficulty. We first developed the capability to transfer meter-scale lengths of individual PMIA nanofiber onto and between spools. We next developed methods to electroplate onto individual suspended PMIA nanofibers. We then developed a contact-less electroplating approach and demonstrated its efficacy using commercial wires in a reel-to-reel configuration. Finally, we developed a micro/mesofluidic platform capable of performing the contact-less electroplating on seeded nanofibers in a monolithic device.

3.2.1 Reel-to-reel transfer of PMIA nanofiber.

In order to metallize meter-length scale wire in the sputtering chamber, we developed a system for transferring continuous lengths of the Nomex nanofiber from the 6” drums used as collectors during electrospinning to 1” spools suitable for subsequent processing. An obvious challenge for reel-to-reel processing of nanofiber is the low yield strength of the nanofibers (as low as 50-80 µN). Rather than attempt to mechanically tension the nanofiber, which is the common approach used with larger wires or fibers, we developed a process utilizing fluid droplets and surface tension to tension and guide the nanofiber during spooling (Figure 11). We estimate that, for fibers of 100 nm diameter, our approach could apply tensile forces on the order of 0.1 µN, much less than the 50 µN yield strength of the fiber.

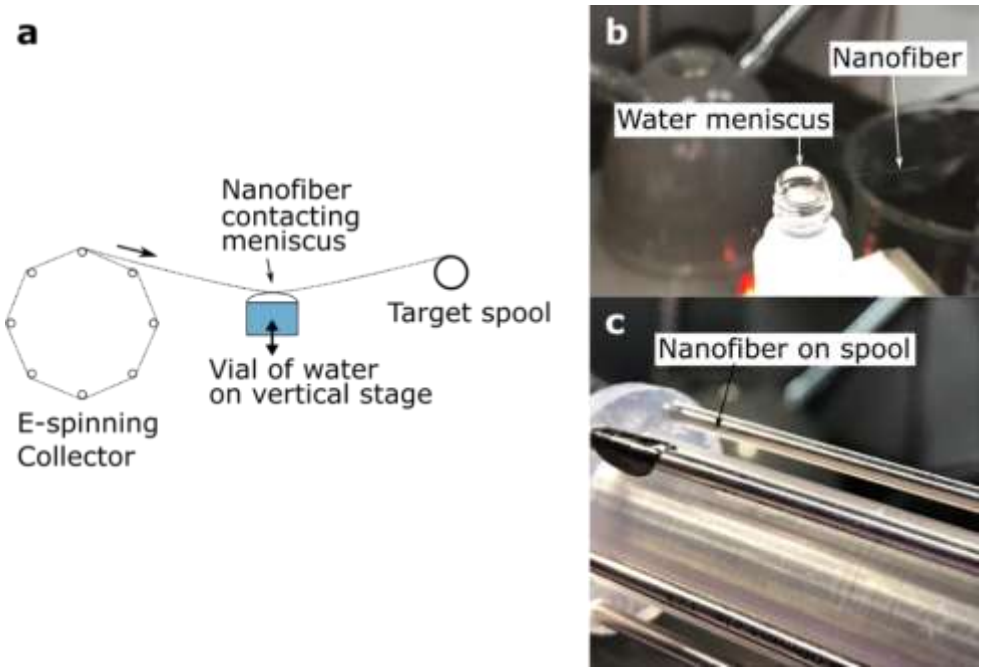

Figure 11. Controlling tension during spooling of PMIA nanofiber. a, Schematic illustration of our tensioning process utilizing hydrophilic interactions between the nanofiber and a water meniscus to provide controllable sub-micronewton forces to tension the nanofiber during spooling. b, Image of PMIA nanofiber in contact with water meniscus during spooling. c, Image of PMIA nanofiber wound around target spool.

In order to increase the efficiency and repeatability of transferring nanofibers between spools, the apparatus was automated using three stepper motors (Figure 12). One stepper motor was used to rotate the electrospinning collector, another was used to rotate the secondary spool, and the third was used to translate a stage holding an over-filled vial of water with protruding meniscus used for tensioning the nanofiber. To initiate the transfer, adhesive tape is pressed to a section of nanofiber on the first spool. While the initial spool is rotating, the tape is then slowly guided across the apparatus to the target spool and pressed to the target spool, anchoring the nanofiber. The nanofiber is intentionally kept loose to prevent accidentally tensioning and breaking the nanofiber. The water meniscus protruding from the glass vial is placed in contact with the (slightly hydrophilic) nanofiber, attracting the nanofiber to the surface of the water, and the vial

is then placed onto the linear stage. Hydrophilic interactions between the nanofiber and meniscus maintain tension on the nanofiber as it is then transferred from spool to spool.

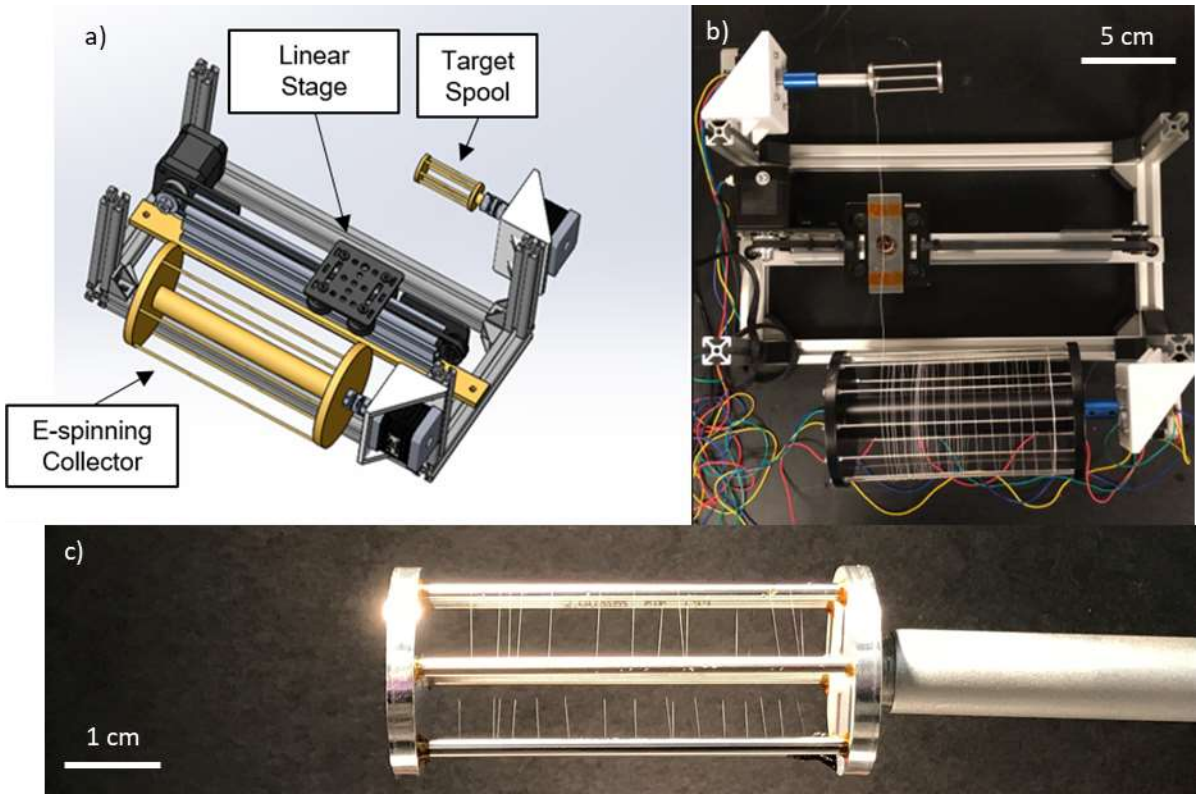

Figure 12. Motorized reel-to-reel nanofiber processing. a) CAD model of spool-to-spool transfer system and b) actual transfer apparatus. C) Successful transfer of 1.2 m of PMIA nanofiber onto a spool

3.2.2 Metallization of Nomex fiber spools using sputter deposition

A vacuum-compatible spool rotation device was designed to continuously rotate the small Nomex spools during processing in a load-locked sputtering system (Figure 13). By continuously rotating the spools during deposition, the nanofibers could be nearly uniformly coated (except for the areas of the wires in contact with the spool's tines). An initial layer of 10 nm Ti and 20 nm Au was deposited onto the fibers to use as a seed layer for subsequent electroplating.

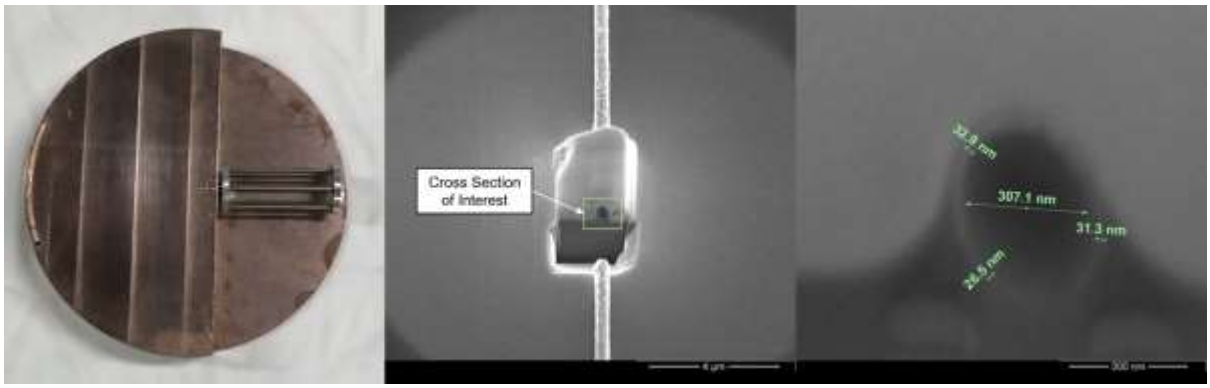

Figure 13. Apparatus for continuously rotating a spool during sputter deposition. Left, Optical image of apparatus (6" diameter). Center and Right, FIB cross-section of completed sputtering, showing the ~300 nm diameter PMIA nanofiber coated with ~30 nm of metal

While this approach did prove effective for metalizing the PMIA nanofiber, we found it difficult to reliably unspool the nanofiber after sputtering. Often the nanofiber would stick to a tine on the spool, likely because of adhesion from the conformal sputtered film. Additional research would be required to optimize the seed layer deposition or preparation process, potentially including investigation of alternative metallization approaches such as electroless metal deposition.

3.2.3 Conventional electroplating

The synthesized nanolitz wire discussed in section 3.1 was fabricated using ~2 cm long PMIA nanofibers coated with sputtered gold. While sputtering enabled rapid process development, a wire fabrication process utilizing electroplating would enable more economical production of wires, especially if larger diameter wires are desired. Electroplating onto nanofibers has two main challenges: making high quality electrical contact to the seed layer while keeping the high conductivity leads out of solution, and making an electrical contact without introducing a force greater than the 50 µN yield strength of the fibers.

Our process development began by using stationary nanofibers. The PMIA nanofibers were mounted on frames as described in Section 3.1.2. The electrochemical cell was comprised of a platinum wire counter electrode (plating anode) and the seed-coated PMIA nanofiber as the working electrode (plating cathode). The platinum wire was immersed in the gold plating solution in a tee-junction, and the PMIA nanofiber was loaded into the plating meniscus. Electrical contact to the PMIA nanofiber was achieved by covering the end of the seed-coated PMIA nanofiber with conducting epoxy to ensure electrical connection to the frame and contacting the frame using mechanically-clamped test leads, as shown in Figure 14. Electroplating was performed at the manufacturer's recommended current density of 4 A/ft^2. Typical electroplating experiments yielded films of thickness in the range of 1s-10 µm. The film was found to be highly conformal and uniform (Figure 15 shows an example of uniformly plated Nomex wire with a thick gold shell surrounding the Nomex filament).

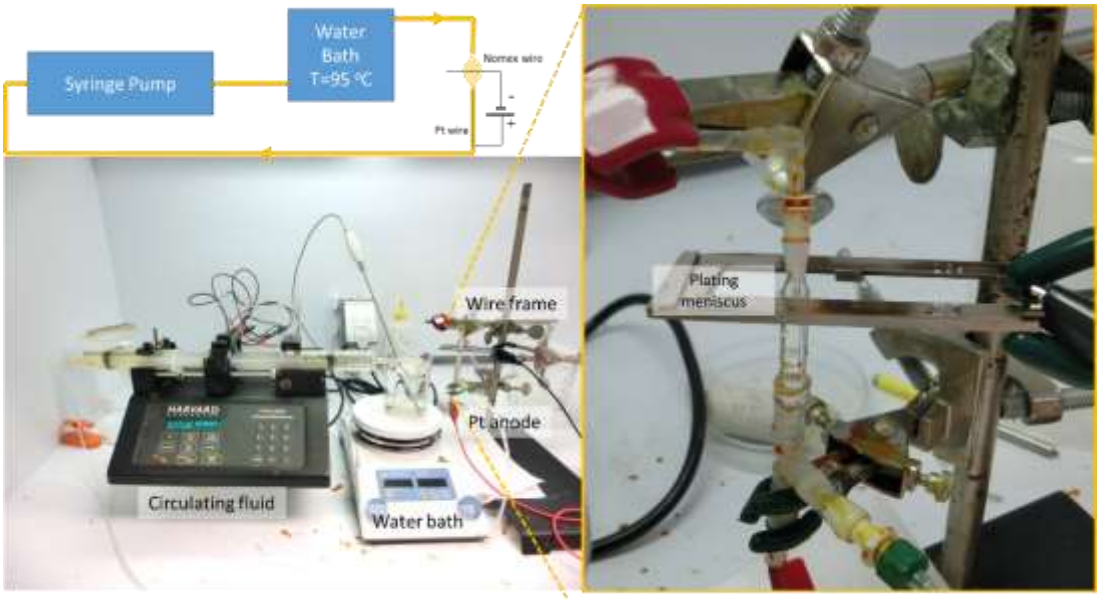

Figure 14. Electroplating bath set up. A syringe pump circulates electroplating solution as it passes through a water bath to raise the temperature and provide more conformal plating. The wires are plated where there is an exposed meniscus of electrolyte providing isolation and mechanical support for the wire as it is plated.

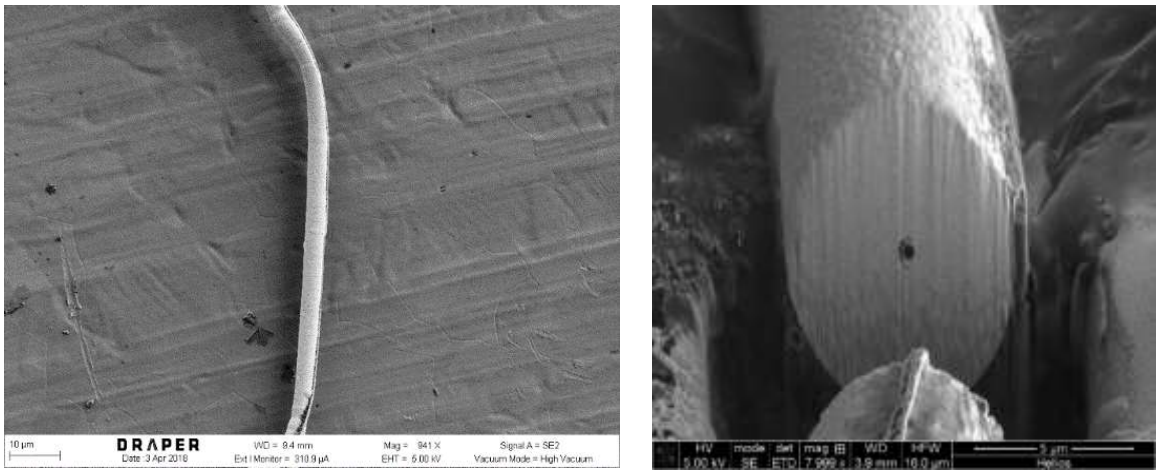

Figure 15. SEM images of PMIA nanofiber electroplated using a current density of 8 mA/cm^2 to achieve a ~5 µm-diameter wire

However, while a traditional electroplating cell set up with direct electrical contact works for short wires, it would be difficult to scale such an approach to reel-to-reel processing of meter-long wire because of the high series resistance of the seed layer. We therefore designed an approach that allows for contactless electroplating.

3.2.4 Contactless Electroplating Using A Closed Bipolar Electrochemical Configuration: Proof of Concept.

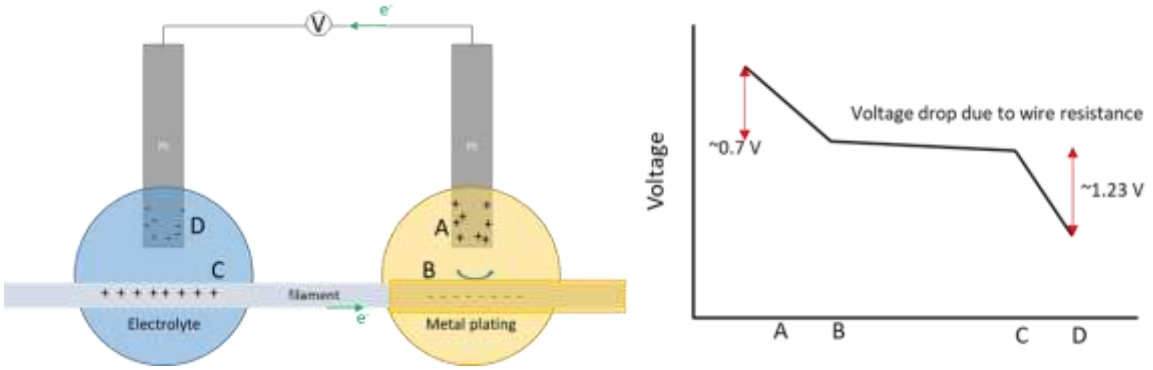

Figure 16. Basic set up of an indirect bipolar electrodeposition (BPE) of gold onto the PMIA filament. The platinum wires are connected to power and a current is driven through. Oxidation/reduction reactions drive ionic current in solution allowing for the PMIA metal-seeded fiber to also under-go redox reactions leading to gold metal plating (V=0.7 V), while hydrolysis occurs in the salt solution (V=1.23 V). Current flows through the filament closing the circuit.

As discussed in previous sections, the very low yield strength of the PMIA fibers has led us to develop creative solutions for wire handling and manipulation using fluids and surface tension to guide the wires. In the case of electrodeposition, we have designed an indirect bipolar electrochemical cell for contactless plating. In a bipolar cell, there are typically two driving electrodes that are connected to the power supply, in our case two platinum electrodes. The bipolar electrode, in our case the seeded PMIA fiber, bridges the two fluid streams, and is at an intermediate floating potential allowing for electronic current to flow through but not ionic. This configuration is a closed bipolar electrochemical cell (CBPE) [1] (Figure 16). In our cell, hydrolysis reactions occur in the salt water solution, while gold plating reactions occur in the metal plating solution, thereby requiring at a minimum ~2V of potential to drive the desired reactions.

To first prove that we could control gold electroplating using a CBPE set up, we ran current through 1 mil copper wire isolated between two baths of gold plating solution and 3.5 M KCl solution. We immersed an initial 23 cm length of 25 micron copper wire into plating solution and ran pieces for 7.5 min, 15 min, and 45 min. We observed for a driving current between 1.7 to 0.85 mA (slowly reduced to adjust for shorter lengths) an equilibrium voltage between 2.2 and 3.2 V. Over 45 min we are able to plate 20 microns of gold on top of the copper wire (Figure 17). EDAX analysis also showed that the coating was nearly 100% gold, with copper completely masked by the plated film.

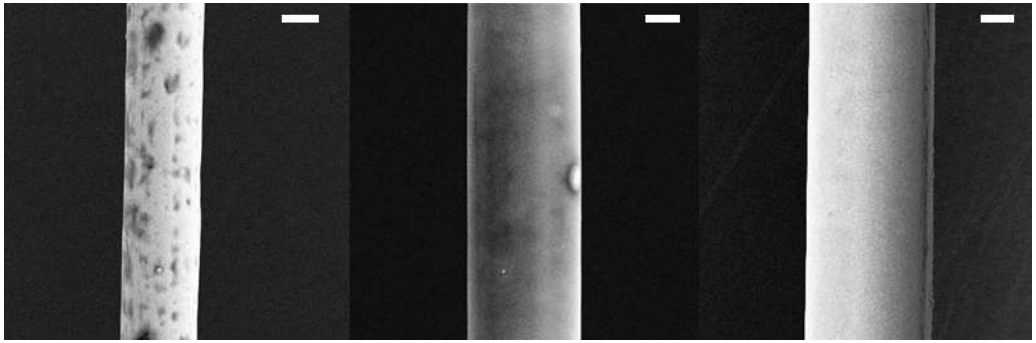

Figure 17. 1 mil copper wire plated in gold using CBPE set up. Over time the thickness plates from 2 microns to 14 and finally to 20 micron thick gold over 45 minutes, demonstrating a scalable process. Scale bar is 10 microns.

Following this demonstration, we scaled up to a circulating plating bath where we could integrate the spool-to-spool configuration. Figure 18 shows a schematic of the recirculating bath, where platinum electrodes are installed on either side of an open channel where a droplet forms, and the wire is fed through the streams. While the configuration shows a feed through with the salt stream first, we have also plated with the gold solution first which has the added benefit of reducing resistance as gold is plated onto the wire. Figure 18 shows the actual set up. Teflon tubing is used to help create a droplet interface in the fluid line.

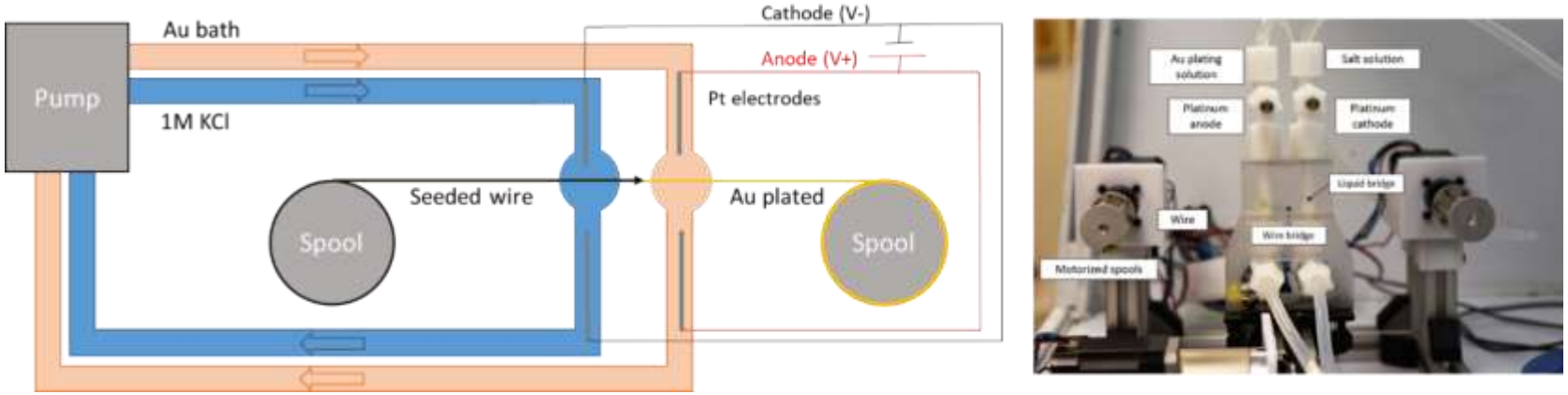

Figure 18. Reel to reel CBPE electroplating using fluid droplets. Two platinum covered titanium rods are used as both the anode and cathode in two separate streams of conductive saline and gold plating solution which are bridged by the wire.

We tested the reel-to-reel set up with 10 micron copper wire, running a length of approximately 5 cm. The wire was fed a rate of 0.04 cm/min through a 0.5 cm droplet at a current of 10 μA (Figure 19).

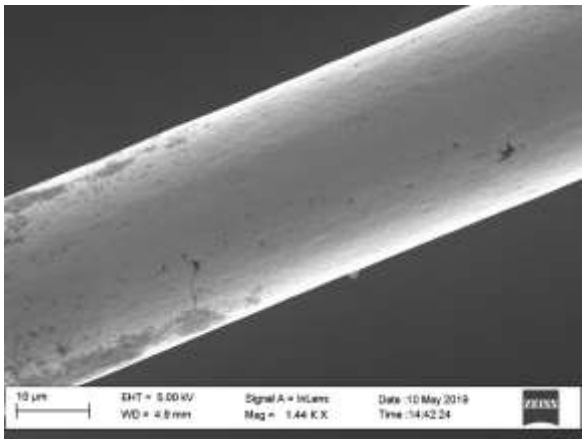

Figure 19. Segment of copper wire coated in gold using the reel-to-reel CBPE set up.

A large challenge of the set up given in Figure 18 is that the fluid stream must be continuous between the platinum electrodes and the open droplets to ensure that the circuit is complete. If a droplet breaks due to mismatched inlet and outlet flows then the circuit breaks, the voltage hits a safety limit, and the potentiostat shuts off thereby stopping the electrodeposition. In addition, when droplets break they can also pull the wires causing the filament to break. Thus, to scale to meter-length scales we re-designed the plating set up to utilize a fluidic chips.

A “meso” fluidic chip was designed to continuously circulate plating solution while allowing for a wire to feed through the middle of the channels. The chip design is depicted in Figure 19, with a 3 mm thick gasket, and 1 cm wide plating channel. In this design, we have put in an air gap between the salt and gold solutions to isolate the solutions and force current to travel via the wire and not ionically through solutions. A future configuration could use water to keep the system in a The fully integrated set up with the reel-to-reel transfer of the wires is shown in Figure 21. Similar to the previous set up, solutions are circulated through the chip and the platinum driving electrodes are immersed in the fluid channels, upstream of the plating filament.

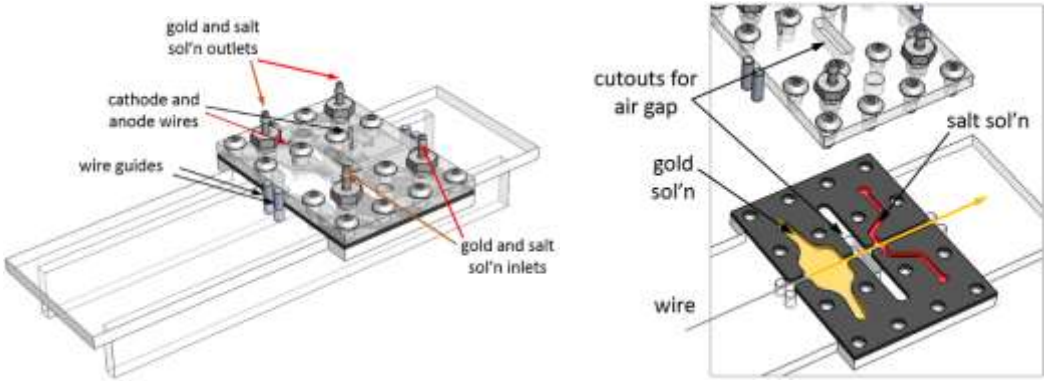

(a) (b)

Figure 20. (a) Mesofluidic chip for contactless electroplating onto a continuously-moving nanofiber scaffold (b) Exploded drawing of chip detail view.

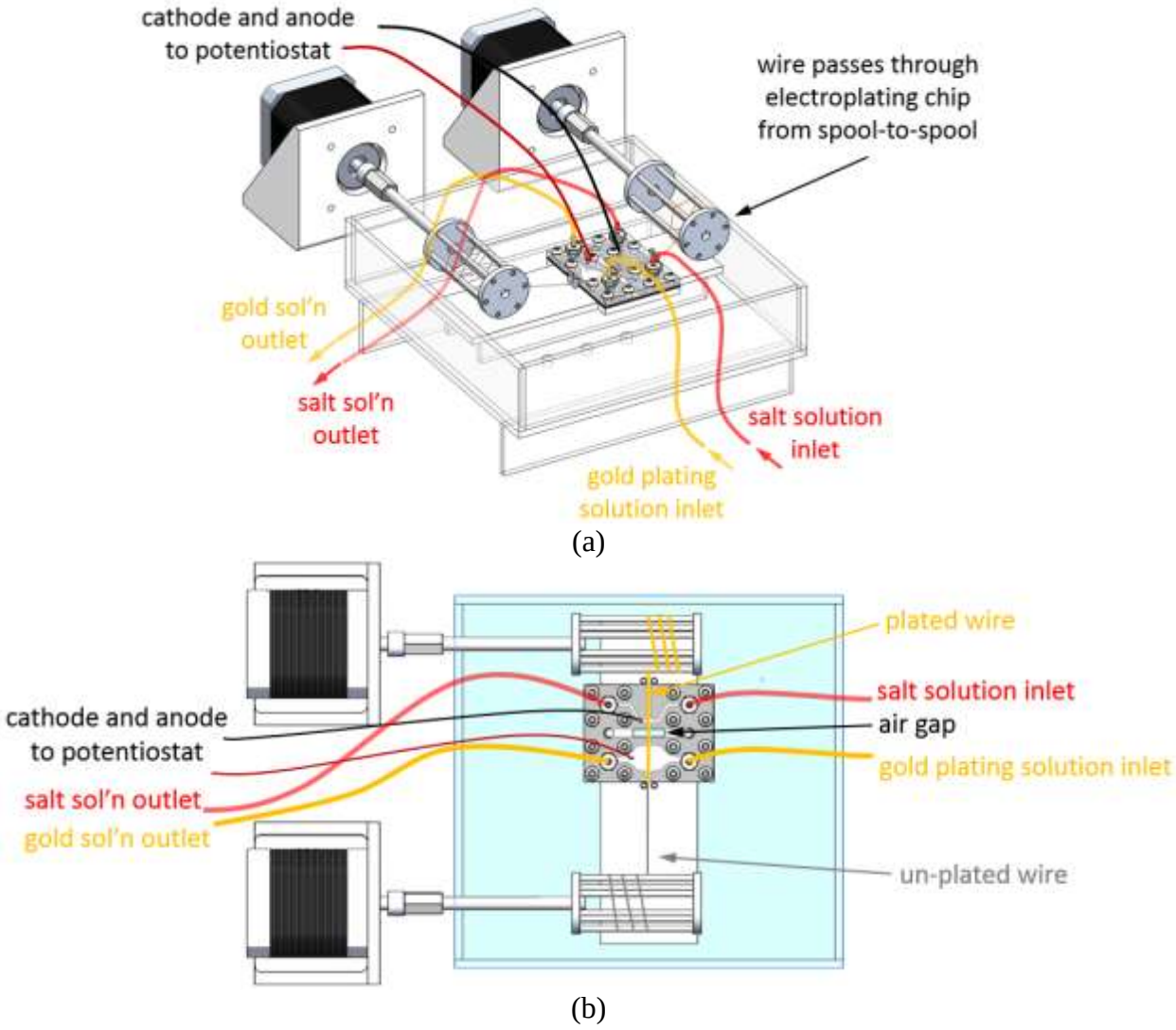

Figure 21. (a) Design of the reel-to-reel electroplating system. (b) Top view of the system.

Using the mesofluidic chip, we were able to scale up from 5 to 85 cm of gold-plated copper wire. We started with 0.7 mil copper wire, applying 24 µA of current and feeding the wire at 0.5 cm/min, for a final gold plating thickness of 500 nm (Figure 22).

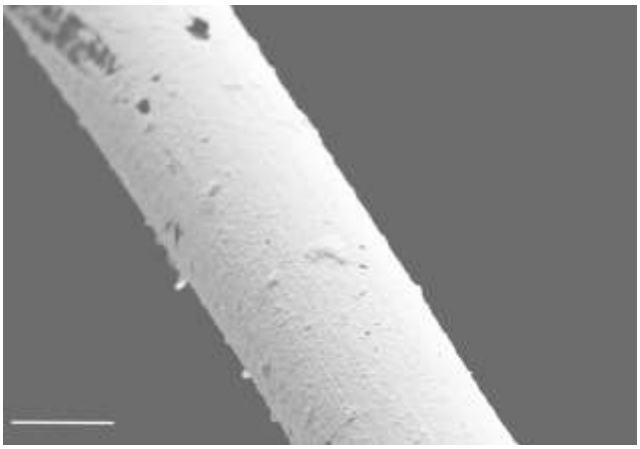

Figure 22. Gold plated copper wire section form 85 cm run. Scale bar is 10 microns.

Finally, we successfully loaded short PMIA fibers off the harvested frames into the mesofluidic chip and electroplated gold using the CBPE configuration, with a driving current of 0.27 µA over 250s, resulting in 150 nm thick gold film (Figure 23). Figure 23 is a FIB cross section of the plated wire, revealing a PMIA core with a sputtered copper core and an electroplated gold shell on the outermost layer.

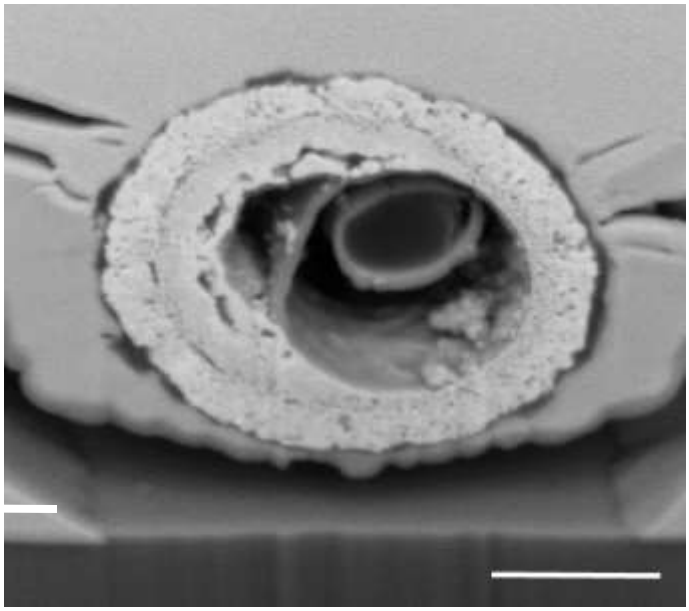

Figure 23. Gold-plated PMIA wire. Scale bar, 500 nm. The PMIA core used for this investigation had multiple concentric layers resulting from presence of $CaCl_2$, as described in Section 3.1.3.

This effort has demonstrated the feasibility of plating meter-scale lengths of fine fibers. Scaling up of metallization of the PMIA filaments can best be achieved by moving from sputtered deposition of seed layers to electroless plating integrated into the mesofluidic chip. In addition,

integrating polymer insulation following the metallization coating step would allow for a fully integrated reel-to-reel process from polymer backbone to fully functional wires (Figure 24)

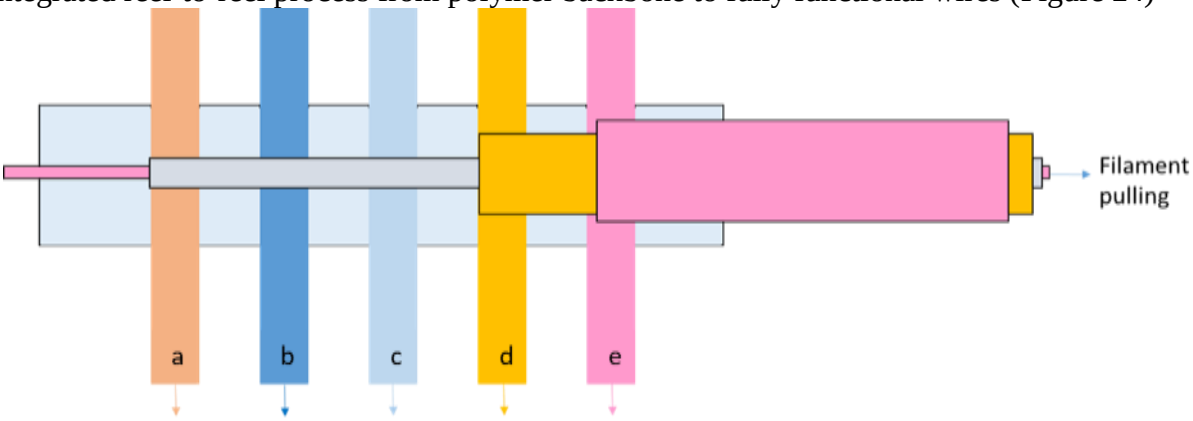

Figure 24. Schematic diagram illustrating a multi-stream approach to creating an insulated electroplated wire using an electroless strike on a polymer filament followed by electroplated metal and a final insulating polymer coating. The streams listed are (a) electroless metal, (b) saline, (c) rinse, (d) metal electroplating, and (e) polymer solutions.

3.3 Nanofiber Manipulation

3.3.1 Hydrodynamic Manipulation

After successfully fabricating wires of ~1 µm diameter and multi-centimeter length, we then developed methods to manipulate individual wires into the requisite hierarchically-twisted topology needed for suppression of skin and proximity effects. As illustrated graphically in Figure 4, wires of the dimensions used in the A2P program are difficult to manipulate using traditional mechanical approaches. First, they are fragile, and second, they tend to fly away uncontrollably due to common ambient forces such as air currents and electrostatics. The approached we developed utilized hydrodynamic drag to simultaneously screen ambient electrostatic forces and provide controllable tension to counter the tensile force exerted on the wires during twisting.

A schematic diagram of our process flow for twisting wires into bundles is shown in Figure 25. Briefly, fabricated wires are transferred from the processing frame onto individual silicon substrates (~0.8 mm x 0.5 mm x 25 mm). Wires are temporarily anchored to the silicon substrates using water-soluble polyacrylic acid (PAA) and are permanently attached to “mu-metal” discs of high magnetic permeability metal (~1.5 mm diameter), which are in turn temporarily attached to the silicon using PAA. After practice, this process was found to be highly repeatable (>90% yield) and relatively fast (<1 minute per wire).

After repeating the process for each wire in the bundle, the silicon substrates were inserted into individual capillary tubes in a custom fixture (Figure 25b). Once submerged, the water-soluble PAA dissolves, releasing both wires and mu-metal attachments. The fixture draws water through the capillary tubes to tension each wire individually.

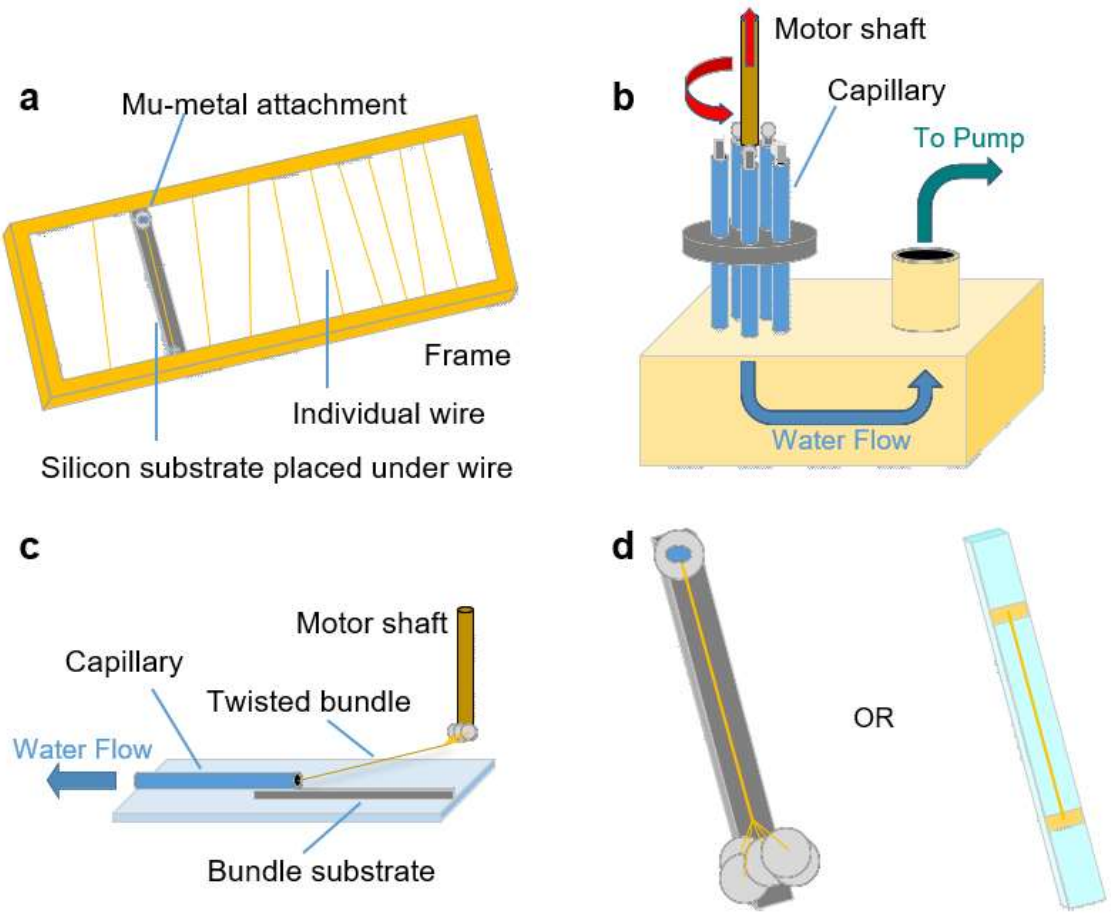

Figure 25. Twisting nano-litz bundles from individual nanowires. a, Placing an individual metal-coated PMIA nanofiber wire onto a silicon substrate, affixing with water-soluble adhesive, and attaching a disc of mu-metal to one end. b, Wires mounted on substrates are inserted into separate capillary tubes, and the entire apparatus is submerged in water. A pump draws water through the capillaries, releasing the water-soluble adhesive. The oversized mu-metal discs prevent the wires from being sucked into the apparatus, while flow tensions the wires within the capillaries. A motor shaft with magnetic tip placed in the center of the capillary array attracts the mu-metal discs, providing reversible attachment of wires to the motor shaft. To twist a bundle, the motor turns while the shaft is withdrawn from the fixture. c, After twisting, the free end of the twisted bundle is drawn into the capillary of a second fixture to provide tension while the bundle is placed on a new substrate. d, If the bundle will be twisted into a twist-of-twists, a new mu-metal disc can be attached to the bundle and the previous discs removed. If the bundle is to be electrically measured, it can be placed directly onto an electrical test substrate and bonded.

3.3.2 Assembly of Untwisted Bundles

Control bundles of nominally untwisted wires were assembled by harvesting wires directly onto a fixture having two adhesive tabs. Due to the small dimensions of the wires, it was challenging to accurately place wires into a bundle. To maximize yield and placement accuracy, a fixture was

fabricated to allow the sequential capture of fibers and allow placement and attachment to the adhesive anchors to be tightly controlled (Figure 26).

Two pieces of double stick kapton tape adhere to the fibers as they are placed. Placement of individual wires is achieved by lowering a frame of fibers onto the fixture while aligning an individual wire to the tape anchors. The tip of a hobby razor is used to press each end of the wire onto the tape anchors to ensure the fiber is captured in the adhesive layer on both ends. This process is repeated until the desired number of wires are captured.

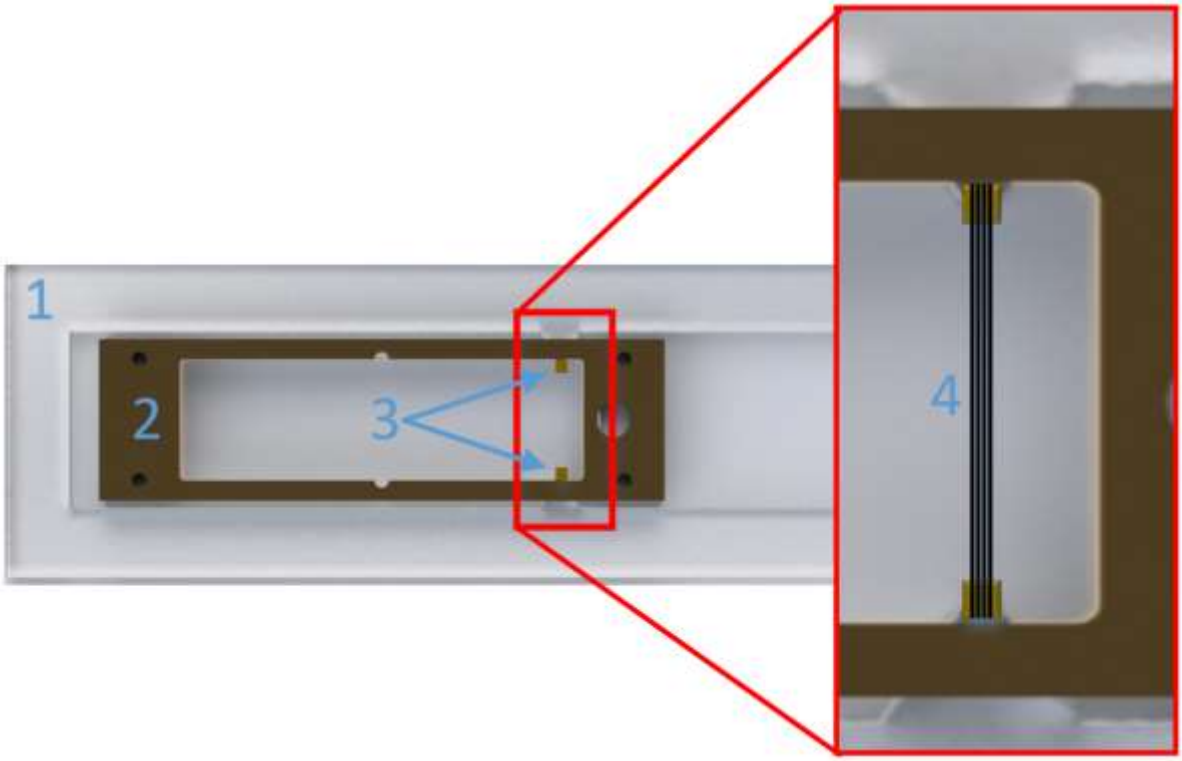

Figure 26: The setup for capturing untwisted nanofibers is shown. Number 1 represents the fixture, 2 the frame of wires, 3 the kapton tape, and 4 the nanofibers that have been captured previously.

After the wires have been attached to the tape anchors, an additional adhesive layer of UV cure epoxy is added to ensure the wires remain affixed to the kapton tape anchors even during immersion in water. The fixture containing wires is then slowly passed through an air/water meniscus with the bundle of wires oriented orthogonal to the plane of the meniscus. Capillary forces draw the wires together, collapsing the wires into a tightly-packed bundle. The bundle is then transferred onto a borofloat glass substrate for electrical testing (Figure 30). Interactions between the bundle and the substrate during the final transfer process occasionally cause the bundle to spread apart slightly, reduce packing density.

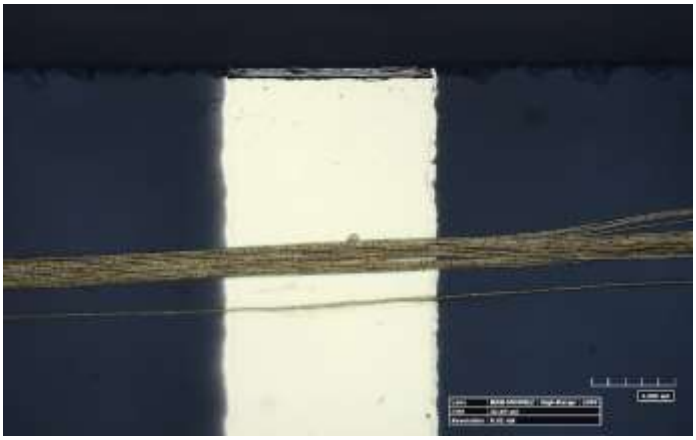

Figure 27: An untwisted bundle after transfer to a borofloat glass electrical measurement substrate. The bright yellow region is a Cr/Au bonding pad

3.3.3 Plectoneme Formation and Suppression in Flexible Filaments

Twisting filaments from one end can cause them to buckle and form 'plectonemes' – an effect familiar to many gardeners coiling garden hose. Our bundle twisting process relies on twisting from one end, so we wished to understand how the physics of helical buckling depended on wire length and other parameters. This information would enable us to determine whether this twisting approach could be used for significantly longer wires in a manufacturing context. Flexible filaments with low Young's modulus were made from silicone rubber (Oomoo 30 and Mold Max 30, Smooth-On Inc.). Silicone rubber compounds were mixed and degassed, and then cast into filaments by filling a custom aluminum shell enclosure with channels machined using ball end-mill bits to create cylindrical filaments. The filaments were cured for 24 hours and then released from the mold. Filaments were cut to varying lengths of 8-14 cm. Tensile testing (ESM301, Mark 10) was used to measure the Young's modulus of the filaments.

Filaments were loaded into a rotating fixture and submerged into a circulating glycerine tank (Figure 28). In order to mount the filaments axially and create a stable fluid transition from the rotary shaft to the filament, the silicone filaments were threaded into 1/16" outer diameter PEEK tubing of corresponding inner diamters and epoxied in place. The rigid PEEK tubing was then secured to a 3/8" threaded shaft with a nut and ferrule. The shaft was mounted via a gearbox to a 1:100 gear motor (Pololu, Inc.), and the angular velocity of the shaft was measured using a Hall sensor. The glycerine tank was circulated (Dayton Rotary Pump 1/2 HP, Grainger) through a flooded bath into a 4" diameter clear PVC pipe allowing for fully developed flow around the filament and also minimized optical distortion. Fluid flow rates were measured using a positive displacement flow meter (Omega). Due to the hygroscopic nature of glycerine, the viscosity was measured regularly (Brookfield Viscometer). Photos and video were taken from a head-on perspective using a digital SLR camera and video camera.

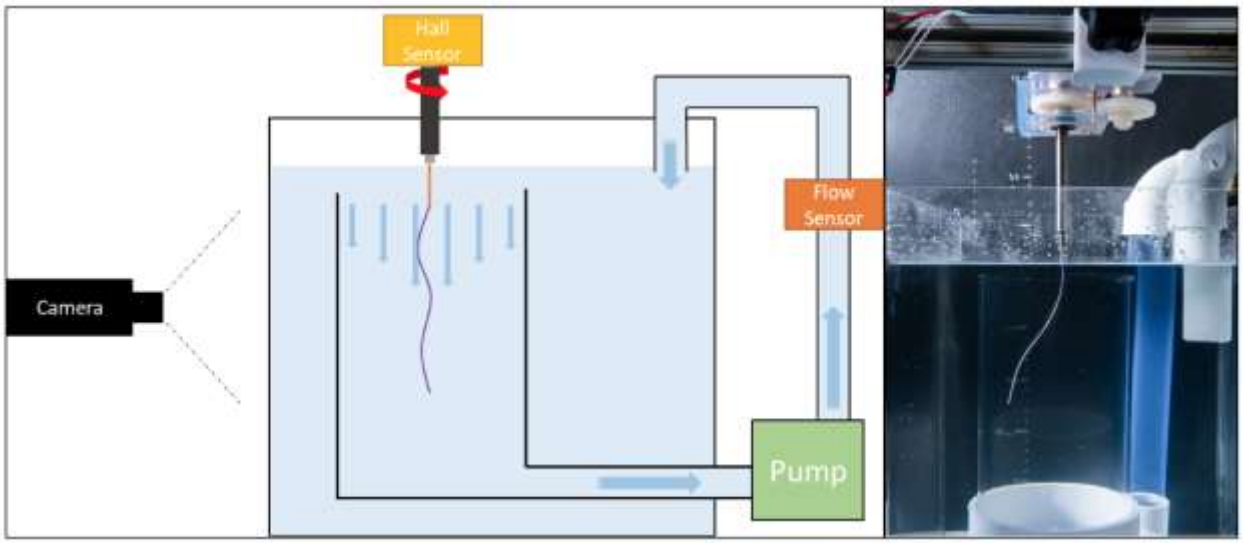

Figure 28. Experimental apparatus for twisting a filament immersed in a recirculating fluid bath. Left, Schematic diagram of apparatus. Right, Image of filament and tank

Table 1 lists the parameters varied experimentally and the associated observed events (stable, unstable, plectoneme).

Table 1. Experimental parameters of macroscale twisting experiments

a (μm)	*L* (cm)	*E* (MPa)	Flow rate (mL/s)	ω (rad/s)	η (Pa-s)	Behavior
381	12	1.43	0	6.4	0.9	Unstable
381	12	1.43	0	10.5	0.9	Plectoneme
381	12	1.43	0	21.0	0.9	Plectoneme
381	12	1.43	0	32.9	0.9	Plectoneme
381	12	1.43	0	49.4	0.9	Plectoneme
381	12	1.43	1.1	7.0	0.9	Stable
381	12	1.43	1.3	11.9	0.9	Stable
381	12	1.43	1.5	22.9	0.9	Stable
381	12	1.43	1.6	34.8	0.9	Stable
381	12	1.43	1.4	50.3	0.9	Plectoneme
381	11	1.43	0	7.6	0.9	Unstable
381	11	1.43	0	13.0	0.9	Unstable
381	11	1.43	0	23.8	0.9	Unstable
381	11	1.43	0	35.7	0.9	Unstable
381	11	1.43	0	52.2	0.9	Plectoneme
381	8	1.43	0	51.2	0.9	Unstable
381	8	1.43	0	7.8	0.9	Stable
381	8	1.43	0	11.9	0.9	Stable
381	8	1.43	0	22.9	0.9	Unstable
381	8	1.43	0	36.6	0.9	Unstable

381	8	1.43	0	52.2	0.9	Plectoneme
381	8	1.43	0.9	8.2	0.9	Stable
381	8	1.43	1.1	12.8	0.9	Stable
381	8	1.43	1.2	24.0	0.9	Stable
381	8	1.43	1.3	34.8	0.9	Stable
381	8	1.43	1.4	54.0	0.9	Stable
381	8	1.43	0.6	53.1	0.9	Unstable
381	11	1.43	0.8	7.7	0.9	Stable
381	11	1.43	0.9	13.0	0.9	Stable
381	11	1.43	0.9	23.8	0.9	Stable
381	11	1.43	0.9	37.5	0.9	Unstable
381	11	1.43	1	56.7	0.9	Unstable/Plectoneme
381	11	1.43	0.5	54.0	0.9	Unstable/Plectoneme
178	10	1.43	0	6.4	0.9	Plectoneme (double)
178	10	1.43	0	11.0	0.9	Plectoneme (triple)
178	10	1.43	0	22.0	0.9	Plectoneme (triple)
178	10	1.43	0	32.9	0.9	Plectoneme (multiple)
178	10	1.43	0	51.2	0.9	Plectoneme (multiple)
178	8	1.43	0	7.0	0.9	Plectoneme
178	8	1.43	0	12.1	0.9	Plectoneme (double)
178	8	1.43	0	23.8	0.9	Plectoneme (triple)
178	8	1.43	0	32.9	0.9	Plectoneme (double)
178	8	1.43	0	51.2	0.9	Plectoneme (multiple)
178	11	1.43	0	8.1	0.9	Plectoneme (double)
178	11	1.43	0	12.1	0.9	Plectoneme (double)
178	11	1.43	0	22.5	0.9	Plectoneme (triple)
178	11	1.43	0	32.9	0.9	Plectoneme
178	11	1.43	0	51.2	0.9	Plectoneme (multiple)
381	11.5	0.48	0	8.2	0.9	Plectoneme
381	11.5	0.48	0	12.6	0.9	Plectoneme
381	11.5	0.48	0	23.8	0.9	Plectoneme (double)
381	11.5	0.48	0	33.9	0.9	Plectoneme (double)
381	11.5	0.48	0	51.2	0.9	Plectoneme
381	11.5	0.48	1.3	8.4	0.9	Stable
381	11.5	0.48	1.5	12.8	0.9	Stable
381	11.5	0.48	1.6	23.8	0.9	Stable
381	11.5	0.48	1.5	34.2	0.9	Stable
381	11.5	0.48	1.6	51.2	0.9	Plectoneme
381	14	0.48	0	8.2	0.9	Unstable

381	14	0.48	0	12.6	0.9	Plectoneme
381	14	0.48	0	23.8	0.9	Plectoneme
381	11	0.48	1.2	4.4	0.9	Stable
381	11	0.48	1.3	9.2	0.9	Stable
381	11	0.48	1.4	21.0	0.9	Stable
381	11	0.48	1.6	32.9	0.9	Stable
381	11	0.48	1.7	51.2	0.9	Plectoneme
178	10	0.66	1.1	7.3	0.9	Stable
178	10	0.66	1.1	11.0	0.9	Stable
178	10	0.66	1.2	22.0	0.9	Stable
178	10	0.66	1.2	32.9	0.9	Plectoneme
178	10	0.66	1.2	47.6	0.9	Plectoneme (double)
178	8	0.66	1.2	6.2	0.9	Stable
178	8	0.66	1.3	11.7	0.9	Stable
178	8	0.66	1.3	22.0	0.9	Stable
178	8	0.66	1.3	32.9	0.9	Stable
178	8	0.66	1.4	43.0	0.9	Stable
178	8	0.66	0.6	45.8	0.9	Plectoneme
381	14	0.48	1.2	6.4	0.9	Stable
381	14	0.48	1.2	11.0	0.9	Unstable
381	14	0.48	1.1	22.0	0.9	Plectoneme
381	14	0.48	1.2	32.9	0.9	Plectoneme
381	14	0.48	1.2	47.6	0.9	Plectoneme

3.3.4 Elastocapillary Manipulation

In parallel to the fluidic manipulation described above for twisted bundles, we developed methods to *programmatically* assemble arbitrary braid topologies at the nanoscale *without damaging* the delicate fibers. Mechanical approaches that are widely used in industry to fabricate complex braids are unsuitable for this purpose because (1) each machine is expensive and can make only a limited number of topologies, and (2) these machines work with fibers or wires that are typically 100 micrometers in diameter or larger; fibers smaller than this can easily break.

Our approach takes advantage of repulsive capillary forces to effectively trap and move small pieces of PDMS ("floats") at the air/water interface inside channels of our devices (Figure 29). Although capillary forces have been widely used in self-assembly [7]–[13], repulsive capillary forces, which arise from two interacting surfaces with opposite signs in wettability[14], are often overlooked. To braid wires, we tie them to the floats and fill the device with water. The inner surfaces of the device are shaped so that as the water level changes, the repulsive capillary forces on the floats change, causing them switch places in a sequence according to the desired braid (Figure 29).

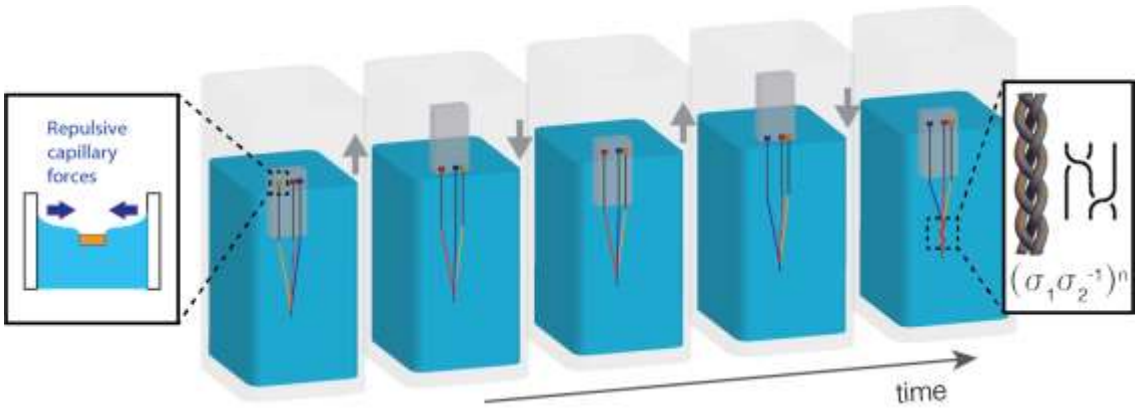

Figure 29. Braids are formed when the device (in gray) is cycled up and down in water. Inside the device we place floats that are attached to wires. As shown in the left inset, the floats are repelled from the walls of the device by capillary forces. To ensure that these forces are repulsive, the contact angle of the float must be opposite from that of the device. As the device moves, the change in shape of the meniscus drives the floats to move in a prescribed pattern. The wires also move in that pattern to form braids. The 3-strand braid commonly seen in hair is shown as an example on the right, along with its mathematical braid-group description.

3.4 Electrical Measurements

While a direct frequency-dependent measurement of AC resistance R_{AC} would be ideal, this is not possible at GHz frequencies. At GHz frequencies, it is typical to use a vector network analyzer (VNA) to measure the amplitude and phase of reflected and transmitted power waves (called S-parameters); device characteristics are then deduced from analysis of the amplitude and phase information of the S-parameters. Our primary measurement approach was designed to measure the resistive losses in straight sections of wire at a single frequency with maximum sensitivity. Samples were mounted and electrically bonded to contact pads on electrically-insulating, rigid substrates. Due to both impedance mismatch between feed lines and the sample as well as the indirect capacitive coupling, the samples formed resonant cavities whose transmission and reflection characteristics could be probed. This measurement approach had several advantages: it minimized the amount of sample manipulation required for mounting; it allowed repeated measurements of various samples without further mechanical manipulation of the samples; it was relatively insensitive to sample position; it permitted use of high-quality microwave SMA connectors to increase repeatability; and it increased the measurement sensitivity by enhancing the interaction time with the sample at the cavity resonance. This last advantage was important only in light of the relative immaturity of nano-litz bundle manufacturing capability. For larger bundles containing a greater number of strands, the scale of performance enhancement increases, obviating the need for such sensitivity.

For the majority of our electrical measurements, sample bundles and wires were placed approximately straight onto narrow pieces of borofloat glass (dimensions 0.7 mm x 0.525 mm x 30 mm) and PEG bonded to Cr/Au contact pads spaced 6.0 mm apart (as shown in Figure 25). Once placed and bonded, samples could be probed via the contact pads to measure DC resistance

and could be reversibly placed onto a custom measurement fixture for measurement of high-frequency characteristics.
The typical resistance of wires and bundles were within ~20% of predicted values based on typical wire diameters (as measured by FIB cross-section and electron microscopy) combined with measured electrical resistivity of witness samples sputtered concurrently with wires (which for sputtered Au, ranged from 5.2e-8 to 6.5e-8 Ω-m).

Because individual strands of wire are insulated in litz bundles, it is important to note that we were able to develop strand insulation characteristics (in particular, aluminum oxide deposited via atomic layer deposition) and PEG bonding techniques that resulted in high-quality electrical contacts via direct bonding to electrical contact pads (Figure 30).

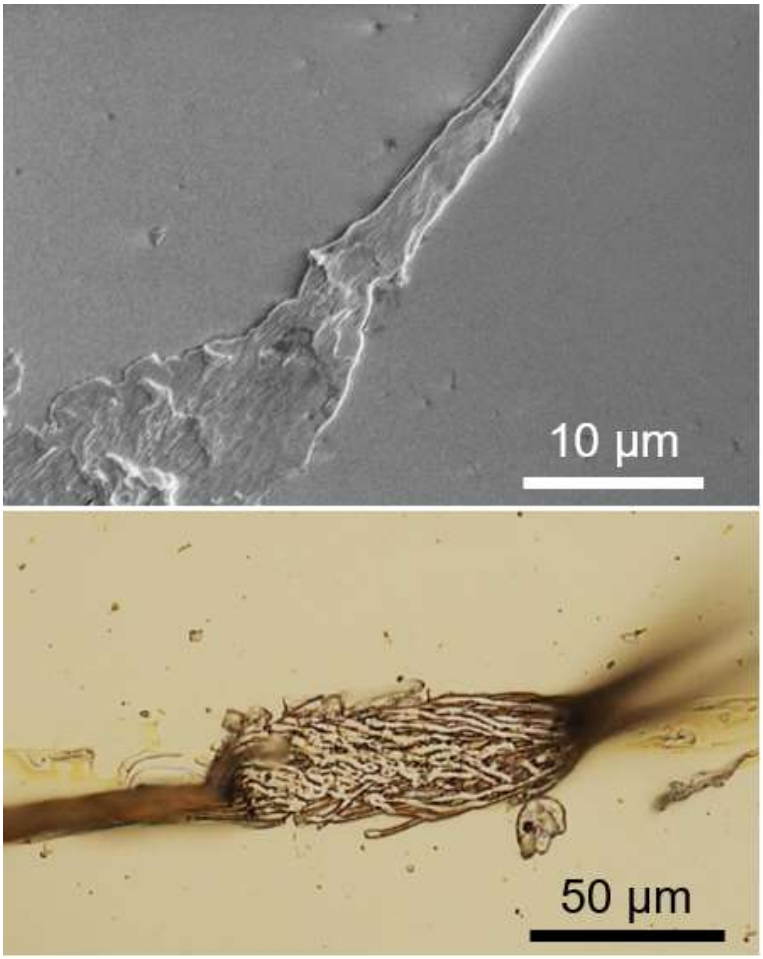

Figure 30. Wire bonding individual metal-coated PMIA nanofibers (top) and nano-litz bundles of ALD-insulated wires (bottom)

The resonant-cavity measurement fixture (Figure 31) is a micro-strip structure etched from Copper on a Rogers (low dielectric constant) substrate. SMA terminals are soldered onto the signal feedlines (Figure 33) and ground planes of the fixture, enabling two-port network measurements on an Agilent Vector Network Analyzer (Model Number: E8363B). In addition to the resonant structures used to measure characteristics of samples, the fixture also included calibration structures to allow a Through, Line, and Reflect (TRL) calibration. This calibration removes RF

response occurring from test cables, SMA connectors, and copper feedlines, such that final measurements represent the electrical response of only the sample and sample substrate.

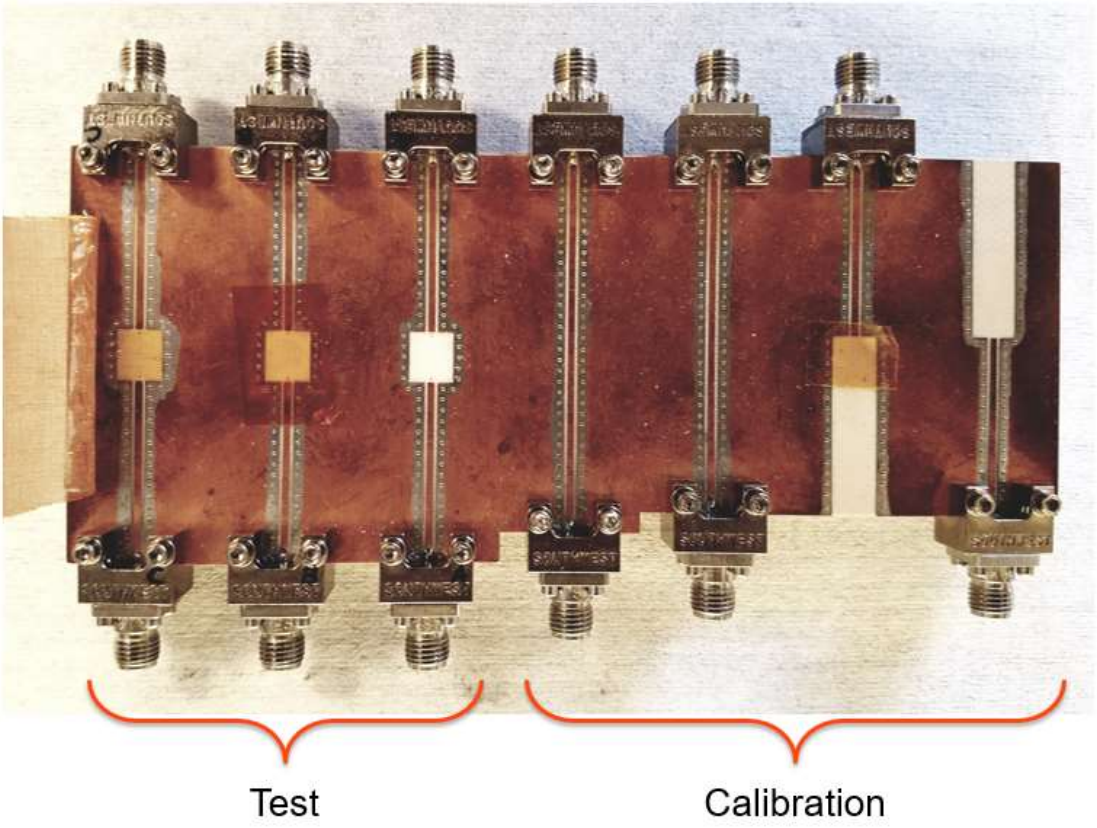

Figure 31. Optical image of resonant cavity measurement fixture

The sample substrate is mounted on a translation stage (Figure 32) that allows for 6-axis (X-Y–Z, pitch-tilt-yaw) adjustment of sample alignment along the feedlines of the RF resonant-cavity fixture. The Borofloat-mounted sample is held in a planar, 20-mil thick Ultem Sample Mount Vise that is attached to a COTS XYZ-linear translation stage attached to a 3-point contact plate, which allows pitch and tilt adjustment. The Sample Mount Vise can rotate in the x-y place (yaw), enabling the sample substrate to be precisely placed on or above the resonant cavity measurement fixture.

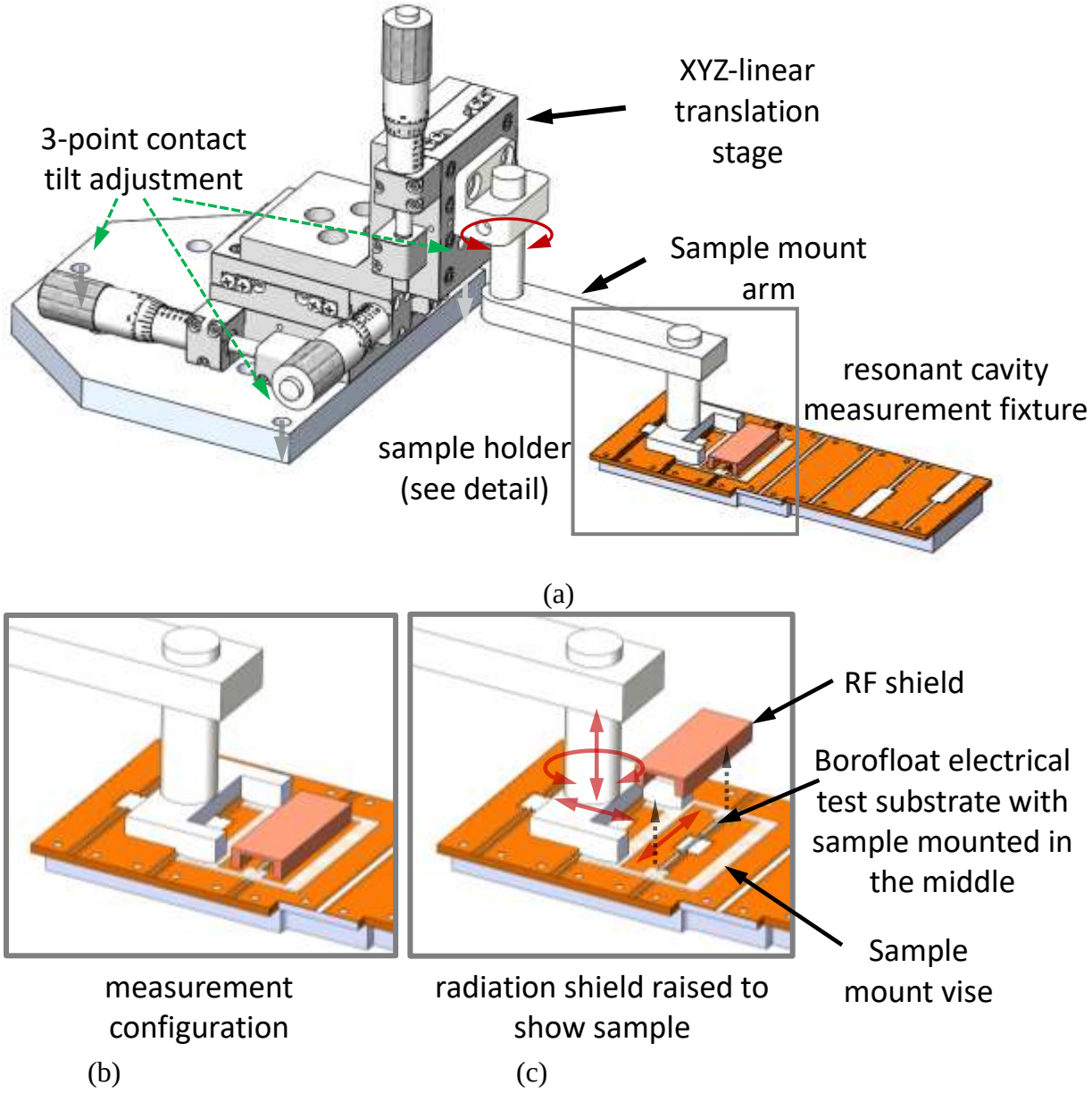

Figure 32. (a) RF measurement positioning fixture. Detail images b and c show how the sample is placed on the test board.

This fixture is used to align the structure such that it is symmetric relative to both ports. This alignment can be done live by viewing the magnitude of the reflected signal on port 1 (S_{11}) and port 2 (S_{22}) relative to an input voltage. By viewing S_{11} and S_{22} simultaneously on a log scale vs frequency it is simple to adjust the micrometer aligned along the axis of the sample until the magnitude of S_{11} and S_{22} align to each other. Alignment can also be checked visually using an optical microscope (Figure 33) to verify that both ends of the sample are aligned and approximately equally spaced from the copper feedlines.

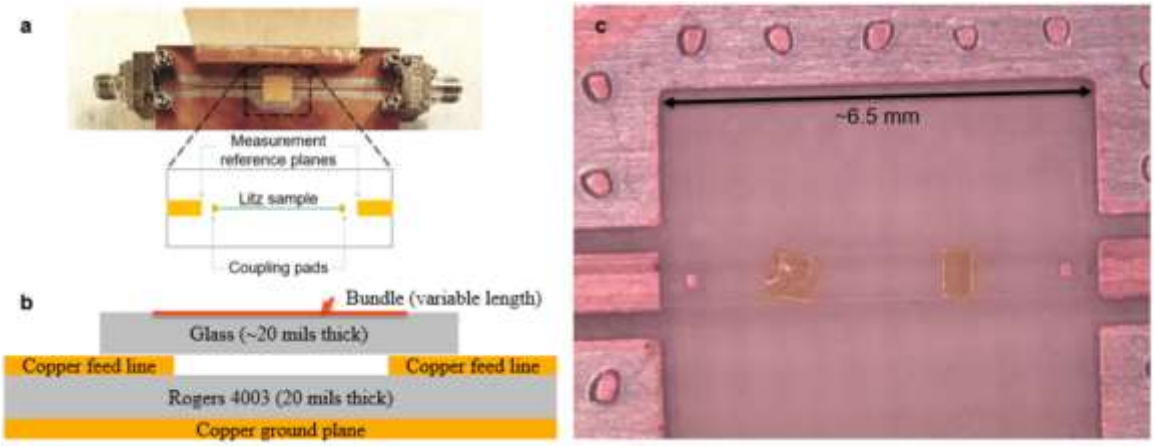

Figure 33. Resonant-cavity measurement fixture. a, Optical image of a measurement channel on the text fixture.

After alignment, a measurement of the sample is taken anywhere between 50 MHz – 25 GHz using 1601 data points, a 3.0 kHZ IF bandwidth, and a stepped sweep with a dwell time of 1.0 msec. Each tenfold reduction in the IF bandwidth lowers the noise floor by 10 dB. By using a stepped sweep the analyzer source is tuned, waits 1.0 msec prior to taking a measurement at that frequency data point, then tunes the source to the next frequency data point. Both the IF bandwidth and stepped sweep allows for a cleaner and accurate measurement. All measurements are stored as .s2p files for data analysis.

3.5 Determination of Quality Factor

Accurate determination of the 'unloaded' quality factor, Q, can be challenging. The majority of our measurements were two-port measurements in which the sample under test formed a resonant cavity. Following Refs. [15]–[17], the unloaded Q factor was determined from a combination of reflection (S11 and S22) and transmission (S21) S-parameters. A key component of this analysis is the concept of a "Q-circle," as illustrated on the Smith chart of Figure 34. The diameter of these circles is related to the strength of the coupling between the resonator and the feed lines.

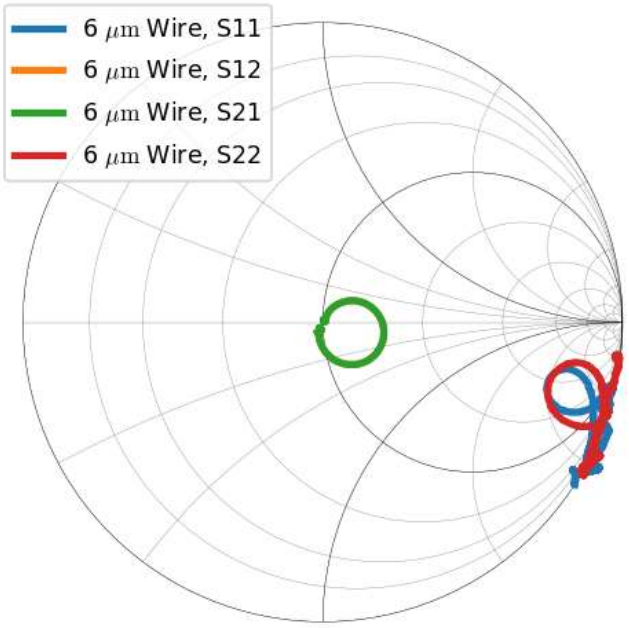

Figure 34. Example Smith plot of a ~6 µm diameter control wire measured in the resonant transmission fixture

One of the primary challenges for determining unloaded Q is fully understanding and characterizing the strength of the coupling to the resonator. For a weakly coupled resonator, one can simply use the transmission (S21) measurement to determine $Q \sim f_0/\Delta f_{3dB}$, where f_0 is the resonant frequency (i.e. frequency of the maximum of the S21 trace) and Δf_{3dB} is the width in frequency at the point 3dB below the maximum. As the coupling between the resonator and the feed lines increases, however, the measured width of the transmission resonance increases. Simply measuring the width of the transmission resonance is therefore not a reliable indicator of the losses within the cavity. If the coupling to the resonator is perfectly symmetric, then the effect of the coupling can be easily estimated using the magnitude of the transmission S21 measurement, but the assumption of symmetric coupling is in general not valid.

To more accurately account for the effects of coupling to the resonator, we utilized both reflection and transmission S-parameters. As illustrated in Figure 35, a bilinear function was fit to the complex S21 transmission data, enabling accurate characterization of the loaded Q. Coupling constants to each port were separately determined from the diameter of the S11 and S22 Q-circles. As discussed in Ref. [17], frequency-dependent transmission line coupling can distort the S11 and S22 Q-circles to be 'balloon' shaped rather than circular. In our case, accounting for this distortion is simplified because of the high impedance of our samples relative to the 50 Ω impedance of the transmission lines, since the large impedance causes the perimeter of the off-resonant S11 and S22 traces to lie on the edge of the Smith chart. The diameters of the circles can therefore be simply estimated based on the distance to the edge of the Smith chart without needing to actually characterize the magnitude of the frequency-dependent phase shift responsible for the distortion.

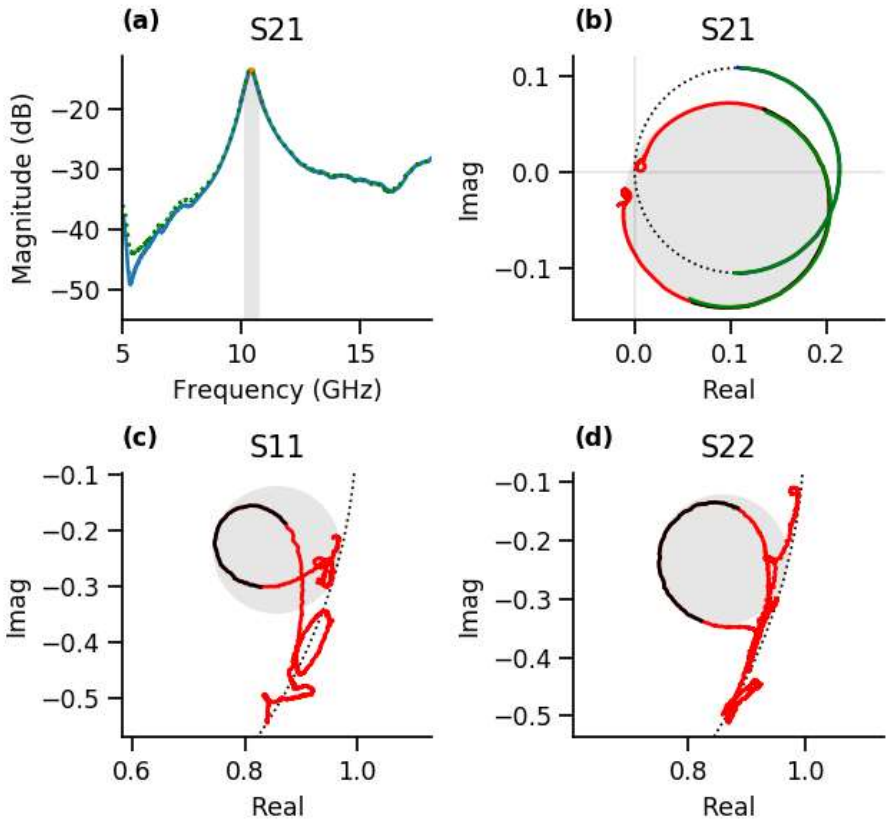

Figure 35. Example Q-factor extraction procedure from the same sample shown in Figure 34. (a), Transmission (S21) magnitude versus frequency. Gray band indicates region within 3 dB of peak that is used for fitting bilinear function for Q-factor extraction. (b-d), Real versus imaginary components of transmission (S21) and reflection from either port (S11 and S22).

3.6 Modeling Litz Wire in the GHz Regime

Many have analyzed and modeled litz wire at low frequency but an open question is whether inter-strand capacitance would make litz wire stop working at high frequency. In order to answer this question we developed a lumped model to specifically probe the effects of inter-strand capacitance.

Figure 36 shows examples of lower frequency litz wire. As was discussed earlier, the approach taken here is to use a combination of circuit-element and mesh-based EM simulation to examine litz optimization.

Figure 36. Example Litz Wire

The circuit element model chosen is based on many other RF models, using inductance, resistance, and capacitance to estimate RF effects. The model for a single section is shown in Figure 37. The advantage of the circuit model is that it can be quickly scaled up to 8, 15, or 25 strands.

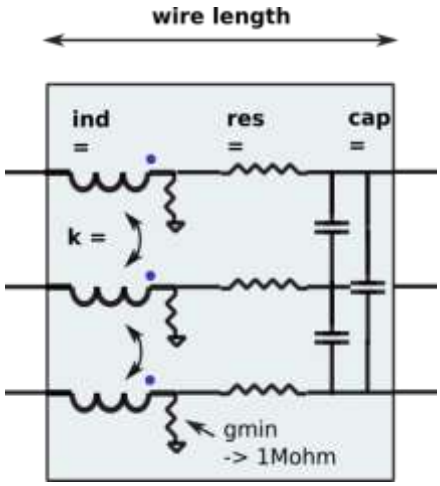

Figure 37. Three-strand circuit-element model of a short section of three straight, parallel wires. A model of a realistic bundle would be represented by multiple sections connected in series. Twisting or braiding can be represented by varying the circuit parameters appropriately in different sections.

We want sections to be < to 1/8 wavelength at the highest frequency of interest, say 20 GHz.

$$\lambda = \frac{c}{f} = \frac{3e8}{20e9} = 15mm \rightarrow \frac{1}{8}\lambda = 1.8mm$$

A smaller length section will model a smaller portion of a wavelength and give results closer to reality.

Moving forward, the three-strand model can be increased to eight strands as in Figure 38. Model sections can be connected in a serial fashion (Figure 39), and then simulate the winding of a litz bundle using cross-connections of the series elements as shown on the right of Figure 38.

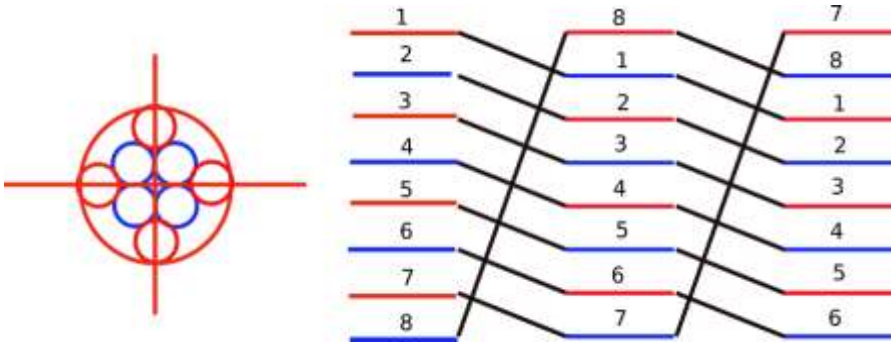

Figure 38. Series Cross-Connection of sections for modeling Litz Effect

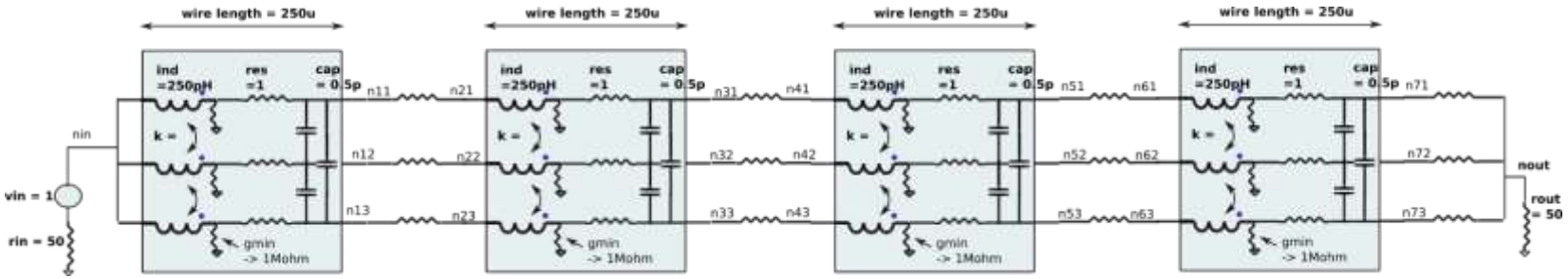

Figure 39. Example Series Connection of Circuit-Element Sections

3.6.1 Wire self- and mutual inductance

3.6.2 Self-inductance:

For self-inductance of a wire we use a simplified formula: $L_{self}=2*length*(log(2*length/radius)-3/4)$

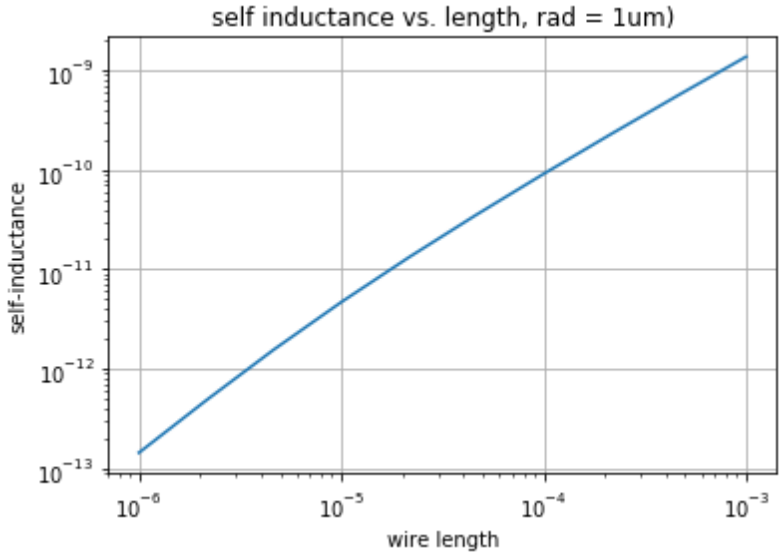

Figure 40. Analytic Self Inductance(nH) vs. Length(log meters)

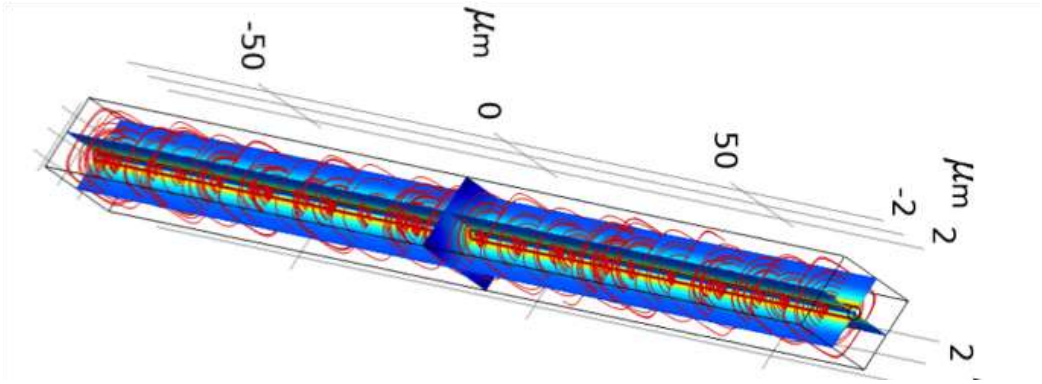

Figure 41. 250 μ m Length Wire Inductance EM simulation

The EM simulation self inductance result for the 250 μ m length is 190 pH, which agrees closely with the analytical result at 250um on the x axis (Figure 40).

3.6.3 Mutual inductance:

The equation for mutual inductance between two wires is:

$$L_{ind} = \left(\frac{\mu_0 * length}{\pi} \right) * ln \left(\frac{separation}{radius} + SDfactor \right)$$

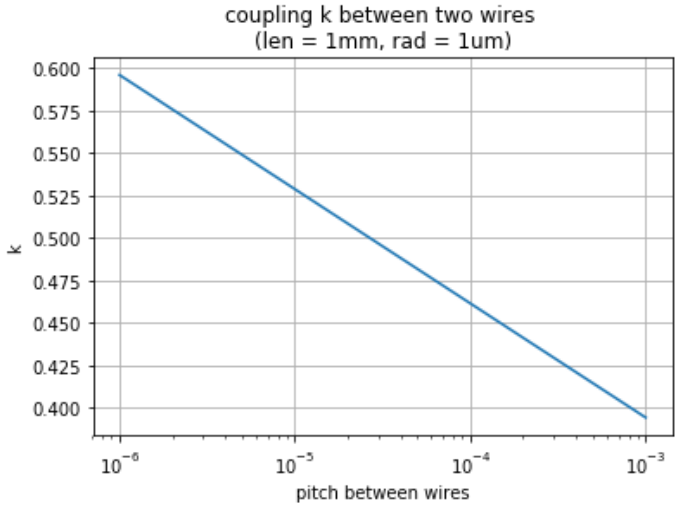

Figure 42. Mutual Inductance(k factor) vs. Separation (log meters)

EM simulation is being carried out to confirm the analytical model.

3.6.4 Modeling proximity effect: the effect of mutual coupling on current distribution

The goal here is to use the circuit model in Figure 37 to examine the simplest mutual inductance between strands in the model by looking at currents in each strand. The strands are placed as shown in Figure 43.

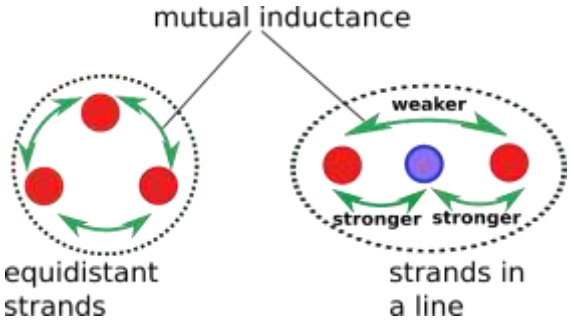

Figure 43. Outer to Outer Coupling 1/2 of Inner to Outer Coupling

First the equidistant strands are simulated, with same wire-wire mutual coupling (Figure 44). The red and blue lines don't have meaning in this case as the strands are equidistant.

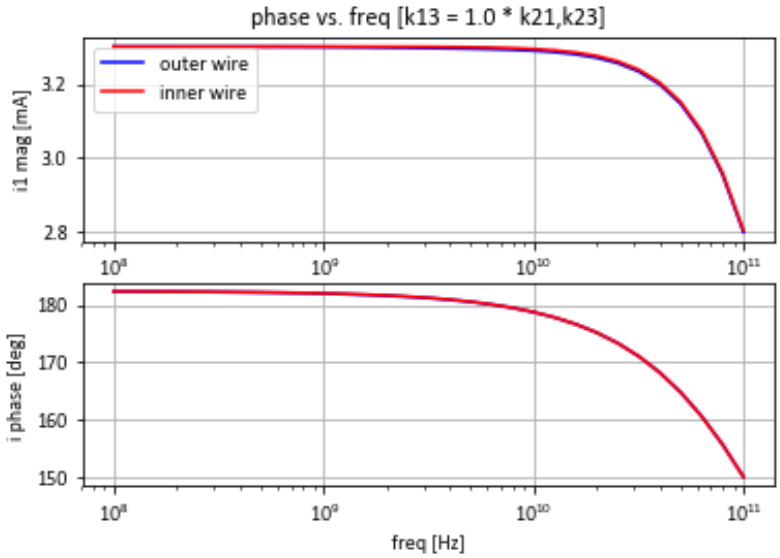

Figure 44. All wire-wire Coupling is Identical

Next the in-a-line placed strands are simulated, with weaker outer coupling (Figure 45). The red plotline shows the AC current in an "outer" wire. The blue plotline shows AC current in the inner wire. As expected from proximity effect, current flows preferentially in the outer wires.

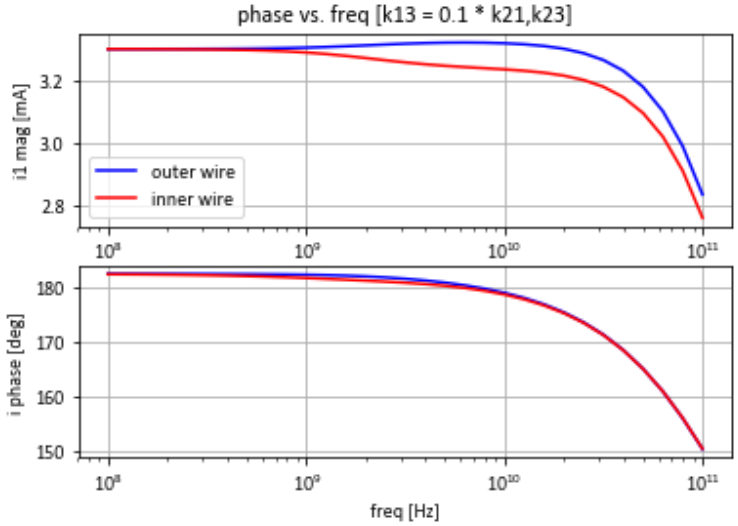

Figure 45. Wires in a plane: Outer-to-outer coupling is 1/2 of inner-to-outer coupling

The outcome of these simulations and analysis are to test the model as a basic structure to look at stand-to-strand inductance and coupling. Generally the interpretation is that this approach is viable to examine the more complex interaction between strands in a litz bundle.

3.6.5 Capacitance vs. strand-strand separation

There has been some concern that closely coupled wires may increase wire-to-wire capacitance such that it becomes a noticeable litz-effect degradation. Larger litz wires have thicker insulation

which reduces capacitance. The wire-to-wire capacitance was calculated vs. wire-wire distance, then used in a circuit model to observe the coupling capacitance effect on simulated strand-to-strand current.

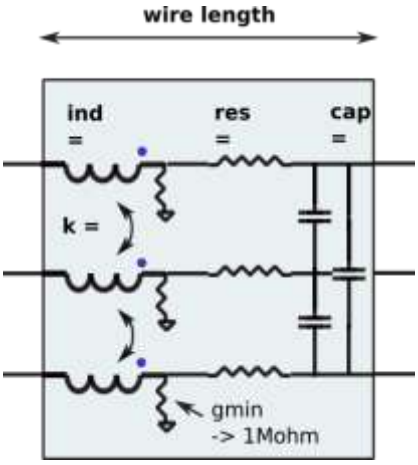

Figure 46. Coupling Capacitance model

One standard equation used to calculate wire to wire capacitance is:

$$C = \frac{\pi * \varepsilon_0 * wireLength}{ln\left(\frac{pitch}{2*radius}\right) + \sqrt{\frac{dist^2}{4*radius^2} - 1}}$$

Figure 47 shows electric field and surface potential EM simulation results on closely spaced strands. These outputs are used to extract simulated between-wire capacitance to compare to the analytical model.

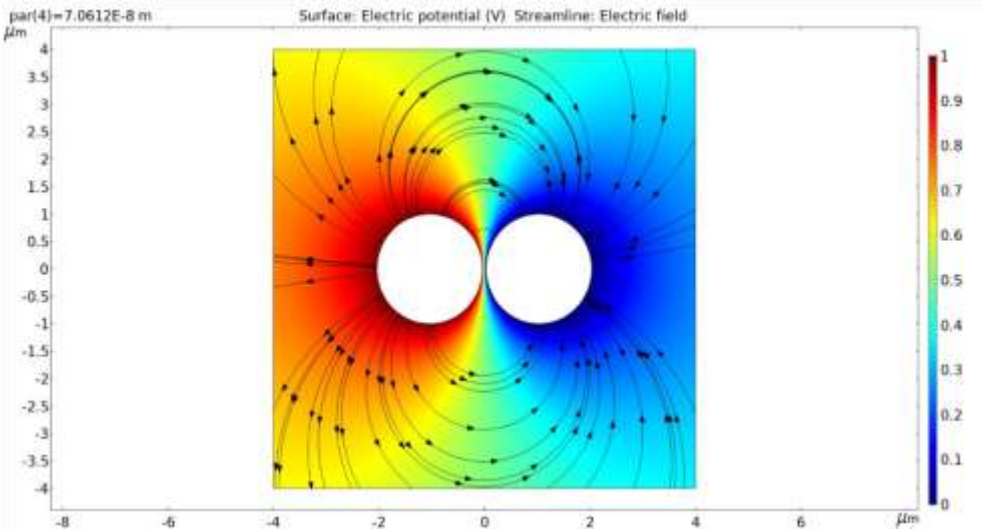

Figure 47. Electric fields and surface potential between wires in a finite element simulation of two parallel wires.

Figure 48 shows a comparison of EM and analytical results, which were found to be in approximate agreement.

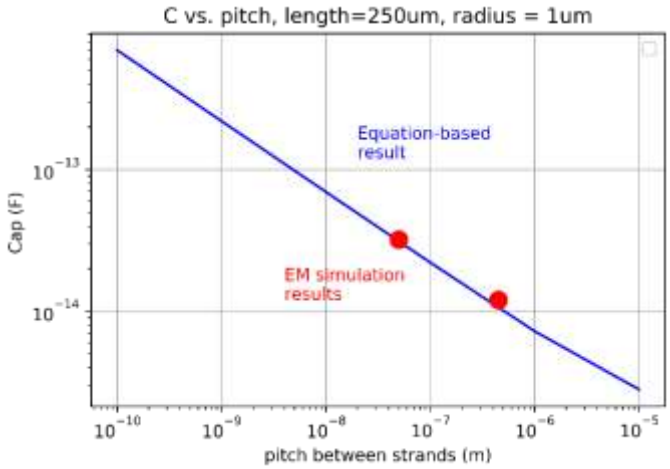

Figure 48. Capacitance between two parallel wires as a function of center-center distance between wires calculated two ways: (1) using the above equation and (2) using the finite element simulation software COMSOL

The goal of the modeling approach is to use a mix of EM and circuit models to allow fast simulation of gross effects and single-point verification and comparison with detailed mesh-based models.

Figure 49 (lower) shows that at 10 GHz, a geometrically impossible large capacitance results in a visible effect in current between inner and outer wires in a 3 wire bundle. Conversely, a 100fF or lower capacitance from a separation of 20nm as shown in Figure 49 (top) has little effect on current in strands.

The result then, is that inter-strand capacitance, as implemented in the model shown in Figure 37, is likely not a risk in litz wire design at GHz frequencies.

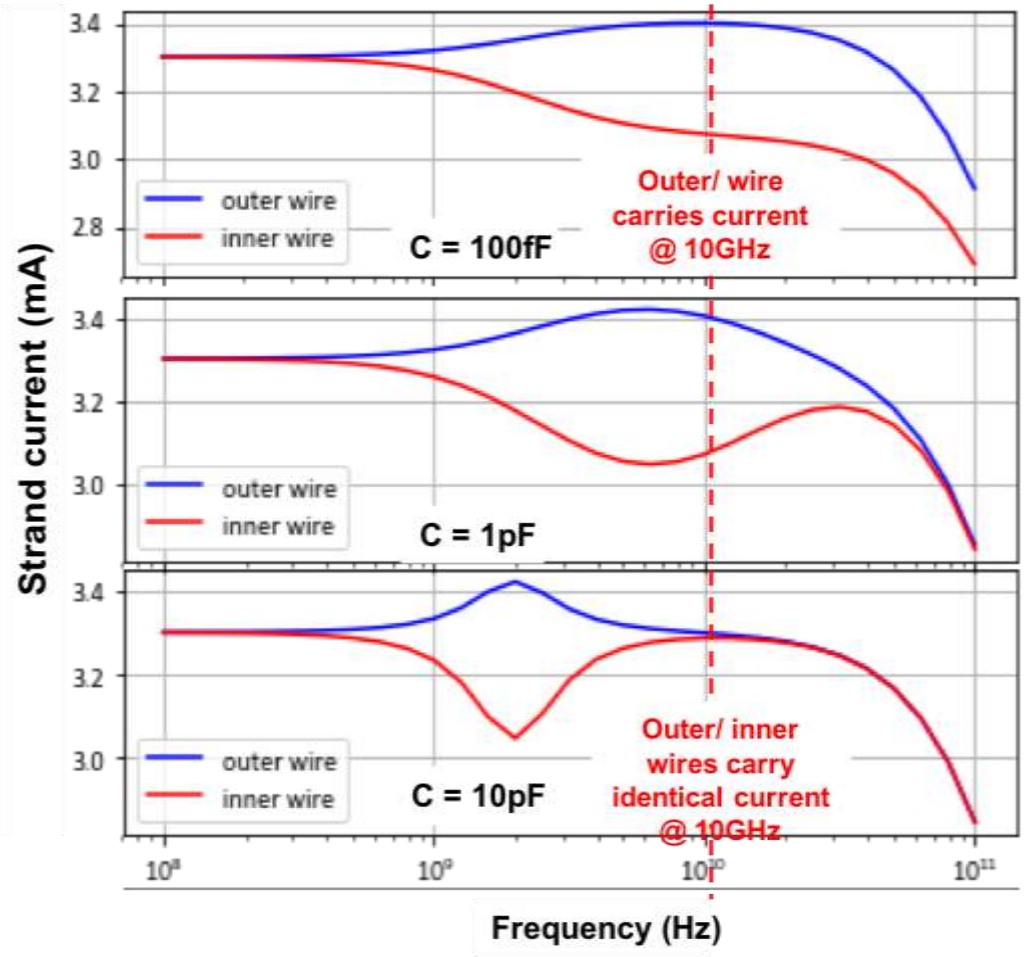

Figure 49. Effect of cap on current/freq.

4 RESULTS AND DISCUSSION

4.1 Electrical Performance of Nano-Litz Bundles

A key outcome for this program was the experimental demonstration that nano-litz wire can outperform solid wire at GHz frequencies. As described in Section 3.4, straight sections of wire were mounted on rigid substrates and were coupled to a custom test fixture to create resonant cavities. The transmission characteristics of these resonant cavities were probed using a vector network analyzer (VNA) in a 2-port measurement to determine the amplitude and phase of the reflected and transmitted S-parameters. The quality factor, Q, of the transmission resonances were used to characterize ohmic loss in the samples at high frequency. At low frequency, the DC conductance of samples ($G_{DC} = 1/R_{DC}$) was measured using a probe station.

In a normal wire in the skin effect regime, current flows only on the surface of the wire in an area approximately proportional to the wire circumference (and hence wire radius, r). For properly designed litz wire, current should flow through the entire metal cross-sectional area, scaling instead with radius squared, r_e^2, where $r_e \propto G_{DC}^{1/2}$ is the radius of an equivalent wire with equal metal cross-sectional area.

We observed the predicted difference in scaling between nano-litz wire and conventional wire by comparing a series of nano-litz samples, thick solid wires, and 'simple bundles' of wires arranged in a non-ideal packing (Figure 50). For each sample, S-parameters were measured and unloaded quality factor Q was extracted as described in Section 3.5 (Figure 50a). The example traces shown in Figure 50a all have similar DC resistance (R_{DC} = 9.91 Ω, 8.95 Ω, and 10.48 Ω for the nano-litz, solid, and simple bundle, respectively) yet show clear differences in the width of their transmission resonances. Calculations of R_{AC} at the resonant frequency (~11 GHz) using the analysis described in Ref. [18] predict that ohmic losses in the solid wire sample and in the simple bundle should be ~1.75x higher than in the nano-litz sample (Figure 50b). Extracted Q-factors plotted versus $G_{DC}^{1/2}$ were overlaid with predicted values of Q for the different sample types, showing a qualitatively different dependence for the nano-litz samples, in excellent agreement with the predicted dependence (Figure 50c).

The calculations of predicted R_{AC} used measured (typical or average) parameters whenever feasible (Table 2). Metal resistivity and strand diameter were typical/average measured values; the Q of the test fixture itself ($Q_{Fixture}$) was estimated using finite element simulations of the fixture with measured values of loss tangent for all dielectric layers in the system. The configurations of bundles used to model nano-litz wire are given in Table 3. The lines in Figure 50c indicate predicted Q for perfect packing density assuming close-packed circular wires, as in Ref. [18] and accounting for the decreased packing density of twisted wires [19]. Shaded regions adjacent to the lines for nano-litz and simple bundles indicate the impact from sub-optimal packing factors of 50% and 10% of optimal for nano-litz and simple bundles, respectively.

Although our goal is to characterize R_{AC}, we are only able to directly measure $Q = \omega L/R_{AC}$, where L is the inductance of the wire as measured in the test fixture. While L is only logarithmically sensitive to the radius of the wire or bundle [20], this effect becomes non-negligible for thicker wires or for very loosely packed bundles. As can be seen in Figure 50c,

two of the simple bundles have Q that is significantly lower than the predicted value. From Figure 50b, we expect the simple bundle to have R_{AC} equal to that of a solid wire; the reason for the low Q of the simple bundles is that they are very loosely packed. These bundles were attempts at bundles of parallel wires, but without even loose packing to hold the bundle together, wires spread horizontally across the sample substrate during mounting. The measured width of the simple bundles was more than 100 µm in places, drastically reducing the inductance of the bundle.

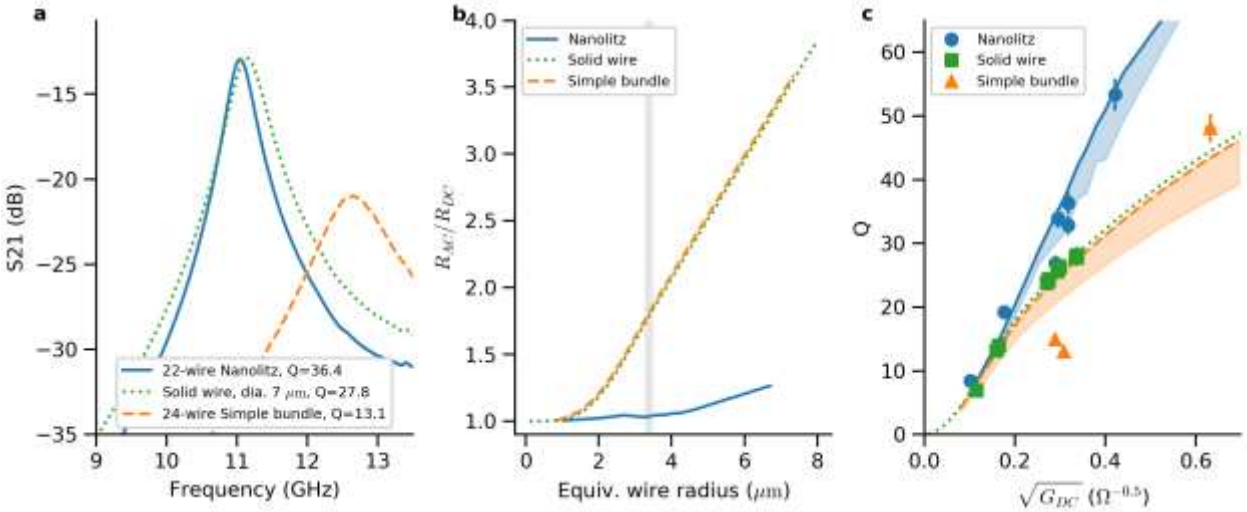

Figure 50. Experimental measurements of nano-litz performance benefit at GHz frequencies for sputtered gold wires. (a), Measured transmission scattering parameter S21 plotted for three representative samples. Unloaded Q extracted for each sample is indicated. (b), Calculated resistance ratio R_{AC}/R_{DC} versus wire radius at 11 GHz for each type of sample. For wire bundles, radius used is of an equivalent wire with equal metal cross-sectional area. The curves for solid wire and non-litz bundle are indistinguishable. (c), Unloaded Q vs $G_{DC}^{1/2}$. Points, extracted unloaded Q factors from experimental data. Lines, predicted values using the analysis in (b). For nano-litz and simple bundles, shaded regions indicate the range of Q expected from sub-optimal fill factor.

Table 2. Properties used in analytical model of Q

Property	Value	Unit
Wire/bundle length	6.5	mm
Metal resistivity	5.4e-8	Ohm-m
ALD insulation thickness	20	nm
Nano-litz strand diameter	1.2	µm
Frequency	11	GHz
$Q_{Fixture}$	150	dimensionless
Wire-ground separation	1.033	mm

As described in Section 3.5, it can be challenging to accurately measure Q of a resonator, particularly when it is highly coupled to feed lines. To verify that the values of unloaded Q that

we extract from data is not overly influenced by coupling, we measured Q (and resonant frequency f_0) while the samples were physically raised off of the test fixture (Figure 51). Despite a strong reduction in peak transmission (as measured by the maximum in S21), the measured Q only increased ~10% as the height Z increased by 1 mm. This modest improvement in Q is in agreement with finite element modeling of the system and is attributed to reduced absorption in the Rogers substrate. As Z increases, a greater proportion of the cavity mode resides in the (lower-loss) air region above the Rogers substrate as opposed to within the (relatively higher-loss) Rogers substrate.

Table 3. Nano-litz bundle configurations used for analytical modeling. Bundle configuration is indicated following industry convention: N/M denotes N bundles of M strands, each twisted in the same chirality (although typically with different pitch for each level). (Different chirality is conventionally indicated by NxM.)

Bundle configuration	Equivalent wire radius (μm)
3/1	1.04
5/1	1.34
3/3	1.80
3/4	2.08
3/5	2.32
5/4	2.68
5/5	3.00
3/3/3	3.12
2/5/3	3.29
4/3/3	3.60
2/5/4	3.79
5/3/3	4.02
2/5/5	4.24
3/5/4	4.65
5/5/5	6.71

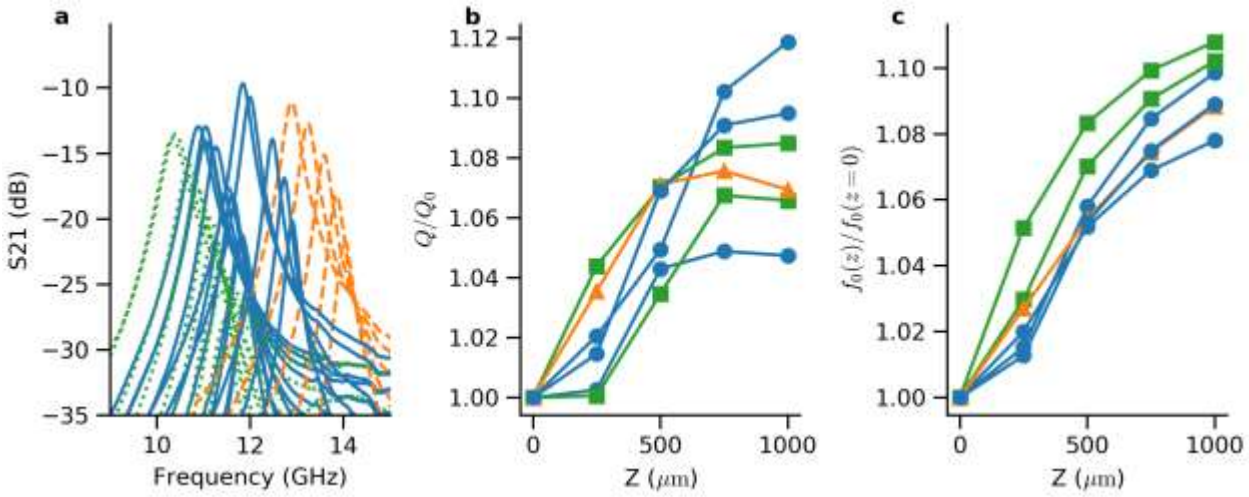

Figure 51. Dependence of sample Q on distance above test fixture, Z.

4.2 Applications.

4.2.1 Nuclear Magnetic Resonance (NMR).

NMR spectroscopy is an incredibly powerful tool used in a wide variety of fields because it can provide detailed information about molecules' bonding, structure, dynamics, and environment. A key limitation for even more widespread use, however, is the inherently low sensitivity of NMR. As summarized by a working group of researchers convened specifically to address issues of low sensitivity in NMR[21], "If it were not because of restricted sensitivity, the potential of NMR spectroscopy would be nearly boundless." The signal measured in NMR, a weak fluctuating magnetic field caused by precessing nuclear spins, is detected using inductive coils called probes. The resistance of the probe coil is one of the primary factors that limits sensitivity in NMR[22].

One of the largest improvements to signal to noise ratio in NMR has come with the development of cryoprobes[23], and it is useful to use the scale of this improvement as a benchmark for what could be achieved with litz wire. Cryoprobes are probes that are cooled to cryogenic temperatures, where the resistivity of the probe metal is reduced to 10-25% of its value at room temperature. It is worth noting that this reduction in resistivity does not translate to a proportional improvement in the Q of the probe because of skin effect. As the wire is cooled and resistivity decreases, the skin depth also becomes smaller (see Eq. 1), squeezing the current into a thinner cross-sectional area. This fact, coupled with the need for thermal insulation between the probe and the sample, results in an overall improvement in sensitivity of only 3-4, including the improvement attributed to reduced amplifier noise [23].

In modern high-field NMR systems, the frequency of the detected signal can exceed 500 MHz, well above the skin effect regime for even the smallest commercial wire. Using the wire fabrication process we have developed under the A2P program, however, it is now possible to make wires of the requisite diameter and to manipulate them into the proper litz topology. A detailed analysis of the potential improvement that could be achieved with litz wire would require analysis of a specific geometry to properly incorporate proximity effect from the magnetic field generated by the coil. Nevertheless, we can estimate from skin effect alone that at 800 MHz, bulk copper has a skin depth of 2.3 μm. A solenoidal coil wound with 1 mm diameter copper wire would therefore be using less than 1% of the available cross-sectional area of the wire. While it is perhaps theoretically possible for a litz coil to improve Q by a full 100x, it would require significant improvements in manufacturing to enable fabrication of a bundle containing 150,000 strands. Given the ubiquity of NMR and the new applications that would be enabled by such a dramatic increase in sensitivity, however, it seems like an excellent high-value application of the A2P technology.

4.2.2 Miniaturized High-Q Surface-Mount Inductors.

There are many application spaces in which improved air coil inductors could be used. One significant application that suggests other applications is 5G cellular service. 5G service promised greatly improved data rate for video streaming and quick file transfer. Improved data

bandwidth is achieved mostly with change to new carrier frequencies which have more data bandwidth.

Commercial companies currently supply very small multi-turn coils in a pick-and-place SMT (surface-mount technology) applications. The smallest coil which can be purchased is an '0402' (40 mils x 20 mils, or 1mm x 0.5 mm) part (Figure 52). These are air coil inductors expected to be used at up to 2 GHz.

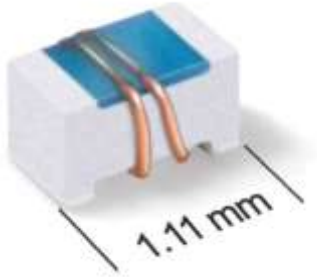

Figure 52. Example coilcraft 0402 SMT RF inductor

Many surface mount components have recently been shrunk. Pick and place machines can now place 0201 (20 x 10 mils) and even 01005 (10 x 5 mils) parts. RF inductors though have not been shrunk to these dimensions. One inductor case, an 0402 11 nH component is reviewed in more detail.

Figure 53 shows a graphic description of how an inductor coil size can be shown. The horizontal line in the graphic indicates an 11 nH value. The red dots indicate the diameter needed for a 6 turn (the litz design case) and a 4 turn inductor (emulating a conventional design). Due to reduced proximity effect and ability to achieve equal R_{AC} with smaller physical conductor, a 6 turn nano-litz part could be made with < 200 μm coil diameter, which fits into an 0201 SMT cross section. This size reduction translates to 1/8 the volume of the 0402 SMT component.

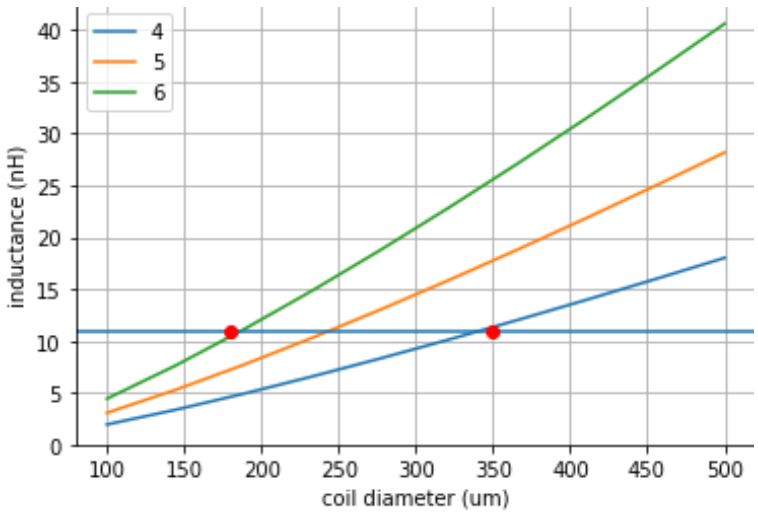

Figure 53. Inductance versus coil diameter for coils with 4, 5, and 6 turns

While reduced component size can be useful in its own right, an additional advantage to smaller components is that they can function as “lumped elements” up to higher frequencies. A 1mm long component is considered ‘lumped element’, i.e. much smaller than a wavelength at the frequency of interest, at 1 GHz. At 10 GHz, however, the ‘0402’ dimension surface mount component is no longer a negligible fraction of a wavelength. An 0201 SMT component, at ½ the length and 1/8 the volume, is still considered a ‘lumped element’ at 10 GHz. In addition, the 0201 component has lower parasitic contributions (pad capacitance and inductance) so that the 0201 component still primarily creates an inductance without significant parasitic contributions.

4.3 Wire Fabrication

Overall, the wire fabrication procedure we developed was very successful at achieving the goals for the program. We were able to reproducibly fabricate wires with diameters far below the limit of commercial wire drawing with high yield and excellent material properties. The majority of our work utilized short wires (~2 cm and shorter), but we successfully demonstrated the ability to manipulate and spool nanofibers up to ~1 meter in length.

4.3.1 Electrospun PMIA Fiber Thermal Stability

The first step in our wire fabrication process was fabrication of the nanofiber scaffold. To characterize the thermal stability of these nanofibers, thick non-woven mats of PMIA nanofibers were deposited and used to characterize the chemical stability of the fibers as a function of temperature via thermal gravimetric analysis (TGA) (Figure 54). As can be seen, the PMIA nanofibers are capable of surviving temperatures up to ~400 °C if $CaCl_2$ from electrospinning is properly removed via washing.

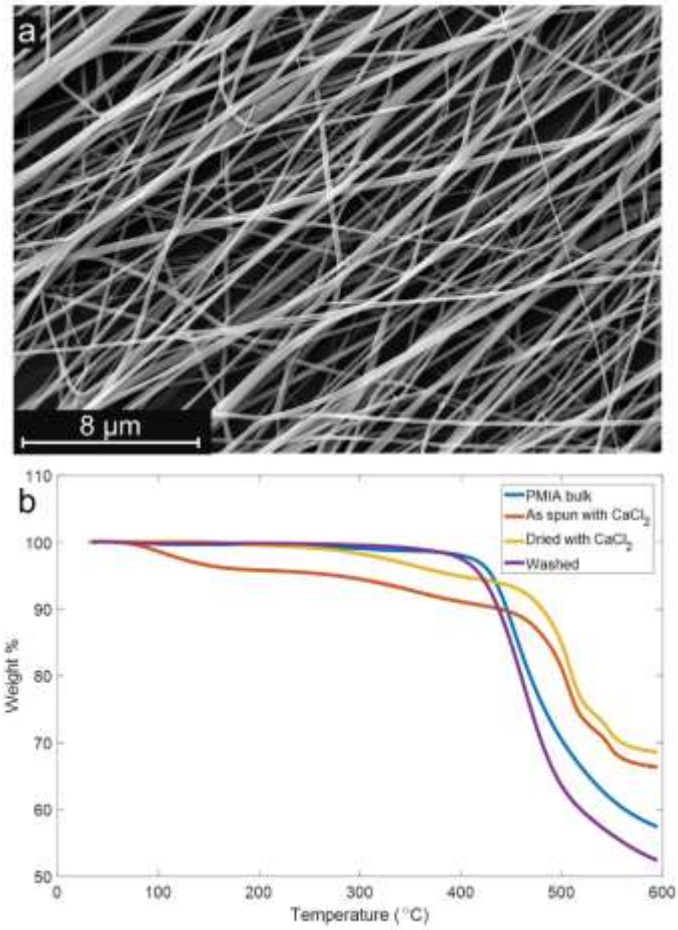

Figure 54. Thermal stability of electrospun PMIA nanofibers. (a) SEM image of a mat of PMIA fibers. (b) TGA results for PMIA bulk starting material, electrospun fibers containing hydrated $CaCl_2$, $CaCl_2$-containing fibers that were dried inside the TGA instrument, and fibers that were washed by immersion in water. (A 12 wt. % PMIA and 8 wt. % $CaCl_2$ in DMAc was used to generate the thick mat used in TGA.)

4.3.2 Electrical Properties of Individual Metal-Coated Nanofibers.

We evaluated the DC electrical conductivity of individual metal coated wires using several methods, all of which yielded results consistent with thin metal wires. In one approach, wires were placed on a Si wafer with a thermal oxide layer using double-sided tape, and Ag paste droplets were added at the two ends to serve as connection pads. A probe station was used to obtain the current vs. voltage values for different wires. Lengths of the wires between the Ag connections were varied between ~1 and 9 mm in these samples. A few of the wires showed a non-Ohmic response likely due to Ag contact irreproducibility and were excluded as outliers. Results were normalized with respect to 5 mm wire length, 400 nm inner fiber diameter, and 500 nm outer wire diameter for better comparison in Figure 55. Silver coated wires show the lowest resistivity within our samples. When high voltages are applied, wires typically break in the 10-20 V range, acting as sub-micron thick fuses.

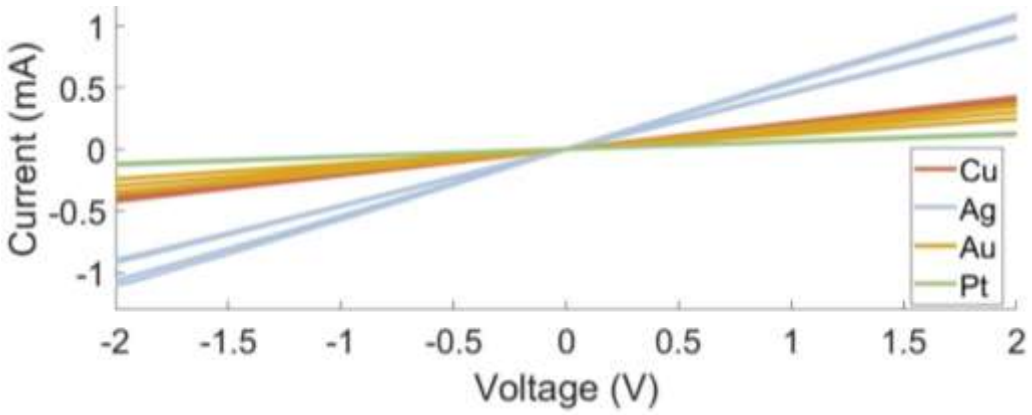

Figure 55. Current versus voltage measurements of PMIA nanofibers coated with various metals

4.3.3 Electroplating and Reel-to-Reel Fabrication.

In section 3.2.4, we introduced a method to electroplate PMIA fibers by using a closed bipolar electrochemical configuration. In our configuration we use a 1 cm plating bath, which limits the throughput. Generally, there are two bounds for scaling up the plating rate. One bound is to consider the voltage drop along the filament given the size of the plating bath (which sets the driving current) and distance from the applied potential (which sets the resistance and voltage drop) is to consider for the manufacturer's recommended current density of 4 ASF, how does the voltage drop due to the seed layer resistance scale with increasing bath size. **Error! Reference source not found.** shows the voltage drop due to resistance given for the recommended current density. In order to avoid unwanted Faradaic reactions, limiting voltage drops to under several hundred millivolts is beneficial. Therefore, plating lengths could scale from 1 to at least 10 cm, per salt water contact. In a mesofluidic chip with many channels this would be easy to integrate to scale to several rows to plate hundreds of centimeters at a time.

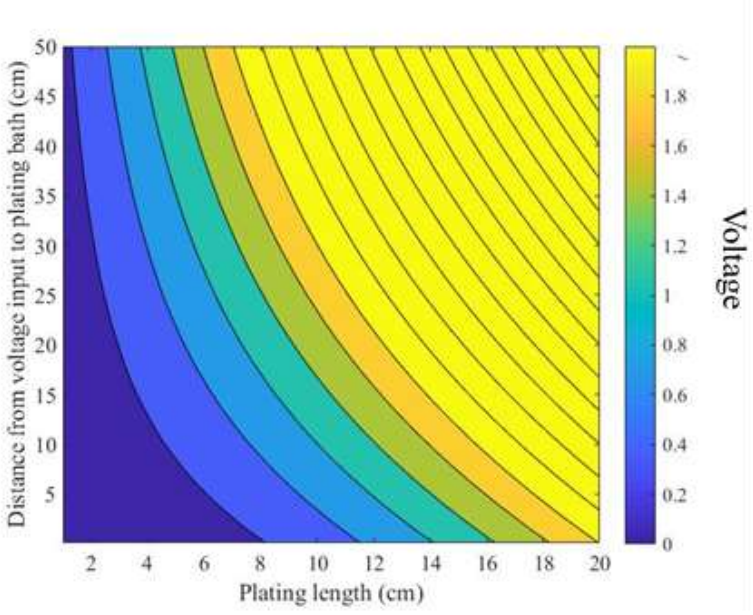

Figure 56. Voltage drop along filament for varying plating length and distance from voltage input, for 4ASF current density .

The more significant rate-limiting step is the manufacturers recommended current density itself. At 4ASF, a 200 nm diameter PMIA filament can plate at a rate of 4 nm. Thus for a 500 nm thick gold film, it will take 125 seconds per segment. In the chip, the linear length of polymer loaded will then dictate the final throughput.

4.4 Directed Assembly of Twisted and Braided Bundles

4.4.1 Hydrodynamic Manipulation.

Using the process described in section 3.3.1 we were able to fabricate twists and twists-of-twists of bare Nomex fiber and Nomex wires coated with a variety of metals and insulating layers. We defined yield as the number of wires in a single twist out of the number of wires that were loaded into the twisting fixture. For additional hierarchical levels of twists we evaluated yield as the number of twisted twists out of the number of loaded twists. As the hydrodynamic manipulation process became developed, refined, and consistent, yield improved to where we could reliably fabricate twists, and twists of twists (see Figure 57). We evaluate the refined process by looking at the subset of twisting runs; here, the final 55, and final 25. Noting that twists, or twists of twists with 4 out of 5 elements (loss of "1") are usable in our Litz bundles, our yield by the end of the project was 80%.

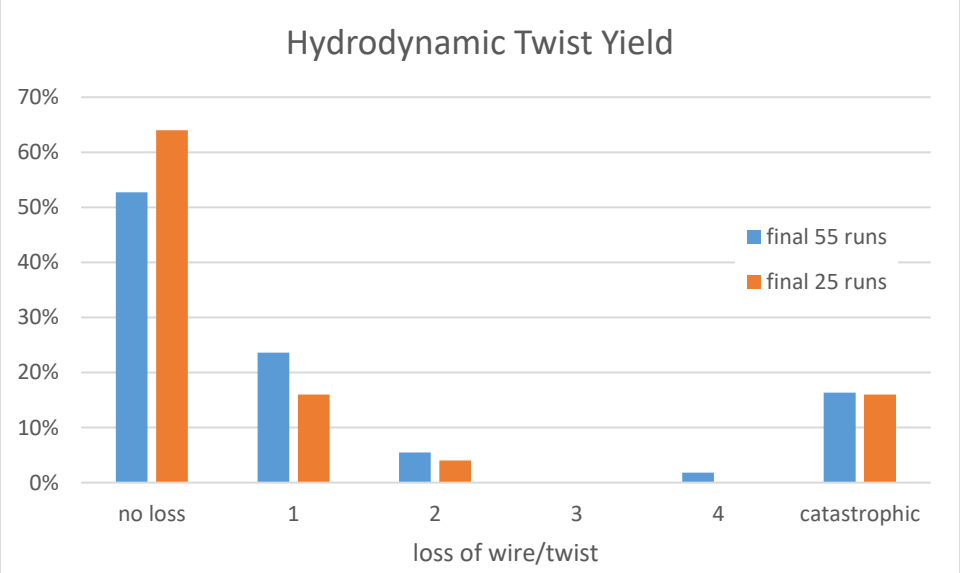

Figure 57. Yield of the refined twisting process. "no loss" denotes no wires or twists lost in the process. "1" denotes a single element (wire or twist) lost. "catastrophic" denotes all elements lost.

Over the course of the project different materials were deposited on the wires to optimize electrical properties. Some examples of twists of twisted bundles of nanowires are shown below (Figure 58 and Figure 59). The different wire types possess unique physical properties that must be accounted for when twisting; we were able to empirically choose twisting parameters (pitch, spin and rise rates) with minimal yield loss. This process should be adaptable to new wire material compositions (core, conductor, insulator, shielding materials) for making twists as this length scale.

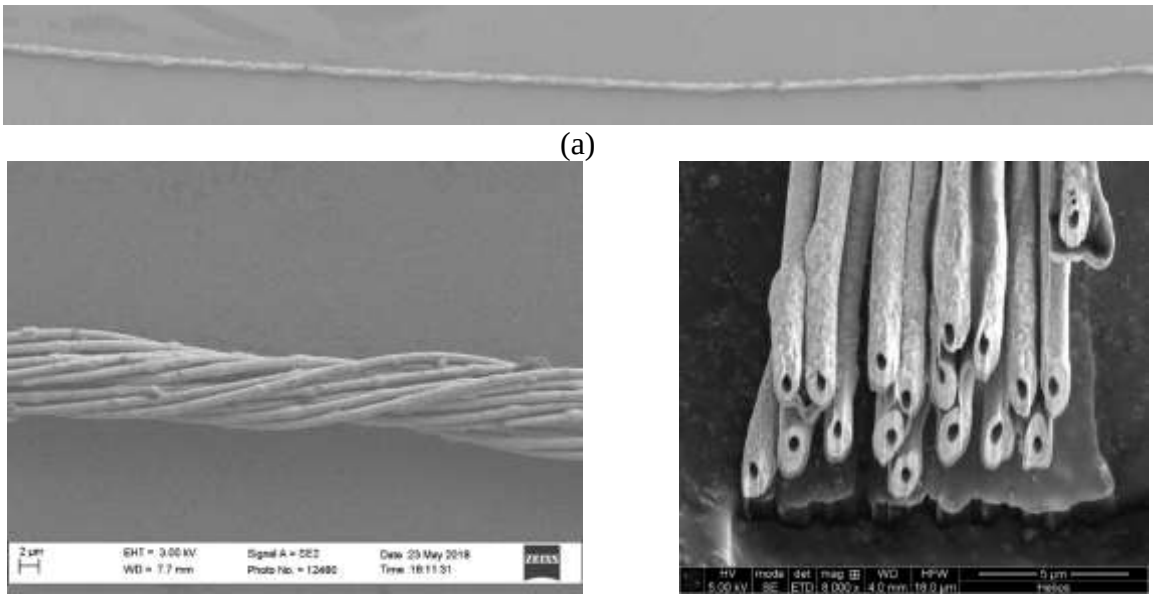

(a) (b) (c)

Figure 58. Bundle of 23 uninsulated nanowires. (a) Scanning electron microscope image, (b) detail, and (c) FIB cross-section.

Figure 59. Optical image of a twist of 5 bundles of 5 ALD insulated nanowires (25 wires total)

4.4.2 Plectoneme Formation and Suppression: Potential for Scale-up of Hydrodynamic Manipulation.

To study fluid-induced helical buckling at a laboratory scale, we cast straight filaments of silicone, a low Young's modulus material, with sub-millimeter diameters and centimeter-length

scales. These high-aspect ratio filaments (length over radius $L/a > 100$), were immersed and rotated in a recirculating tank filled with a high viscosity fluid, glycerin. A schematic of the system is given in Figure 60a, and the details are in Section 3.3.3.

By varying angular velocities and filament aspect ratios, we observed the presence of three different dynamical regimes: *twirling*, where the rod rotated around its center line like a speedometer cable (Figure 60b); *whirling*, where the rod writhed around the rotation axis like a crankshaft, which then evolved to *overwhirling*, where it then formed a steady state whirling ``U" shape (Figure 60c); and finally *plectonemes*, where filaments self-contacted and wrapped around themselves like the twisted kinks in garden hoses (Figure 60d).

For rotating filaments with a fixed geometry (length L and radius a) and Young's modulus E, we typically observed the transition from stable twirling to unstable overwhirling and plectonemes with increasing angular velocity ω (Figure 61). We were able to tune the critical angular velocity, ω_c, by immersing the filament in an axial fluid flow field that generated tension along the length of the filament.

Importantly, our results indicate (green dots on Figure 61) that the approach used for twisting our micron-scale Nomex wires into Nanolitz should scale from the millimeter and centimeter length scales to meters cale without inducing buckling instabilities. Our complete analysis was submitted as a paper to Physical Review Letters and is under review. It is attached as Appendix0.

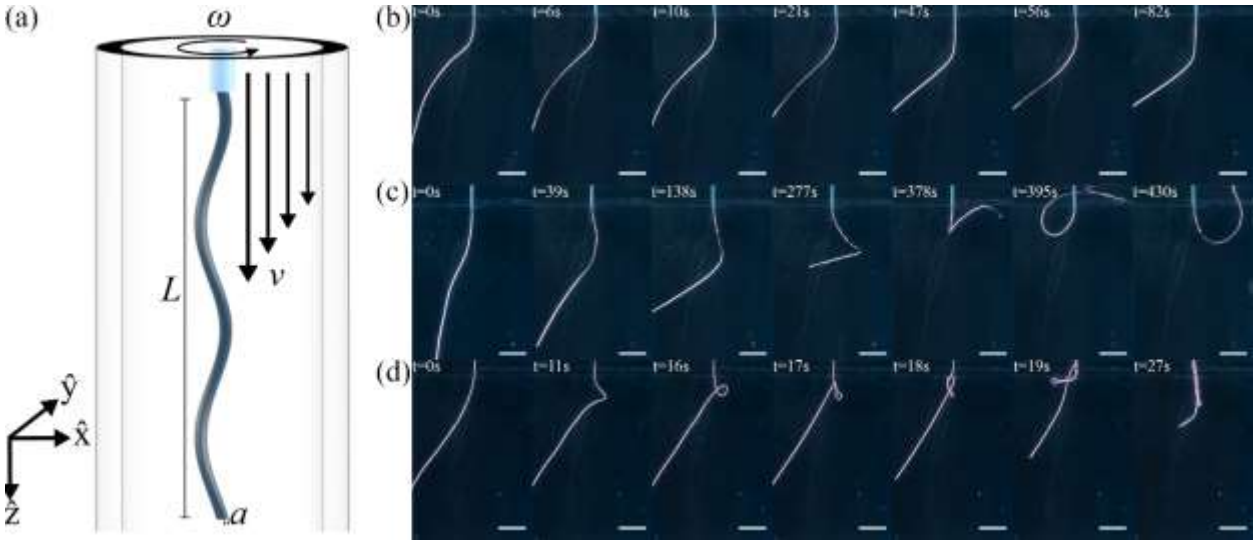

Figure 60: (a) Diagram of the experimental setup. A flexible filament of length l and radius a is freely suspended in a viscous fluid and rotated at the top with an angular velocity ω. A pump provides downward flow with a velocity v to tension the filament. (b)-(d) Times series of 380 μm diameter filaments with v = 0, demonstrating: (b) stable twirling motion with L = 8 cm and ω = 12 rads/s, (c) unstable whirling leading to overwhirling motion with L = 8 cm and ω = 26 rads/s, and (d) plectoneme formation with L = 11 cm and ω = 61 rads/s. Scale bars are all 2 cm.

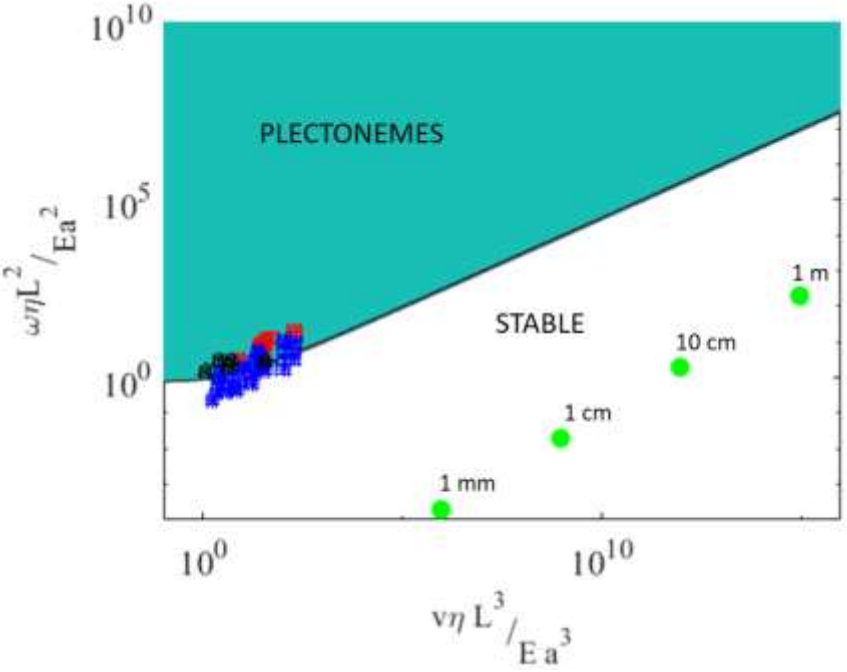

Figure 61. Macro-scale modeling and analytical results show that the approach used for twisting Nomex wires into nanolitz should scale from the milli- and centimeter-length-scales to meter without inducing buckling instabilities.

4.4.3 Elastocapillary Manipulation.

As described in Section 3.3.4, our approach to fully programmable assembly takes advantage of repulsive capillary forces to effectively trap and move small pieces of PDMS ("floats") at the air/water interface inside channels of our devices (Figure 29).

The range of the capillary forces is large (millimeter to centimeter scale), meaning that we can use macroscopic floats and devices to manipulate nanoscale wires. We demonstrate this idea in a simple device to make a hair braid, wherein the braid topology is programmed into the device itself (Figure 62). As the device moves relative to the interface, each centimeter-scale float moves along a set path, moving as far away from the walls of the device as possible. The shape of the walls therefore determines the path, and thus the braid structure. Programming float motions into the device allows us to fabricate complex braids with only one moving part: the stage that raises or lowers the device. As the device moves relative to the interface, each centimeter-scale float moves along a set path, moving as far away from the walls of the device as possible. The shape of the walls therefore determines the path, and thus the braid structure. Programming float motions into the device allows us to fabricate complex braids with only one moving part: the stage that raises or lowers the device.

In the language of braid theory, the structure of the device defines a sequence of braid generators, σ_i. Each σ_i represents a strand in the i^{th} place crossing over the strand in the i+1th place, while the operation σ_i^{-1} represents a strand in the i^{th} place crossing *under* the strand in the i+1th place. Thus, $\sigma_1\ \sigma_2^{-1}$ is the repeating sequence that describes the hair braid: the strand in the leftmost position must cross over the middle strand, and then the middle strand must cross under

the rightmost strand. This process can be repeated many times. However, while this is simple to do with our hands at a macroscale, the 3-strand hair braid has not been achieved at the micro- or nanoscale.

To do that, we must also perform two other operations, besides switching, that are essential to making real braids: separating two floats (and their attached wires) and ratcheting floats back to their original positions without undoing the braid. These operations are shown in Figure 62a-c. As with switching, they are controlled through the shape of the walls of the device.

We demonstrate these operations by making a three-strand braid of the type usually used for hair, but with smaller (5 μm diameter) fibers (Figure 62d-e). The motions of the floats can be seen in Movie S1. The braid seen in the micrograph has multiple repeating elementary units. We make these simply by cycling the motion of the device. As we move the device up with respect to the interface, the braid pattern is formed. As we move it down, the floats return to their starting positions through a different path, one that does not undo the braid (Figure 62d). Because the paths of the floats through the device is deterministic in both directions, we can extend the braid pattern by continuously moving the device up and down. In practice, we have made hair braids with 10 repeating units, and we believe we can make many more after we solve some minor technical challenges. The motions of the floats can be seen in Movie S1. The braid seen in the micrograph has multiple repeating elementary units. We make these simply by cycling the motion of the device. As we move the device up with respect to the interface, the braid pattern is formed. As we move it down, the floats return to their starting positions through a different path, one that does not undo the braid (d). Because the paths of the floats through the device is deterministic in both directions, we can extend the braid pattern by continuously moving the device up and down. In practice, we have made hair braids with 10 repeating units, and we believe we can make many more after we solve some minor technical challenges.

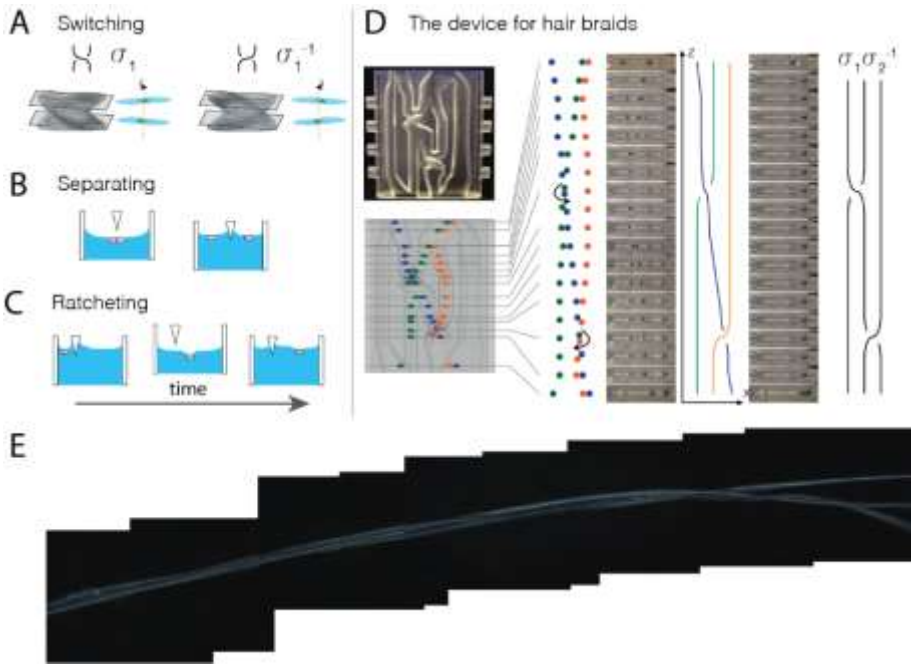

Figure 62. A 3-strand braid is achieved by integrating three operations into one device. (A) The switch, in which two floats change positions, leading to wires crossing each other. Each cross-section of a switching section is an oval whose long axis rotates 180° along the z-axis.

As the interface moves through each cross-section, a pair of floats aligns with the long axis of the oval, owing to repulsive capillary forces. As the interface moves through the switch, the floats turn 180°. The handedness of the switch is programmed into the device design. (B) A separator, which separates two floats. When the meniscus reaches the divide (the triangle), strong repulsive capillary forces overcome the capillary attraction between the two floats and separate them. (C) The ratchet, which steers a float into a different channel when the device movement is reversed. A float tends to stay at the center of the meniscus due to repulsive capillary forces. Thus, when the device is moved up, the float in the narrow channel on the left moves to the center of the large channel. When the device is moved back down, the float moves into the wider channel on the right. (D) A photograph of a 3-strand braiding device along with schematics and photographs of cross-sections. As shown from top to bottom, when the device is moved out of water, the green and orange floats are separated, the blue and green floats are switched (σ_1) and separated, and then the blue and orange floats are switched (σ_2^{-1}) in the opposite direction and separated. The lateral positions of each float are tracked and plotted with respect to height, which shows the 3-strand braid pattern. When floats reach the bottom of the device, the ratchet steers them to the outside channels (second column of photographs), such that the braid operation can be repeated (E) Optical micrograph of a 3-strand braid assembled with Kevlar fibers that are about 5 μm in diameter.

An issue with this simple approach to making braids, where each switch is constructed into the device itself, is that the height of the device scales with the number of strand switches in each repeating unit of the braid. This problem becomes more acute for braids with long repeating units. In particular, for twists or hierarchical twists (twists of twisted wires), the repeating units can be very long, as shown by the braid theory notation in Figure 3e, which describes the pattern of switches required to make a braid in which three groups of three twisted strands are twisted around each other. This kind of pattern is useful for the Litz wires discussed above.

Therefore we develop another type of device that can switch multiple strands simultaneously. A device to make a simple twist is shown in Figure 63a. Multiple wires are attached to the float, which then spins as the device moves up with respect to the interface. To make multiple repeating units of the twist, we must be able to move the device back down (with respect to the interface) without undoing the twist. To do this, we use a different kind of ratchet, shown in Figure 63b. Multiple wires are attached to the float, which then spins as the device moves up with respect to the interface. To make multiple repeating units of the twist, we must be able to move the device back down (with respect to the interface) without undoing the twist. To do this, we use a different kind of ratchet, shown in b.

This ratchet is based on contact-line hysteresis. At a given height, the shape of the meniscus is different, depending on whether the device is moving up or down, owing to the difference between the advancing and receding contact angles (Figure 63c). Theoretical calculations from the Brenner group (Figure 63d) show how to exploit this (usually small) difference in contact angle. If the device has a rectangular float and a radial slot, the float can rotate as the device moves in one direction, but when it moves in the other, the long axis of the float oscillates about the direction of the slot. Figure 31c). Theoretical calculations from the Brenner group (d) show how to exploit this (usually small) difference in contact angle. If the device has a rectangular float and a radial slot, the float can rotate as the device moves in one direction, but when it moves in the other, the long axis of the float oscillates about the direction of the slot.

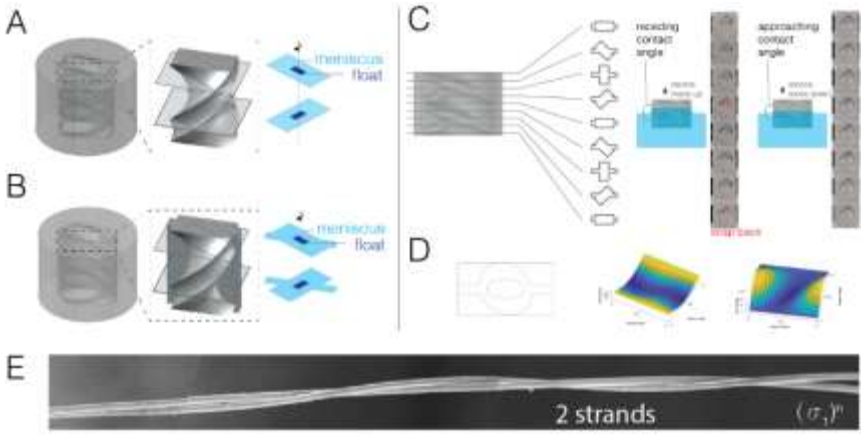

Figure 63. Multiple wires can be twisted by attaching them to the same float. (A) Similar to Figure 62A, a float can be turned through a channel with a rectangular cross-section that is rotated along its normal axis. (B) To rachet, we add a slot that runs through the entire height of the device. (C) Diagram of device and shapes of cross-sections along the height. When the device moves up, there are sudden "snap back" events (red arrows) that prevent the float from making a full rotation. When the device moves down, the float smoothly makes a full rotation. The difference between the two directions arises from the difference in advancing and receding contact angles. (D) A numerical model of the interface shows the energy as a function of the float orientation and height inside the device at two different contact angles. When the contact angle is small (left), the minimum-energy orientation oscillates about the orientation of the slot, as seen in the experiment. When the contact angle is large (right), the minimum-energy orientation aligns with the rotation of the channel. (E) Electron micrograph shows two 5-μm-diameter Kevlar fibers that have been twisted around each other using the device in panel C. Figure 30A, a float can be turned through a channel with a rectangular cross-section that is rotated along its normal axis. (B) To rachet, we add a slot that runs through the entire height of the device. (C) Diagram of device and shapes of cross-sections along the height. When the device moves up, there are sudden "snap back" events (red arrows) that prevent the float from making a full rotation. When the device moves down, the float smoothly makes a full rotation. The difference between the two directions arises from the difference in advancing and receding contact angles. (D) A numerical model of the interface shows the energy as a function of the float orientation and height inside the device at two different contact angles. When the contact angle is small (left), the minimum-energy orientation oscillates about the orientation of the slot, as seen in the experiment. When the contact angle is large (right), the minimum-energy orientation aligns with the rotation of the channel. (E) Electron micrograph shows two 5-μm-diameter Kevlar fibers that have been twisted around each other using the device in panel C.

We can combine this twisting operation with switching to make hierarchical twists using a compact device. By connecting multiple wires to each float, one can make hierarchical twists. For example, a 2x2 twist can be made by attaching two wires to each float.

Having shown that we can switch, twist, separate, and ratchet wires, we now demonstrate that we can make arbitrary braids. By "arbitrary" we mean any braid pattern within the mathematical braid group B_n, where n is the number of strands in the braid. Formally, switching neighboring

strands corresponds to multiplying a braid by a generator σ. Mathematicians have shown that the braid group is closed under multiplication, meaning that if all generators are available, then all possible *n*-strand braids can be constructed simply by combining the generators. Therefore a device in which any two neighboring strands can be switched in any order can make an arbitrary braid. This includes all of the braids we have shown so far, including twists, hierarchical twists, and non-twisting braids, and even braids without repeating units.

We show such a device in Figure 64a. This device consists of vertical sections corresponding to all possible 4-strand generators: σ_1, σ_1^{-1}, σ_2, σ_2^{-1}, σ_3, σ_3^{-1}. The challenge is to "call" or access the generators in arbitrary order. To do this, we use a variant of the ratchet design in Figure 62. Again, this design relies on repulsive capillary forces. We create "operational zones" at different heights in the device, such that when the interface is positioned within a zone and its direction reversed, it follows a particular switch. There is one operational zone per generator. Therefore each generator can be called in arbitrary order. We have not yet built this device or used it to make braids, but we have demonstrated all the operations needed including the "operational zone." This device consists of vertical sections corresponding to all possible 4-strand generators: σ_1, σ_1^{-1}, σ_2, σ_2^{-1}, σ_3, σ_3^{-1}. The challenge is to "call" or access the generators in arbitrary order. To do this, we use a variant of the ratchet design in . Again, this design relies on repulsive capillary forces. We create "operational zones" at different heights in the device, such that when the interface is positioned within a zone and its direction reversed, it follows a particular switch. There is one operational zone per generator. Therefore each generator can be called in arbitrary order. We have not yet built this device or used it to make braids, but we have demonstrated all the operations needed including the "operational zone."

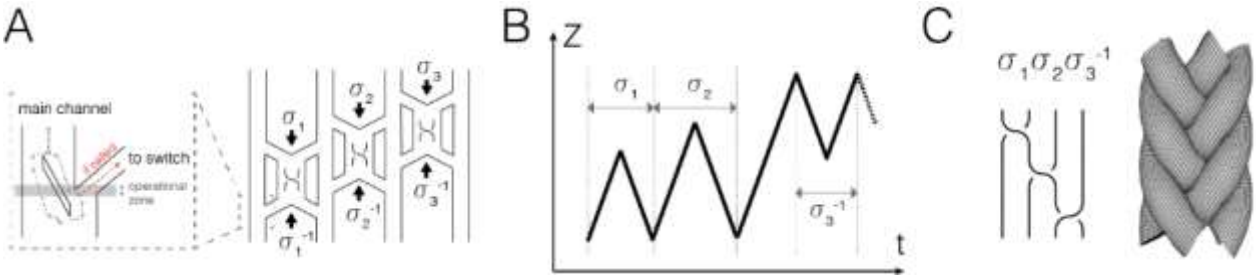

Figure 64. An arbitrary braiding machine design that can braid any four-strand topology. (A) The device has four main channels, each of which controls one float. A switch between two neighboring floats can be "called" by moving the device to the right height in the right direction. For instance, in the inset, the float travels down the main channel when the device is moved out of water. When the float reaches the operational zone, it stays in the main channel (along the gray arrows) unless the direction of the device movement is reversed there. Reversing the direction moves the float into a switch (red arrow). Since the same switch can be accessed from above and below, both handedness (σ_i and σ_i^{-1}) can be achieved in the same section of the device. (B) As an example, a braid $\sigma_1\sigma_2\sigma_3^{-1}$ can be made by moving the device along the trajectory z(t) shown here. This trajectory is easily programmed into the motorized stage. (C) The braid $\sigma_1\sigma_2\sigma_3^{-1}$ in panel B corresponds to a fishtail braid, shown schematically and rendered here.

What enables this approach is the ability to move the stage in an arbitrary direction as a function of time. A major difference between this approach and those shown in Figure 62 and Figure 63 is

that the motion of the device up and down controls the braid pattern, whereas in the other devices, the braid topologies are programmed into the devices themselves. But in both cases, only a single degree of freedom is required: one needs only a motorized stage that can move along one axis. Thus, compared to mechanical braiding machines, which steer every single strand in two axes in a fixed pattern, our device is much simpler and requires far fewer moving parts. Motion of the device up and down controls the braid pattern, whereas in the other devices, the braid topologies are programmed into the devices themselves. But in both cases, only a single degree of freedom is required: one needs only a motorized stage that can move along one axis. Thus, compared to mechanical braiding machines, which steer every single strand in two axes in a fixed pattern, our device is much simpler and requires far fewer moving parts.

The simplicity and small number of moving parts are advantageous for applications. The devices themselves (excluding the motorized stage) are 3D-printed, costing only a few dollars per devices. The programmable motorized stage requires only a $30 stepper motor and controller. Because the stage requires only a single degree of freedom, one can easily make many braids in parallel simply by placing multiple devices on the same stage. Furthermore, because a single device can be programmed to make any braid, our approach allows for rapid prototyping of different braid structures for different applications.

Because the capillary forces are weak, the method is scalable to small wire diameters. Capillary forces scale with the perimeter of the object and are known to be able to assemble structure from the nanoscale to the millimeter scale [8]–[12]. We can precisely control the capillary forces by controlling the size, shape and wettability of our float. Therefore, our method is universal and independent of the wire material.

Limitations: although we do not need to continuously feed the wires to the device, we do have to connect the wires to the floats. Currently we do this manually, which is the largest source of failures. Also we have not yet demonstrated braids of submicrometer-scale fibers.

5 CONCLUSIONS

As part of the A2P Nano-Litz program, we successfully developed several new techniques and technologies. A key achievement was the first demonstration of litz wire operating in the GHz regime. This technology has the potential to drastically improve the sensitivity of NMR, enabling more rapid pharmaceutical drug discovery and more precise determination of molecular structure of large molecules. In addition, it may enable further miniaturization of inductive components for 5G and other high-frequency communication. The ability to make and manipulate wires far below the limit of conventional wire drawing may prove useful in its own right for the economical manufacture of ultra-fine wire, even at wire diameters that are available via conventional wire drawing. Finally, several interesting technologies, including the ability to passively braid and twist wires via elastocapillary interaction, have opened new possibilities into the manipulation of small structures, perhaps enabling yet further opportunities to translate atoms into products.

6 RECOMMENDATIONS

The goals for this program were the demonstration of the ability to make litz wire that was optimized for the GHz regime as well as the demonstration of a litz wire performance benefit at GHz frequencies. Having achieved both goals, it is clear both that this technology can enable 10x improvements to a variety of exciting applications and that the key limitations to adoption of nano-litz wire will be manufacturability and cost. While we have taken significant strides toward developing processing technology that could enable cost-effective manufacturing of nano-litz wire, significant work remains to fully realize this potential. We therefore recommend that additional work be funded to further develop the needed manufacturing capability to enable the full capability of this technology to be realized.

REFERENCES

[1] A. Payne, “LITZ CABLE FOR HF SINGLE LAYER COILS,” p. 32, 2014.

[2] E. L. Hall, “Resistance of conductors of various types and sizes as windings of single-layer coils at 150 to 6,000 kilocycles.,” National Bureau of Standards, Technologic Papers of the Bureau of Standards T 330, 1926.

[3] F. Terman, *Radio Engineers Handbook*. McGraw-Hill Book Company, Inc., 1943.

[4] Xu Tang and C. R. Sullivan, “Optimization of stranded-wire windings and comparison with litz wire on the basis of cost and loss,” in *2004 IEEE 35th Annual Power Electronics Specialists Conference (IEEE Cat. No.04CH37551)*, Aachen, Germany, 2004, pp. 854–860.

[5] A. Aydin, L. Sun, X. Gong, K. J. Russell, D. J. D. Carter, and R. G. Gordon, “Strong, Long, Electrically Conductive and Insulated Coaxial Nanocables,” *ACS Appl. Polym. Mater.*, vol. 1, no. 7, pp. 1717–1723, Jul. 2019.

[6] B. S. Lim, A. Rahtu, J.-S. Park, and R. G. Gordon, “Synthesis and Characterization of Volatile, Thermally Stable, Reactive Transition Metal Amidinates,” *Inorg. Chem.*, vol. 42, no. 24, pp. 7951–7958, Dec. 2003.

[7] B. Pokroy, S. H. Kang, L. Mahadevan, and J. Aizenberg, “Self-Organization of a Mesoscale Bristle into Ordered, Hierarchical Helical Assemblies,” *Science*, vol. 323, no. 5911, pp. 237–240, Jan. 2009.

[8] N. Bowden, A. Terfort, J. Carbeck, and G. M. Whitesides, “Self-Assembly of Mesoscale Objects into Ordered Two-Dimensional Arrays,” *Science*, vol. 276, no. 5310, pp. 233–235, 1997.

[9] A. Terfort, N. Bowden, and G. M. Whitesides, “Three-dimensional self-assembly of millimetre-scale componets,” *Nature*, vol. 386, pp. 162–164, 1997.

[10] J. Tien, T. L. Breen, and G. M. Whitesides, “Crystallization of Millimeter-Scale Objects with Use of Capillary Forces,” *J. Am. Chem. Soc.*, vol. 120, no. 48, pp. 12670–12671, Dec. 1998.

[11] T. L. Breen, J. Tien, S. R. J. Oliver, T. Hadzic, and G. M. Whitesides, “Design and Self-Assembly of Open, Regular, 3D Mesostructures,” *Science*, vol. 284, no. 5416, pp. 948–951, May 1999.

[12] C. Py, P. Reverdy, L. Doppler, J. Bico, B. Roman, and C. N. Baroud, “Capillary Origami: Spontaneous Wrapping of a Droplet with an Elastic Sheet,” *Phys. Rev. Lett.*, vol. 98, no. 15, Apr. 2007.

[13] M. Mastrangeli, W. Ruythooren, J. Celis, and C. V. Hoof, “Challenges for Capillary Self-Assembly of Microsystems,” *IEEE Trans. Compon. Packag. Manuf. Technol.*, vol. 1, no. 1, pp. 133–149, Jan. 2011.

[14] D. Vella and L. Mahadevan, “The ‘Cheerios effect,’” *Am. J. Phys.*, vol. 73, no. 9, pp. 817–825, Sep. 2005.

[15] D. Kajfez, “Q-Factor,” *Encycl. RF Microw. Eng.*, 2005.

[16] P. J. Petersan and S. M. Anlage, “Measurement of resonant frequency and quality factor of microwave resonators: Comparison of methods,” *J. Appl. Phys.*, vol. 84, no. 6, pp. 3392–3402, 1998.

[17] K. Leong and J. Mazierska, “Precise measurements of the Q factor of dielectric resonators in the transmission mode-accounting for noise, crosstalk, delay of uncalibrated lines, coupling loss, and coupling reactance,” *IEEE Trans. Microw. Theory Tech.*, vol. 50, no. 9, pp. 2115–2127, Sep. 2002.
[18] C. R. Sullivan and R. Y. Zhang, “Analytical model for effects of twisting on litz-wire losses,” in *2014 IEEE 15th Workshop on Control and Modeling for Power Electronics (COMPEL)*, Santander, Spain, 2014, pp. 1–10.
[19] C. R. Sullivan, “Optimal choice for number of strands in a litz-wire transformer winding,” *IEEE Trans. Power Electron.*, vol. 14, no. 2, pp. 283–291, Mar. 1999.
[20] “Appendix A: Formulae for Partial Inductance Calculation,” in *Signal Integrity and Radiated Emission of High-Speed Digital Systems*, Chichester, UK: John Wiley & Sons, Ltd, 2008, pp. 481–486.
[21] J.-H. Ardenkjaer-Larsen *et al.*, “Facing and Overcoming Sensitivity Challenges in Biomolecular NMR Spectroscopy,” *Angew. Chem. Int. Ed Engl.*, vol. 54, no. 32, pp. 9162–9185, Aug. 2015.
[22] D. I. Hoult and R. E. Richards, “The signal-to-noise ratio of the nuclear magnetic resonance experiment,” *J. Magn. Reson. 1969*, vol. 24, no. 1, pp. 71–85, Oct. 1976.
[23] H. Kovacs, D. Moskau, and M. Spraul, “Cryogenically cooled probes—a leap in NMR technology,” *Prog. Nucl. Magn. Reson. Spectrosc.*, vol. 46, no. 2–3, pp. 131–155, May 2005.

APPENDIX: MACROSCALE TWISTING PAPER

Twirling, Whirling, and Tensioning: Plectoneme Formation and Suppression in Flexible Filaments

Isaac R. Bruss,[1,*] Heena K. Mutha,[2,*] Katherine Stoll,[2] Brent Collins,[2] Vinh Nguyen,[2] David Carter,[2] Michael P. Brenner,[1,3] and Kasey J. Russell[2,†]

[1] *School of Engineering and Applied Sciences, Harvard University, Cambridge, MA 02138*
[2] *The Charles Stark Draper Laboratory, Inc., Cambridge, MA 02139*
[3] *Kavli Institute of Bionano Sciences and Technology, Harvard University, Cambridge, MA 02138*

(Dated: July 8, 2019)

A high-aspect ratio flexible filament suspended in a viscous fluid is unstable to a symmetry-breaking whirling motion when axially rotated beyond a critical velocity. We present the first known experiments of this behavior and uncover a rich diversity of plectoneme formation soon after the initial instability, including multiple plectonemes for especially long filaments. A physical model extending Timoshenko's theory of elastic instability is presented which captures the fundamental physics involved in the instability. Additionally, we consider the effects of an axial flow that acts to tension the filament and control the onset of whirling without adjusting the physical properties of the filament itself. Such a setup could be employed to selectively engineer plectoneme formation at specified locations and lengths, and in fibers with sub-micron diameters, potentially to create super-elastic ropes and fabrics.

A sufficiently flexible object immersed in a moving fluid will dynamically change shape—and therefore alter the encompassing flow field—despite the standard assumption that low Reynolds number fluids are characterized as having a smooth and steady flow field [1]. A common example is the motion of microscopic cilia and flagella, which are able to transform their rotational and/or cyclic motion into translational motion of the entire cell [2].

A prevalent class of shape change, especially for large-aspect ratio elastic materials—like the two biological examples above—is the buckling instability, which comes in two varieties: compressional Euler buckling, and helical buckling [3, 4]. The dynamic and versatile behavior of Euler and helical buckling has been cleverly exploited by a variety of biological phenomena such as filopodia to produce motion [5], uni-flagellated bacteria to achieve reorientation [6], and plant roots to redirect growth around barriers [7]. However, in general, torsion-induced helical buckling has historically been classified as a mode of "failure", for instance in industrial applications such as breaking tubes during well drilling [8, 9]. Similarly, high-aspect ratio wires formed from electrospun nanofibers of sub-micron diameter and centimeter-scale lengths coated with metal [10] can undergo torsion-induced failure when being twisted to synthesize micron-scale litz wire [11].

Both Euler and helical buckling modes can be produced via fluid flow. For example, Euler buckling has been observed experimentally by extruding a filament [12] or by rotating helical filaments [13] in a highly viscous fluid. In this letter, we present the first known experiments demonstrating fluid-induced helical buckling in straight filaments.

To study fluid-induced helical buckling at a laboratory scale, we cast straight filaments of silicone, a low Young's modulus material, with sub-millimeter diameters and centimeter-length scales. These high-aspect ratio filaments (length over radius $L/a > 100$), were immersed and rotated in a recirculating tank filled with a high viscosity fluid, glycerin. A schematic of the system is given in Fig 1a, and the details are in the Supporting Information (S.I.). By varying angular velocities and filament aspect ratios, we observed the presence of three different dynamical regimes: *twirling*, where the rod rotated around its center line like a speedometer cable (Fig. 1b); *whirling*, where the rod writhed around the rotation axis like a crankshaft, which then evolved to *overwhirling*, where it then formed a steady state whirling "U" shape (Fig. 1c); and finally *plectonemes*, where filaments self-contacted and wrapped around themselves like the twisted kinks in garden hoses (Fig. 1d). For rotating filaments with a fixed geometry (length L and radius a) and Young's modulus E, we typically observed the transition from stable twirling to unstable overwhirling and plectonemes with increasing angular velocity ω (Fig. 2). We were able to tune the critical angular velocity, ω_c, by immersing the filament in an axial fluid flow field that generated tension along the length of the filament.

Several insightful models have investigated the underlying physics and conjectured resulting modes of filaments under fluid-induced helical buckling. Most notably Wolgemuth *et al.*[14] introduced the twirling and whirling modes in rotating filaments using numerical and analytical methods. Building upon this work, there have been multiple attempts to simulate the twirling to whirling instability [15], including a hydrodynamic bead-spring model [16, 17], immersed-boundary fluid dynamics [18], and a combination Kirchhoff rod/regularized Stokeslets model [19]. These works all predicted the existence of the additional stable state, overwhirling. Finally, plectonemes, the far-from instability structures commonly found in DNA [20, 21], are the anticipated final form of helically buckled rods that are torqued well beyond

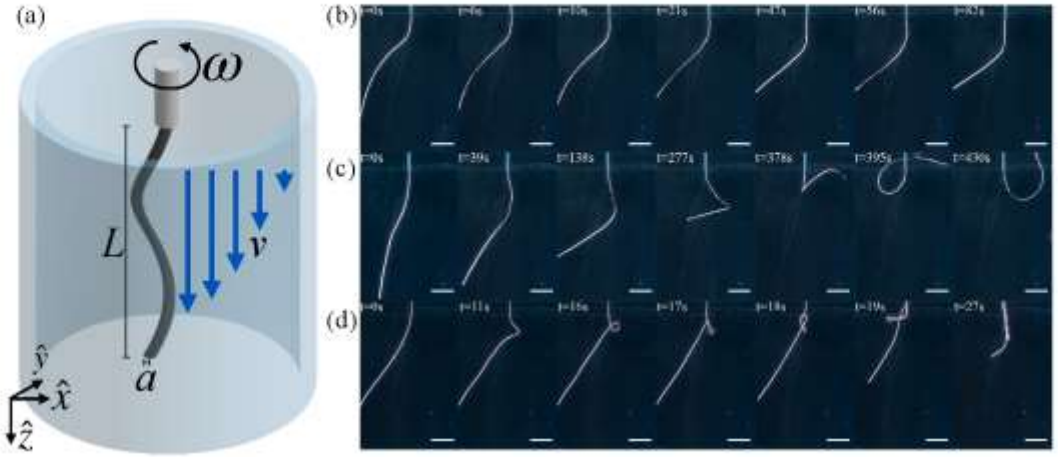

FIG. 1. (a) Diagram of the experimental setup. A flexible filament of length l and radius a is freely suspended in a viscous fluid and rotated at the top with an angular velocity ω. A pump provides downward flow with a velocity v to tension the filament. (b)-(d) Times series of 380 μm diameter filaments with $v = 0$, demonstrating: (b) stable twirling motion with $L = 8$ cm and $\omega = 12$ rads/s, (c) unstable whirling leading to overwhirling motion with $L = 8$ cm and $\omega = 26$ rads/s, and (d) plectoneme formation with $L = 11$ cm and $\omega = 61$ rads/s. Scale bars are all 2 cm.

the initial buckling event [4, 22, 23]. Our experiments confirmed the existence of these predicted whirling, overwhirling, and plectoneme modes, and provide insight into the range of possible unstable modes. In addition, our experiments added tension to the filament with axial fluid flow. Here, using a simplified Kirchhoff rod and slender-body fluid dynamics model, we extend existing modeling efforts to explain the critical angular velocity for buckling, ω_c, as well as its dependence on the filament's aspect ratio, material properties, and fluid parameters.

We begin with a scaling analysis to establish the essential physical phenomena. We can estimate ω_c by building upon the classic theory of elastic instability for a flexible rod with hinged boundary conditions. Based on the standard Kirchhoff equations, a rod (see Fig. 1) of length L and radius a is in equilibrium when

$$EI\frac{d^2x}{dz^2} = Tx + C\tau\frac{dy}{dz}$$
$$EI\frac{d^2y}{dz^2} = Ty - C\tau\frac{dx}{dz}, \qquad (1)$$

where E is the Young's modulus, $I = \frac{\pi}{4}a^4$ is the second moment of area, T is the axial tension, $C = EI/(1+\nu)$ is the twist modulus, ν is Poisson's ratio, and τ is the Frenet-Serret torsion of the curve [4]. Following the theory laid out by Timoshenko [3], we can derive the magnitude of the critical torsion of the curve for helical buckling of a a freely suspended, uniformly twisted rod:

$$\tau_c(L,T) = \frac{3\sqrt{TL^2 + EI\pi^2}}{L\sqrt{EI}} = \sqrt{\frac{36T}{\pi a^4 E} + \frac{9\pi^2}{L^2}}, \qquad (2)$$

where we have henceforth assumed an incompressible material with a Poisson's ratio of $\nu = 0.5$, such as the effectively incompressible silicone rubber used in our experiments. In the limit of zero tension, Eq. (2) yields $\tau_c(L,0) = 3\pi/L$, anticipating that for our finite length system there is always a critical non-zero torsion of the curve required to achieve buckling. Furthermore, we will show that Eq. (2), despite being derived for the case of a uniformly twisted rod, can serve as the foundation for an approximate solution to a more general system with non-uniform torsion.

Specifically, in our system torsion is generated by rotating the rod at the top end ($s = 0$) through a fluid with a viscosity η. Assuming zero Reynolds number, slender-body dynamics gives the drag coefficient for an axially rotating rod at equilibrium to be $\zeta_r = 4\pi\eta a^2$ [24]. Because the bottom end ($s = L$) of the rod is free, at equilibrium the magnitude of the internal torsion of the curve resulting from this rotational drag decreases linearly with s:

$$\tau(s) = \frac{\zeta_r\omega}{C}(L-s) = 24\frac{\omega\eta}{Ea^2}(L-s). \qquad (3)$$

Now we can ask: given a partial section of the rod between $s = 0$ and some arc length $s = s^*$, and assuming it obeys Eq. (1), is the torsion strong enough to induce helical buckling? To utilize Eq. (2), we approximate the s-dependent torsion of the curve as being uniform within this s^* segment with a value equal to the average along

the length of the segment:

$$\tau_{av}(s^*)L = 12\frac{\omega\eta}{E}\left(\frac{L}{a}\right)^2(2-\frac{s^*}{L}). \quad (4)$$

This average unitless torsion of the curve (i.e. radians of rotation along the total length) is maximum for short segments near the driven end (i.e. for small s^*), and it is quadratically dependent on the aspect ratio, L/a. Continuing our dissection of the rod into s^* segments and employing Eq. (2), a rod with zero tension will buckle when $\tau_{av}(s^*) \geq \tau_c(s^*, 0)$, finally yielding

$$\lim_{T\to 0}\omega_c = \frac{\pi}{4}\frac{E}{\eta}\left(\frac{a}{L}\right)^2 \quad (5)$$

when $s^* = L$. Though our model makes some ambitious assumptions, our numerical prefactor of $\pi/4 \approx 0.785$ is comparable to the result of 0.563 from the standard model by Wolgemuth *et al.*, which is based on numerical solutions of the linearized slender body dynamics model [14, 15].

Next we expand our model by modifying the tension component of Eq. (2) to include an axial fluid flow at a velocity v. The axial drag coefficient for a rod is $\zeta_{||} = 2\pi\eta/[\ln(L/2a) + c]$, where the logorithmic denominator stems from Stokes' paradox, and accounts for the finite length of the rod [25]. The constant, c, stems from additional terms in asymptotic expansion [24]. The axial tension on the rod is therefore $T = \zeta_{||}v(L-s)$, and following the same steps that led to Eq. (4), we arrive at

$$T_{av}(s^*) = \frac{\pi\eta L v}{\ln(L/2a) - 0.84}\left(2-\frac{s^*}{L}\right). \quad (6)$$

Inserting this average tension back into eqns (2) & (4), we arrive at the final governing inequality

$$12\frac{\omega\eta}{E}\frac{L^2}{a^2}(2-\frac{s^*}{L}) \geq 3\sqrt{\pi^2\frac{L^2}{s^{*2}} + 4\alpha\frac{v\eta}{Ea}\frac{L^3}{a^3}\frac{2-s^*/L}{\ln(\frac{L}{2a})+C}}, \quad (7)$$

where the left side represents the average torsion of the curve of a segment s^* of a filament of total length L, and the right side represents the critical torsion of the curve required for the segment to helically buckle. We set $C = -0.84$, which is derived from the $O(\log(L/a))$ term, and which is within $< 1\%$ of the extrema values for our experimental range of $L/a = (200, 600)$ [24]. The sole fitting parameter, α, accounts largely for our model's assumption that the axial fluid flow only exerts axial tension on the filament, whereas in reality it also applies an effective torque on the filament to reorient any perturbations back to the $\hat{z}$ axis orientation.

From Eq. (7) there are two unitless parameters that regulate this instability. First is the relative rotational velocity's contribution to torque, $(\omega\eta/E)(L/a)^2$; and second is the relative fluid velocity's contribution to tension, $(v\eta/Ea)(L/a)^3$. Numerically solving for the critical rotational velocity, ω_c, in Eq. (7) yields the lines in Fig. 2, which capture the observed physical behavior across a wide parameter range.

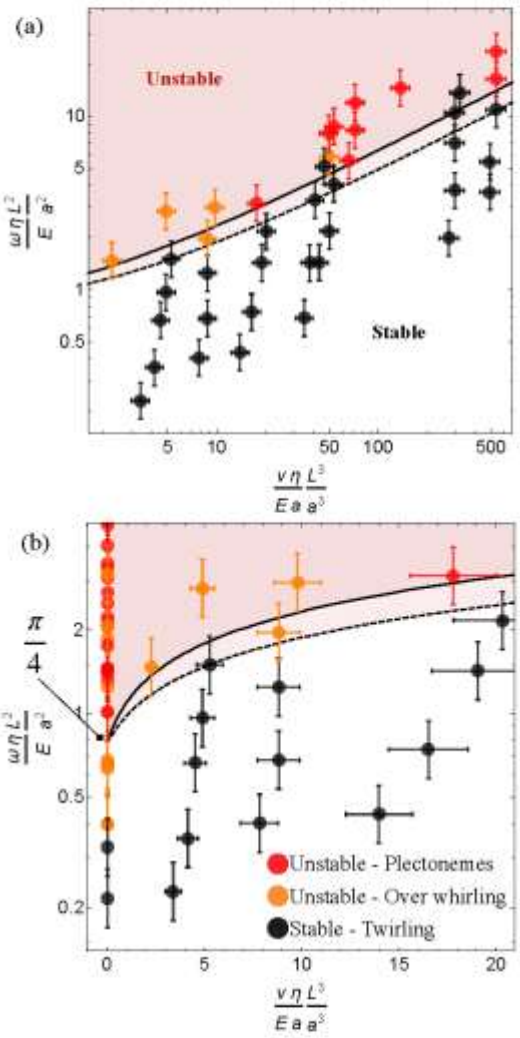

FIG. 2. Phase diagrams of instability with log-log (a) and log-linear (b) scaling. The solid and dashed lines show Eq. (7) with $\alpha = 8$ for $(L/a) = 100$ and $(L/a) = 1{,}000$, respectively. The region above each line is predicted to be unstable to helical buckling for the given (L/a). Error bars show one standard deviation attributed to experimental conditions. Parameters from individual data points are given in the S.I.

There are two important limits to consider. First is the limit $(v\eta/Ea)(L/a)^3 \gg 1$, which allows us to ignore the

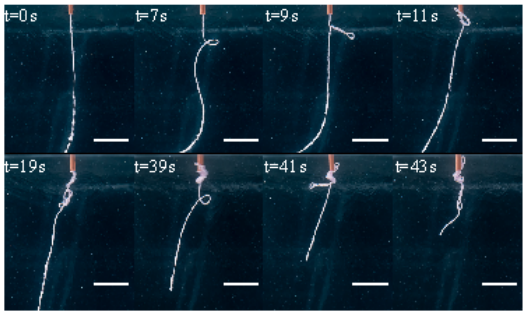

FIG. 3. Time series showing successive formation of three plectonemes in a filament with $L = 10$ cm, $a = 178$ μm, and $\omega = 57$ rads/s.

first term under the square root in Eq. (7) and produces a scaling of $\omega_c \sim \sqrt{v}$. Second, the zero fluid velocity limit, $v \to 0$, reproduces the result of Eq. (5) with a linear dependence $\omega_c \sim v$. Our model's prefactor of $\pi/4 \sim 0.785$ from Eq. (5) is within a factor of two of the experimental results, which appear to lie in the range of $0.3 - 0.4$ (see the y-intercept in Fig. 2).

For further comparison to alternative existing numerical models, the experimental results yield an ω_c that is also below what was originally predicted by Wolgemuth *et al.* [14]; however, it is above the numerical results of Lim and Peskin's immersed-boundary fluid dynamics model [18]. Our own model can expect an overestimation of the prefactor because it was difficult to prepare the initial state of the filament to be perfectly straight, and some amount of curvature was always present (as seen in the $t = 0$ images in Fig. 1). Wada and Netz have previously shown that the initial filament shape reduces ω_c by 25% for an initial radius of curvature of $L/2\pi$ [16], which is within the range of our experiments. Additionally, our approximation in Eq. (4) underestimates the average torsion by assuming it to be constant throughout the filament, while in reality the torsion is concentrated at the rotating (top) end. One would therefore expect an overestimation of this prefactor.

We made two additional experimental observations. First, the time required to reach the steady buckled state decreased with increasing ω, as would be naively expected. Second, the location of buckling (and therefore plectoneme formation) was independent of ω. This behavior is much like how the location of Euler buckling for a beam doesn't depend on the loading rate (for sufficiently slow rates), rather only that the critical load is achieved. Once the critical torsion had been exceeded in our system, the deflection occured at a distance only dependent on the length scale that determined the bending rigidity, EI; that is to say, the location of buckling depended only on the radius of the filament, a.

Surprisingly, this feature holds true even when multiple plectonemes form within the same filament. Typically, the normal torquing of a rod at both ends leads to only a single plectoneme as the initial helical instability gives way to localized writhing [22, 26]. This single plectoneme then grows in size, with further twisting only adding to its length. Alternatively, our unique setup of twisting via fluid drag allows for multiple plectonemes. An example of this behavior is shown in Fig. 3, which achieves a final total of three plectonemes. After the complete formation of the first plectoneme—whose final length is set by the available length of filament between the plectoneme's midpoint and the clamped top end—if there is sufficient length remaining to exceed the critical buckling torque, then another buckling event will occur at approximately the same distance from the rotating end. This phenomena is the only known example where multiple plectonemes can be formed in a filament without directly manipulating nodal points between plectonemes, or allowing for entropic effects in the thermodynamic limit (such as for DNA) [27].

By trading twisting stress for bending stress, a single plectoneme effectively acts as a Hookean storage container for fiber length, much like the coil spring and spool of a tape measure. This behavior therefore transforms traditionally nonelastic fibers into elastic ones. Furthermore, the effective strain capacity is no longer constrained by the yield strength of the material itself but by the amount of length absorbed by the plectoneme. This remarkable behavior means that plectoneme-containing strands could be used to construct super-elastic fibers and fabrics, opening another class of fiber-based artifical muscles used for work or actuation in soft materials [28]. Previously, only single-plectoneme fibers could be formed, which ensured unwieldy long plectonemes that would themselves behave like unruly strings, getting knotted, twisted, and tangled, and therefore preventing them from behaving like an ideal spring. However, by using our technique to divide plectonemes into many units within a fiber, the aforementioned problem is averted. Therefore, we envision multi-plectoneme fibers to have many potential applications including soft robotics and smart textiles for advanced super-elastic materials.

The authors would like to thank Draper staff for their support on experiment development and analysis: Ernest Kim, David Adler, Peter H. Lewis, Vanessa Sanchez, Terrell Williams, Tim Cook, Jordan De Guzman, Robert Hodgson, Peter Yung, Seth Van Liew, and Amy Duwel. This work was sponsored by the Air Force Research Laboratory (AFRL) and the Defense Advanced Research Agency (DARPA).

---

* These two authors contributed equally.

† Corresponding author: krussell@draper.com

[1] C. H. Wiggins and R. E. Goldstein, Physical Review Letters **80**, 3879 (1998).
[2] J. Elgeti, R. G. Winkler, and G. Gompper, Reports on Progress in Physics **78** (2015).
[3] S. P. Timoshenko and J. M. Gere, *Theory of Elastic Stability*, Dover Civil and Mechanical Engineering (Dover Publications, 2012).
[4] B. Audoly and Y. Pomeau, *Elasticity and Geometry: From Hair Curls to the Non-linear Response of Shells* (OUP Oxford, 2010).
[5] N. Leijnse, L. B. Oddershede, and P. M. Bendix, Proc. Natl. Acad. Sci. USA **112**, 136 (2014).
[6] K. Son, J. S. Guasto, and R. Stocker, Nat. Phys. **9**, 494 (2013).
[7] J. L. Silverberg, R. D. Noar, M. S. Packer, M. J. Harrison, C. L. Henley, I. Cohen, and S. J. Gerbode, Proc. Natl. Acad. Sci. USA **109**, 16794 (2012).
[8] M. Hajianmaleki and J. S. Daily, J. Pet. Sci. Eng. **116**, 136 (2014).
[9] J.-S. Chen and H.-C. Li, J. Appl. Mech. **78**, 41009 (2011).
[10] A. Aydin, L. Sun, X. Gong, K. Russell, D. Carter, and R. Gordon, ACS Appl. Polym. Mater. (in press).
[11] K. J. Russell *et al.*, Manuscript in preparation (2019).
[12] F. P. Gosselin, P. Neetzow, and M. Paak, Phys. Rev. E Stat. Nonlin. Soft Matter Phys. **90** (2014).
[13] M. K. Jawed, N. K. Khouri, F. Da, E. Grinspun, and P. M. Reis, Phys. Rev. Lett. **115**, 1 (2015).
[14] C. W. Wolgemuth, T. R. Powers, and R. E. Goldstein, Phys. Rev. Lett. **84**, 1623 (2000).
[15] T. R. Powers, Rev. Mod. Phys. **82**, 1607 (2010).
[16] H. Wada and R. R. Netz, EPL **75**, 645 (2006).
[17] H. Wada, Phys. Rev. E Stat. Nonlin. Soft Matter Phys. **84**, 1 (2011).
[18] S. Lim and C. S. Peskin, SIAM J. Sci. Comput. **25**, 2066 (2004).
[19] S. D. Olson, S. Lim, and R. Cortez, J. Comput. Phys. **238**, 169 (2013).
[20] T. C. Boles, J. H. White, and N. R. Cozzarelli, J. Mol. Biol. **213**, 931 (1990).
[21] S. Forth, C. Deufel, M. Y. Sheinin, B. Daniels, J. P. Sethna, and M. D. Wang, Phys. Rev. Lett. **100**, 1 (2008).
[22] J. M. Thompson and A. R. Champneys, Proc. R. Soc. Lond. A **452**, 117 (1996).
[23] A. Lazarus, J. T. Miller, M. M. Metlitz, and P. M. Reis, Soft Matter **9**, 8274 (2013).
[24] J. B. Keller and S. I. Rubinow, J. Fluid Mech. **75**, 705 (1976).
[25] H. Lamb, *Hydrodynamics*, Dover Books on Physics (Dover publications, 1945).
[26] G. H. M. Van Der Heijden and J. M. T. Thompson, Nonlinear Dyn. **21**, 71 (2000).
[27] M. Emanuel, G. Lanzani, and H. Schiessel, Phys. Rev. E Stat. Nonlin. Soft Matter Phys. **88**, 22706 (2013).
[28] C. S. Haines, N. Li, G. M. Spinks, A. E. Aliev, J. Di, and R. H. Baughman, Proc. Nat. Acad. Sci. USA **113**, 11709 (2016).

LIST OF SYMBOLS, ABBREVIATIONS, AND ACRONYMS

(skin depth, frequency, angular frequency, inductance, capacitance)

μ	Magnetic permeability
AFRL	Air Force Research Laboratory
ALD	Atomic layer deposition
DARPA	Defense Advanced Research Projects Agency
f	Frequency
FIB	Focused ion beam
NMR	Nuclear magnetic resonance
PAA	Polyacrylic acid
PMIA	Poly(m-phenylene isophthalamide)
PVD	Physical vapor deposition
Q	Quality factor (of a resonator or inductor)
RXAS	Soft Matter Materials Branch, Functional Materials Division, Materials and Manufacturing Directorate of AFRL
SNR	Signal to noise ratio
TGA	Thermal gravimetric analysis
VNA	Vector network analyzer
δ	Skin depth
ρ	Electrical resistivity